REVEALING NOVEL DEGRADATION MECHANISMS IN HIGH-CAPACITY BATTERY MATERIALS BY INTEGRATING PREDICTIVE MODELING WITH *IN-SITU* EXPERIMENTS

A Dissertation
Presented to
The Academic Faculty

By

Feifei Fan

In Partial Fulfillment
Of the Requirements for the Degree
Doctor of Philosophy in the
Georgia W. Woodruff School of Mechanical Engineering

Georgia Institute of Technology
August 2015

REVEALING NOVEL DEGRADATION MECHANISMS IN HIGH-CAPACITY BATTERY MATERIALS BY INTEGRATING PREDICTIVE MODELING WITH *IN-SITU* EXPERIMENTS

Approved by:

Dr. Ting Zhu, Advisor
School of Mechanical Engineering
Georgia institute of Technology

Dr. Shuman Xia
School of Mechanical Engineering
Georgia institute of Technology

Dr. Hailong Chen
School of Mechanical Engineering
Georgia institute of Technology

Dr. Gleb Yushin
School of Materials Science and Engineering
Georgia institute of Technology

Dr. Meilin Liu
School of Materials Science and Engineering
Georgia institute of Technology

Dr. Min Zhou
School of Mechanical Engineering
Georgia institute of Technology

Date Approved: May 13, 2015

To my parents

ACKNOWLEDGEMENTS

First and foremost, I would like to express my deepest gratitude to my Ph.D. thesis advisor, Dr. Ting Zhu, for his continuous invaluable guidance and immense support during my Ph.D. study. I am sure that Dr. Ting Zhu will continue to be a source of encouragement and expertise in my future professional career.

I would like to thank my thesis committee members: Dr. Hailong Chen, Dr. Meilin Liu, Dr. Shuman Xia, Dr. Gleb Yushin and Dr. Min Zhou for their valuable insights and comments on my research. In addition, I want to extend my gratitude to Dr. Adri van Duin, Dr. Jianyu Huang, Dr. Hong Li, Dr. Xiaohua Liu, Dr. Yang Liu, Dr. Scott X. Mao, Dr. Jiangwei Wang, Dr. Chunsheng Wang, Dr. Shuman Xia, Dr. Gleb Yushin, and Dr. Sulin Zhang for research collaboration. I would also like to thank my colleagues – Yifan Gao, Shan Huang, Hao Luo, Ying Liu, Xueju Wang and Zhi Zeng for helpful discussions.

Finally, I would like to give my special appreciation to my parents for their endless love and support throughout my life and for all sacrifices they have made for me in the past five years.

TABLE OF CONTENTS

LIST OF FIGURES

LIST OF TABLES

LIST OF ABBREVIATIONS

TEM	Transmission Electron Microscopy
ReaxFF	Reactive Force Field
DFT	Density Functional Theory
MEAM	Modified Embedded Atomic Method
LAMMPS	Large-Scale Atomic/Molecular Massively Parallel Simulator
BCC	Body-Centered-Cubic
FCC	Face-Centered-Cubic
HCP	Hexagonal-Close-Packed
MD	Molecular Dynamics
1D	One-dimensional
2D	Two-dimensional
3D	Three-dimensional
RDF	Radial Distribution Function
ADF	Angular Distribution Function
RVE	Representative Volume Element
SEM	Scanning Electron Microscope
LIB	Lithium Ion Battery
NIB	Sodium Ion Battery
SiNW	Silicon Nanowire
AAI	Amorphous-Amorphous Interface
CNF	Carbon Nanofiber
d-C	Disordered-Carbon
c-C	Crystalline-Carbon

SUMMARY

Lithium-ion (Li-ion) batteries are critically important for portable electronics, electric vehicles, and grid-level energy storage. The development of next-generation Li-ion batteries requires high-capacity electrodes with a long cycle life. However, the high capacity of Li storage is usually accompanied by large volume changes, dramatic morphological evolution, and mechanical failures in the electrodes during charge and discharge cycling. To understand the degradation of electrodes and resulting loss of capacity, this thesis aims to develop mechanistic-based models for predicting the chemo-mechanical processes of lithiation and delithiation in high-capacity electrode materials. To this end, we develop both continuum and atomistic models that simulate mass transport, interface reaction, phase and microstructural evolution, stress generation and damage accumulation through crack or void formation in the electrodes. The modeling studies are tightly coupled with *in-situ* transmission electron microscopy (TEM) experiments to gain unprecedented mechanistic insights into electrochemically-driven structural evolution and damage processes in high-capacity electrodes. Our models are successfully applied to the study of the two-phase lithiation and associated stress generation in both crystalline and amorphous silicon anodes, which have the highest known theoretical charge capacity, as well as the lithiation/sodiation-induced structural changes and mechanical failures in silicon-based multilayer electrodes. The modeling studies have uncovered unexpected electrochemical reaction mechanisms and revealed novel failure modes in silicon-based nanostructured anodes. Our modeling research provides insights into how to mitigate electrode degradation and enhance capacity

retention in Li-ion batteries. More broadly, our work has implications for the design of nanostructured electrodes in next-generation energy storage systems.

1 INTRODUCTION

Batteries are essential components of most electrical devices. They are used in our cars, laptops, power grids, and other electrical appliances. Desirable attributes of batteries include long life, high capacity, light weight, and low cost. Advances in battery technologies could help manufacture high-performance batteries and solve the energy crisis one day. Among the various existing technologies, lithium-ion (Li-ion) batteries currently outperform other energy-storage systems because of their high energy density and design flexibility [1]. This explains why Li-ion batteries have recently received most attention. Rechargeable Li-ion battery technologies have revolutionized our portable electronics, and it is important to the electrification of transportation vehicles. To meet the ever-increasing demand for energy consumption, innovations in Li-ion battery technologies is urgently needed.

Key components in a Li-ion battery include a cathode, an anode, and an electrolyte. The cathode, or the positive electrode, is typically made of Li metal oxide. The anode, or the negative electrode, is made of graphite, a form of carbon with a layered structure. The battery is filled with a transport medium, the electrolyte, so that the Li-ions carrying positive charges can flow freely. When the battery is charged, the positively charged Li ions from the cathode move through the electrolyte into the anode. When the battery discharges, namely the energy is removed from the cell, Li ions travel through the electrolyte from the anode back to the cathode.

The anode of current commercial Li-ion batteries is made of graphite. To enhance the capacity of the batteries, researchers seek new materials for the anodes. One of the

most promising anode materials is silicon (Si) because Si has a low discharge potential and the highest known theoretical charge capacity [1], as shown in Figure 1.1. However, such a high capacity of Li in Si anodes during charging and discharging is accompanied by a large volume expansion, which is about 280%. The 280% volume expansion induced by the electrochemical lithiation in Si anodes can cause fracture or even pulverization of the anodes, thereby leading to performance degradation [2-4].

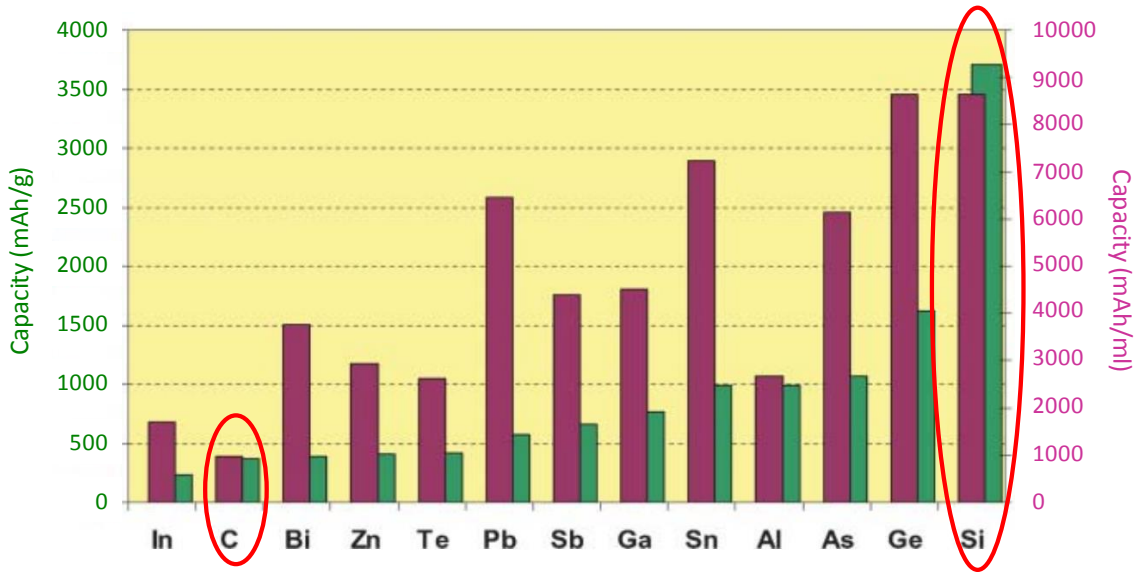

Figure 1.1 Gravimetric and volumetric capacities for selected alloying reactions. Reproduced from Ref. [1].

To mitigate the performance degradation in anode materials, researchers have developed nanostructured anode materials. The nanostructures have short Li diffusion distances, and can reduce lithiation-induced stress to avoid pulverization. Hence, these novel materials are able to withstand longer cycles with less degradation in electrochemical performance [1, 5-13]. Although there are numerous research efforts on the electrochemical behavior of these materials, the mechanical behavior and failure mechanisms associated with the electrochemical charging and discharging remains

largely unknown. Further, improving the overall performance of the nanostructured electrode materials requires an understanding of interplay between mechanical behavior and electrochemical processes, as well as physical mechanisms at various length scales:

- The electrochemical lithiation and delithiation of nanostructured Si anodes involves multiple physics phenomena. These phenomena include: (1) The lithiation of crystalline Si (*c*-Si) forms amorphous Li_xSi (a-Li_xSi) alloys, involving a transition from a crystalline phase to an amorphous phase [5, 13-15]. (2) During lithiation, as the Li concentration in Li_xSi alloys increases, the Young's modulus and the yield stress of Li_xSi alloys decreases drastically [15, 16]. (3) The lithiation of Si anodes also involves coupling among chemical reactions, species diffusion, and mechanical deformation [5, 17, 18]. (4) Si anodes undergo large elastic-plastic deformation and even fracture [17, 19-21].
- The electrochemical lithiation of Si electrodes also involves physical processes at multiple length scales. These processes include atomic-scale reaction at the phase boundary front [22, 23], as well as microstructural evolution due to species diffusion and phase separation [24]. While understanding the phase-boundary reaction requires the atomic-scale models, morphological changes and fracture can be efficiently studied using the continuum modeling tools [22, 25].

The multi-physics and multi-scale nature of the charging/discharging processes in the nanostructured electrode materials poses a challenge on modeling and simulations the electro-chemo-mechanical behavior. Modeling and simulating the coupling of concurrent multiple physics phenomena at various length scales have attracted tremendous research efforts [21, 26-40]. A wide range of modeling and simulation methods have been applied

to investigate the physical mechanisms for improving the reliability and performance of the novel electrode materials (Figure 1.2).

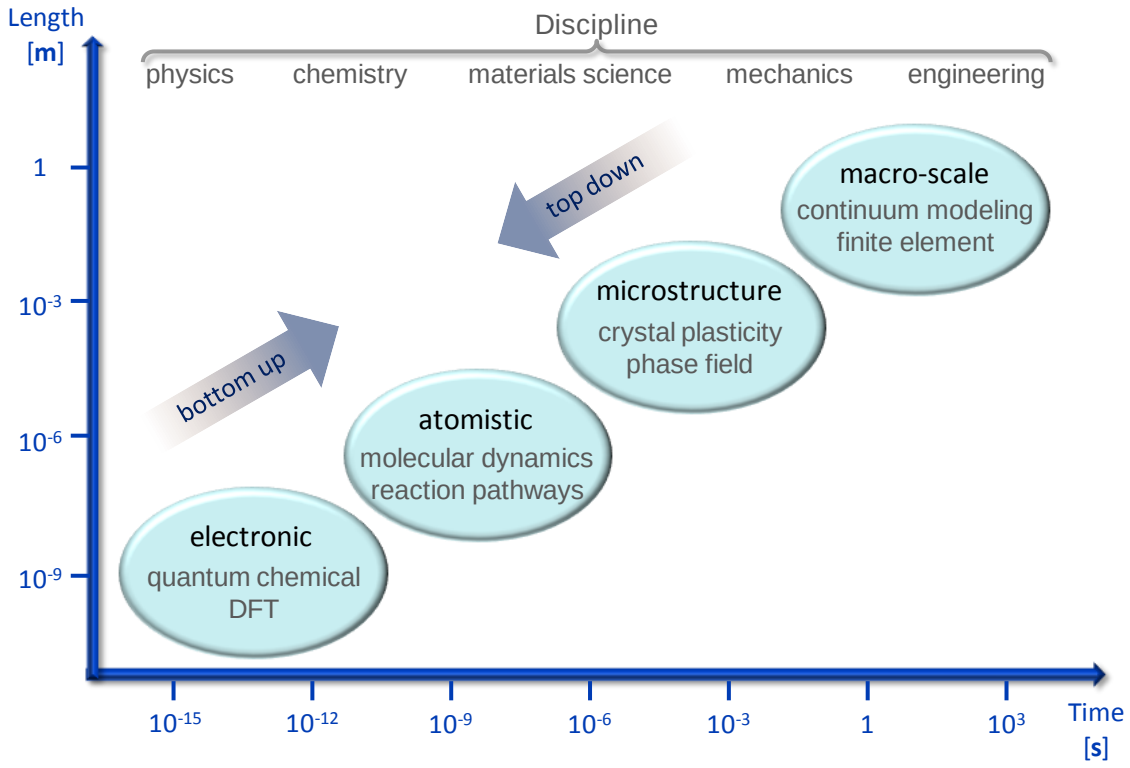

Figure 1.2 Multi-physics and multi-scale modeling in electrode materials during electrochemical charging and discharging.

This thesis is focused on understanding the novel degradation mechanisms in high-capacity battery materials by integrating predictive modeling with *in-situ* transmission electron microscopy (TEM) experiments. In this thesis, the mechanistic based models at the atomistic and continuum levels for predicting the chemo-mechanical processes are developed. The modeling studies are tightly coupled with *in-situ* TEM experiments, so as to gain unprecedented mechanistic insights into the electrochemically-driven structural evolution and damage processes in the electrodes.

1.1 Mechanical Behavior of Li_xSi Alloys: An Atomistic Study

Silicon (Si) is a promising electrode material for next-generation Li-ion batteries [17, 19, 33, 41]. A major challenge to the application of Si electrodes is the electrochemically-induced mechanical degradation, which can cause capacity fading and limit the cycle life of lithium-ion batteries [3, 25, 34, 41]. During electrochemical cycling, Li usually reacts with Si to form the amorphous Li_xSi (*a*-Li_xSi) alloys [13, 37, 42-44]. Despite the intensive electrochemical study of *a*-Li_xSi, their mechanical properties and associated atomistic mechanisms remain largely unexplored.

Several recent experimental studies have investigated the mechanical properties of *a*-Li_xSi. Hertzberg *et al.* conducted the nanoindentation testing on polycrystalline Si thin films at various stages of lithiation [45]. They reported a strong dependence of Young's modulus and hardness on the Li to Si ratio. Young's modulus was found to decrease from an initial value of 92 GPa for pure Si to 12 GPa for $Li_{3.75}Si$, and the hardness changes from 5 GPa to 1.5 GPa, correspondingly. Chon *et al.* used the curvature measurement technique to determine the yield stress in a lithiated Si thin film [42]. They reported a yield stress of 0.5 GPa for *a*-$Li_{3.5}Si$, and other thin film lithiation experiments reported similar values [43]. Kushima *et al.* measured the fracture strength and plasticity of lithiated Si nanowires by *in situ* tensile testing inside a transmission electron microscope [46]. The tensile strength decreased from the initial value of about 3.6 GPa for pristine Si nanowires to 0.72 GPa for *a*-Li_xSi ($x \sim 3.5$) nanowires. They also reported the large fracture strains that range from 8-16% for *a*-Li_xSi ($x \sim 3.5$) nanowires, 70% of which remained unrecoverable after fracture.

The mechanical properties of *a*-Li_xSi alloys have also been recently studied using quantum mechanical and interatomic potential calculations. Shenoy *et al.* performed the density functional theory (DFT) calculations of the elastic properties of *a*-Li_xSi alloys [36]. They showed the elastic softening with increasing Li concentration. Zhao *et al.* conducted DFT calculations for both the biaxial stress in *a*-Li_xSi thin films and the yield stress in bulk *a*-Li_xSi under uniaxial tension [47]. They found large differences between the characteristic stress levels of the two cases. Cui *et al.* developed a modified embedded atomic method (MEAM) interatomic potential for the Li_xSi alloys [48]. They performed molecular dynamics simulations of uniaxial tension for bulk *a*-Li_xSi at 300K and showed that the yield strength decreased from about 2 GPa for LiSi to 0.5 GPa for *a*-$Li_{3.75}Si$. In addition, quantum calculations have been performed to study the atomic structures and energetics, as well as Li diffusion, in *a*-Li_xSi alloys [26, 27, 30-32, 38, 49-51]. The aforementioned modeling studies not only provide valuable insights into the mechanical properties of *a*-Li_xSi, but also highlight the challenges to understand the structure-property relationship in *a*-Li_xSi. Namely, the composition and atomic structure can change drastically during electrochemical cycling of Si electrodes, involving for example the transition from a Li-poor network glass to a Li-rich metallic glass with increasing Li concentration during lithiation [52, 53].

In Chapter 2, we employ a newly developed reactive force field (ReaxFF) to study the mechanical behavior of the *a*-Li_xSi alloys using MD simulations. This ReaxFF provides the accurate predictions of a set of fundamental properties for Li_xSi alloys, such as Li composition-dependent elastic modulus, open-cell voltage, and volume expansion. Compared to DFT, the computational efficiency of ReaxFF enables the large scale MD

simulation of *a*-Li_xSi, which is crucially important for sampling amorphous structures and thus obtaining their statistically meaningful properties. In addition, ReaxFF is capable of describing various bonding environments, essential for improving the chemical accuracy of simulated structures and properties spanning a wide range of Li compositions.

1.2 Chemo-Mechanics of Si Electrodes: An Atomistic Study

Our ReaxFF-based MD modeling and simulations are capable of capturing the chemo-mechanical behavior of *a*-Li_xSi alloys during electro-chemical lithiation. In Chapter 3, we study the first lithiation of *c*-Si nanopillars (Section 3.1) and subsequent lithiation of *a*-Si thin films (Section 3.2).

First lithiation of c-Si nanopillars

The first lithiation of *c*-Si exhibits two significant features. One feature is that the lithiation occurs in a two-phase mechanism, namely there exists a phase boundary between pristine Si and lithiated Si and the lithiation proceeds through the movement of a sharp phase boundary [17, 19]. The *in-situ* TEM experiments show that the thickness of the phase boundary is about 1nm, and lithiation in *c*-Si proceeds through the layer-by-layer removal of Si atoms on close-packed plane. The reason for this two-phase mechanism is that at the phase boundary high lithium concentration is needed to break strong Si-Si covalent bonds and dissolve Si atoms from Si covalent network (Figure 1.3). The other feature is that lithiation-induced expansion is highly anisotropic, leading to anomalous swelling and even fracture in Si nanostructured electrodes [25]. TEM experimental characterization shows the mobility of the sharp phase boundary is

orientation-dependent. For example, the mobility of {110} phase boundary is higher than that of {111} phase boundary, and the lithiation-induced expansion along <110> direction is larger than that along <111> direction [18, 54].

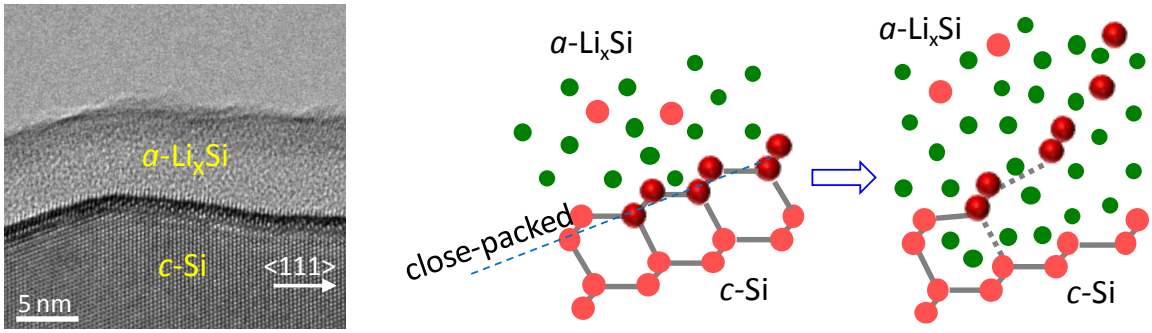

Figure 1.3 The two-phase mechanism in the first lithiation of *c*-Si. The left image is taken from *in-situ* TEM experimental characterization results, showing a sharp phase boundary between *c*-Si and *a*-Li_xSi. The right image is a schematic illustration on the layer-by-layer removal of Si atoms from a Si network during lithiation. Reproduced from Ref. [18].

The chemo-mechanical behavior of Si nanostructured electrodes has been often modeled with simplified constitutive laws and chemo-mechanical properties. The question may arise: Are these constitutive models capable of capturing the chemo-mechanical behavior and predicting associated failure mechanisms? To bridge the gap between the physical processes at the atomistic level and the chemo-mechanical behavior at the continuum level, we perform large-scale atomistic simulations using the ReaxFF method, which allow a direct output of lithiation-induced morphological evolution and the spatial distribution of stress (Section 3.1). The atomistic modeling and simulations take into account both the two-phase mechanism and the anisotropic lithiation. The results provide mechanistic insights into the chemo-mechanics of *c*-Si nanostructured electrodes during the first lithiation.

Lithiation of a-Si thin films

Currently, one effective method of measuring the mechanical properties of *a*-Li_xSi is to test the lithiation response of a Si thin film on an inactive substrate (e.g., a Cu underlayer on a Si wafer) [19, 22, 55]. Upon electrochemical lithiation, volume expansion in the lithiated Si thin film is constrained by the substrate, generating a biaxial compressive stress in the film. The film stress can be determined from the curvature change of substrate based on the Stoney equation. The lithiation stresses measured from such thin film experiments were often taken as the yield strengths of *a*-Li_xSi alloys in recent literature. Based on the results of these studies, we raise the following questions: Can these thin-film stresses well represent the plastic properties of *a*-Li_xSi alloys? What is the relationship between the yield strength measured from the thin-film experiment during lithiation and that from the mechanical deformation of biaxial compression, uniaxial tension and compression of *a*-Li_xSi after lithiation? Considering the limited experimental data available, here we address these questions with ReaxFF-based MD simulations for providing insights into the effects of composition, loading mode and stress state on the mechanical properties of *a*-Li_xSi alloys.

In Section 3.2, we present the MD simulation results of lithiation in an *a*-Si thin film. We analyze stress generation in the film during the lithiation and the relationship between the stress generation and the Li concentration of *a*-Li_xSi. We then compare the results with those obtained from pure mechanical loading and discuss whether the loading sequence affects the measurements of the mechanical properties of *a*-Li_xSi alloys.

1.3 Atomistically-Informed Continuum Modeling

Improving the reliability and performance the high-capacity nanostructured electrodes requires a fundamental understanding of underlying physical processes at the atomic scale and their interplay during charge and discharge cycling. The atomic-level physical processes have been investigated through both *in-situ* and *ex-situ* experiments [18, 20, 33] and atomistic modeling and simulations [36, 56, 57]. These investigations have revealed critical factors controlling the physical processes, such as electrochemical reaction mechanisms [18, 54] and the evolution of physical properties [19, 20]. These factors play an important role in the degradation of the electrodes. For example, whether the lithiation is reaction-control or diffusion-control affects the morphological evolution of the electrodes, associated stress generation, as well as fracture and failures. To capture the essential features of lithiation-induced stress and failures, continuum models need to account for these critical factors at the atomic scale.

Diffusion, reaction, and large-strain deformation

In the first part of Chapter 4, we develop a physical-based model for simulating Li diffusion, reaction of Li and Si, and large-strain deformation in the nanostructured electrodes. This model incorporates key information of these physical processes obtained from *in-situ* TEM experiments and atomistic simulations. Therefore, the model is able to simulate the reaction-controlled and diffusion-controlled lithiation, which could cause anomalous morphological evolution of the electrodes as shown in Figure 1.4 [41]. Furthermore, the model is based on large-strain elastic-plastic deformation theory. Therefore, it can accurately predict the stress generation and cracking.

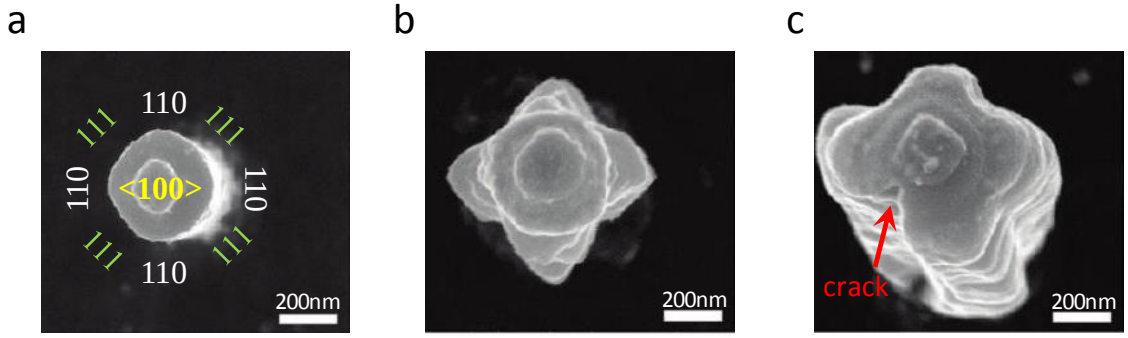

Figure 1.4 Cracking in a <100>-oriented *c*-Si nanopillar. (a) Initial cross section of the nanopillar. (b) Cross section of the nanopillar in an intermediate stage of lithiation. (c) Cracking occurs in a late stage of lithiation. Reproduced from Ref. [41].

Application to Si nanostructured anodes

In the second part of Chapter 4, we apply our model to study the lithiation-induced degradation in both *c*-Si and *a*-Si nanostructured anodes. Together with TEM and SEM experimental characterization, the modeling studies have uncovered unexpected electrochemical reaction mechanisms, such as two-phase lithiation mechanism in the first lithiation of *a*-Si. In addition, motivated by experimental observations [17, 21, 41, 58], the studies have revealed novel failure mechanisms in Si-based nanostructured anodes, by analyzing lithiation-induced stress generation and fracture modes. The modeling research provides mechanistic insights into how to mitigate electrode degradation, and therefore helps to optimize the design of high-capacity electrodes.

1.4 Chemo-Mechanics of Multilayer Electrodes

One of the main challenges with high-capacity LIB electrodes is the dramatic volume change during cycling. For the purpose of reducing the overall volume change,

nanostructured composite electrodes, such as carbon/silicon nanotubes and hierarchical nanostructures, have been developed owing to rapid progress in synthesis and fabrication techniques [5, 10, 14, 16, 59, 60]. These advanced electrodes can reduce stress generation, better accommodate inhomogeneous volume expansion, minimize side reactions, as well as enhance electrical transport. Because of these improvements, these electrodes can withstand the increasing number of charge-discharge cycles without significant capacity loss, and therefore have great potential for applications in electrodes of next-generation rechargeable batteries [5, 16, 61-68]. However, the structural complexity of the nanostructured composites could introduce novel phenomena and degradation mechanisms. In Chapter 5, we investigate the chemo-mechanical behavior of two different nanostructured multilayer anodes: bilayer carbon nanofibers as Na-ion anodes and SiO_2-coated Si nanopillars as Li-ion anodes.

Sodiation of bilayer carbon nanofibers

Recently, batteries based on other alkali-metals, such as Na-ion batteries (NIBs) have attracted great attention, owing to their comparatively high natural abundance and low cost [69-73]. Considering the similar chemical properties of Li, Na, and K, the anode and cathode materials used in LIBs are being investigated for their applications in NIBs in the past few years. The potential anode materials for NIBs include carbonaceous materials, Sn, Sb, and metal oxides. Among these candidates, carbonaceous materials are most promising, given their successful applications in commercial LIBs and particularly low cost, natural abundance, small volumetric expansion during alloying with alkali-metals [70, 74, 75]. Graphite has been used as the anode of current commercial LIBs with a theoretical capacity of 372 mAh/g [76]. However, only a small amount of Na ions can

be stored in the graphite anode of NIBs. Such a limitation has been often attributed to the higher intercalation energy barrier of Na ions [69, 70, 77]. So far, the highest capacity for carbonaceous anodes reported in NIBs is about 300 mAh/g in hard carbon, whose usage is severely limited by its poor cyclability [77]. Recently, the disordered or amorphous carbon materials were found to exhibit much improved cyclability [70, 75, 78]. For example, the disordered hollow carbon nanowires showed a reversible capacity as high as 251 mAh/g with 82.2% capacity retention after almost 400 sodiation-desodiation cycles [75], which is much better than hard carbon [79]. Moreover, carbon is often used to enhance electron conduction in anodes or cathodes of LIBs and NIBs, as well as to support other active materials in high-capacity nanocomposite anodes for LIBs and NIBs [64, 80-83]. Therefore, it is essential to understanding the electrochemical reactions and associated structure-property relationships of carbon-based anodes during sodiation, thereby paving the way for future development of the novel carbon-based or carbon-supported nanocomposite anodes for NIBs.

Lithiation of SiO_2-coated Si nanowires

Charge/discharge cycling of Si anodes is accompanied with dramatic volume changes, leading to fracture and pulverization [42, 84]. Such fracture and pulverization can cause continuous formation and growth of solid electrolyte interphase layer on newly-formed surface of the electrodes, resulting in low Columbic efficiency and high impedance. To maintain structural integrity and minimize side reactions, a coating layer has been introduced on the surface of the active materials. Recently, various coating materials, such as SiO_2 [10, 60, 62, 85, 86], Al_2O_3 [87], TiO_2 [87, 88], and Carbon [89, 90], have been employed for performance enhancement of Si anodes. Among these

materials, SiO_2 has attracted particular interest because of the following reasons: (1) the growth of a native SiO_2 layer on Si surface is unavoidable; (2) the thickness of a SiO_2 layer can be easily controlled through thermal oxidation; (3) SiO_2 exhibits high natural abundance, large reversible capacity of Li, and low discharge potentials [91-95]. To improve the performance of SiO_2-coated Si nanostructured anodes, understanding the chemo-mechanics of the coated anodes is essential and worth a detailed study.

In Chapter 5, we present chemo-mechanical modeling studies of nanostructured multilayer electrodes for Li-ion and Na-ion batteries including hollow carbon nanofiber (CNF) anodes (Section 5.1) and oxide-coated Si nanowires (Section 5.2). We investigate the origin of geometrical changes and crack formation. Our modeling studies provide mechanistic insight into the microstructure evolution and mechanical degradation of multilayer electrodes in electrochemical reactions.

2 MECHANICAL BEHAVIOR OF Li_xSi ALLOYS: AN ATOMISTIC STUDY

Electrochemical cycling of a Si electrode usually produces amorphous Li_xSi (*a*-Li_xSi) alloys at room temperature. Despite the intensive electrochemical study of *a*-Li_xSi alloys, their mechanical behavior and underlying atomistic mechanisms remain largely unexplored. In this study, we perform molecular dynamics simulations to characterize the mechanical properties of *a*-Li_xSi with a newly developed reactive force field (ReaxFF). We compute the yield and fracture strengths of *a*-Li_xSi under a variety of mechanical loading conditions, including biaxial compression, uniaxial tension and compression. The effects of loading sequence and stress state are investigated to correlate the mechanical behavior with the dominant atomic bonding characteristics that are mediated by the Li content. We also investigate fracture mechanisms in *a*-Li_xSi, and the simulation results reveal a brittle-to-ductile transition as Li-concentration increases in the *a*-Li_xSi alloys. The results provide mechanistic insights for interpreting experiments, understanding intrinsic properties and designing new experiments on *a*-Li_xSi alloys, essential to the development of durable Si electrodes for high-performance Li-ion batteries.

2.1 A Reactive Force Field (ReaxFF) for Li_xSi

The parameters of ReaxFF for *a*-Li_xSi systems were optimized against a based training set from density functional theory (DFT) calculations, containing a collection of data including energies, geometries and charges. ReaxFF bond, off-diagonal and valence angle parameters relevant to the *a*-Li_xSi system were optimized. A total of 10 parameters

were fitted to a training set containing 142 data points using a successive single-parameter search method with multiple cycles to account for parameter correlation [96].

The ReaxFF uses the Si parameters developed by van Duin *et al*. [97] and was further trained to model the *a*-Li_xSi systems. The force field was trained against the equation of states for the simple cubic phases of Si [97] and the body-centered cubic (bcc), face-centered cubic (fcc) and hexagonal-close-packed (hcp) phases of Li. In Figure 2.1 (a), we compare the equations of states for the bcc, fcc and hcp phases of Li given by ReaxFF and DFT studies. The ReaxFF energy curves are in good agreement with DFT calclations, with an root mean square deviation of only 1.65 kcal/mol for bcc, 2.14 kcal/mol for fcc and 2.36 kcal/mol for hcp phases of Li.

The ReaxFF was also trained against the energy curves for crystalline LiSi, $Li_{12}Si_7$, $Li_{13}Si_4$ and $Li_{15}Si_4$ given by DFT calculations. Figure 2.1 (b) – (c) gives the comparison of energy curves of LiSi, $Li_{12}Si_7$, $Li_{15}Si_4$ and $Li_{13}Si_4$ crystals predicted by ReaxFF and DFT calculations. The root mean square deviation of ReaxFF energy curves from DFT calculations is only 0.23 kcal/mol for LiSi, 9.58 kcal/mol for $Li_{12}Si_7$, 0.46 kcal/mol for $Li_{13}Si_4$ and 3.68 kcal/mol for $Li_{15}Si_4$. Table 2.1 lists the heat of formation of various Li/Si crystals predicted by ReaxFF and its comparsion with corresponding DFT values. The ReaxFF and DFT results are in good agreement.

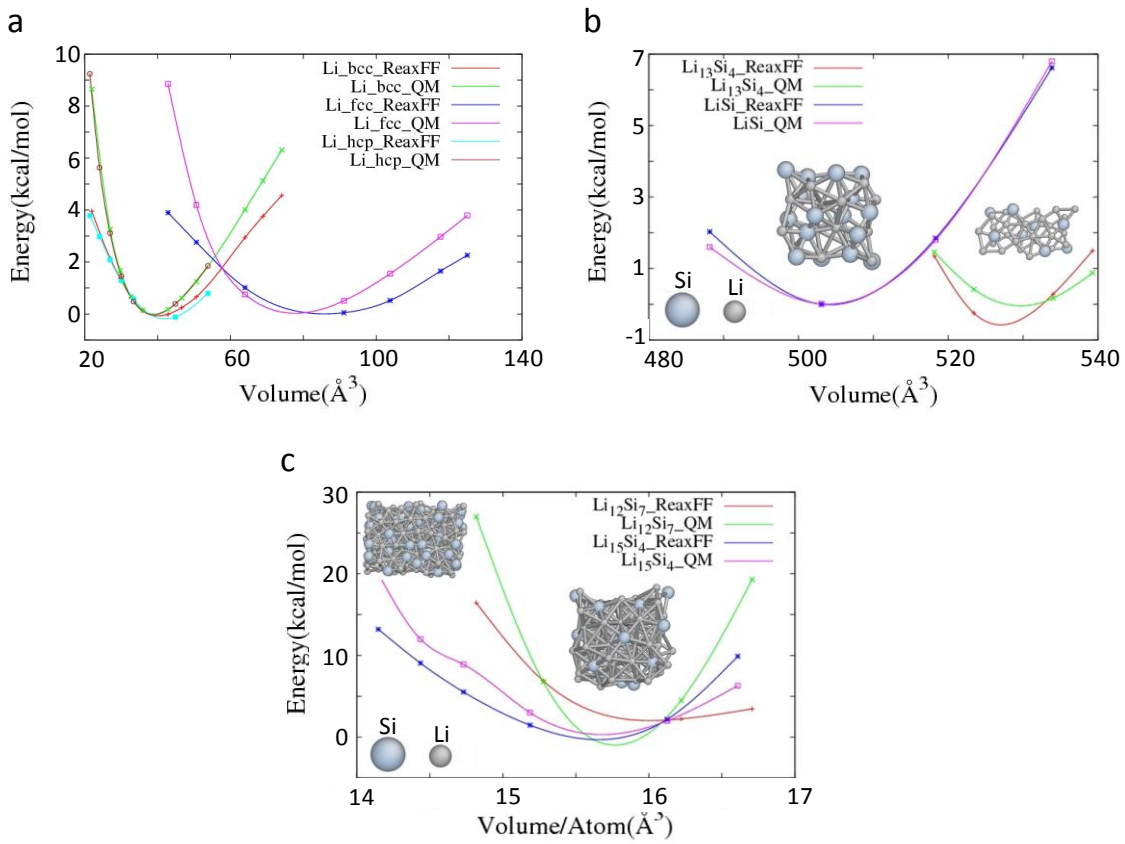

Figure 2.1 (a) Energy versus volume for the bcc, fcc and hcp phases of pure Li from ReaxFF and DFT calculations. (b) Energy versus volume for crystalline LiSi and $Li_{13}Si_4$ predicted by ReaxFF and DFT calculations. (c) Energy versus volume for crystalline $Li_{12}Si_7$ and $Li_{15}Si_4$ from ReaxFF and DFT calculations.

Table 2.1 Heat of formation of LiSi, $Li_{13}Si_4$ and $Li_{15}Si_4$ crystals from ReaxFF and DFT caclulations.

	ReaxFF (kcal/mol)	DFT (kcal/mol)
LiSi	-14.85	-9.30
$Li_{13}Si_4$	-85.47	-99.75
$Li_{15}Si_4$	-95.02	-104.84

2.2 Structural Characterization of Li_xSi Alloys

The *a*-Li_xSi alloys with several representative Li concentrations are generated using molecular dynamics (MD) simulations. The MD simulations are conducted using the Large-scale Atomic/Molecular Massively Parallel Simulator (LAMMPS) [98]. For each composition, the starting system is either *c*-Si with interstitial Li atoms distributed evenly or the crystalline compound of Li_xSi. Each system contains approximate 2000 atoms in total. Amorphous structures are obtained by melting the starting systems under a stress-free condition and quenching at a fixed cooling rate. That is, each system is relaxed under three-dimensional (3D) periodic boundary conditions for 0.5-1.2 ns at a temperature about twice of its melting point, and then the system is cooled at a rate of 10^{13} K/s to room temperature, 300 K.

We note the procedure described above aims to obtain amorphous structures. With sufficient equilibration of structures at high temperature, the choice of a pre-quenched structure does not affect the amorphous system upon quenching. However, the local structure and shear modulus could be influenced by cooling rate and relaxation history in MD simulations. This is because a slower rate gives the structure longer relaxation time to reach a lower energy, which results in a more stable system and higher shear modulus. In contrast, a higher cooling rate results in lower barriers between the sub-basins in the potential energy landscape, thus rearrangement of atoms is easier to occur.

Previous studies show that the continuous random covalent network of Si is gradually broken during the insertion of Li [99], as Li atoms weaken and break Si-Si

bonds. Characterization of *a*-Li_xSi systems at each composition yields qualitative measurements on the changes in local structures and bonds. For current *a*-Li_xSi systems, several different parameters are used in order to describe the essential features of structures with various Li concentrations.

Figure 2.2 (a) – (d) shows as-built amorphous systems for selected *a*-Li_xSi alloys and pure amorphous Li (*a*-Li) and *a*-Si systems. Figure 2.2 (e) – (f) reveals how the continuous Si network is disrupted with increasing Li concentrations. When Li concentration is relatively low, the Si network is partially destroyed and featured with long Si chains and large Si rings. With increasing Li content, Si chains are progressively shortened to isolated Si atoms and short Si chains, such as boomerangs and dumbbells.

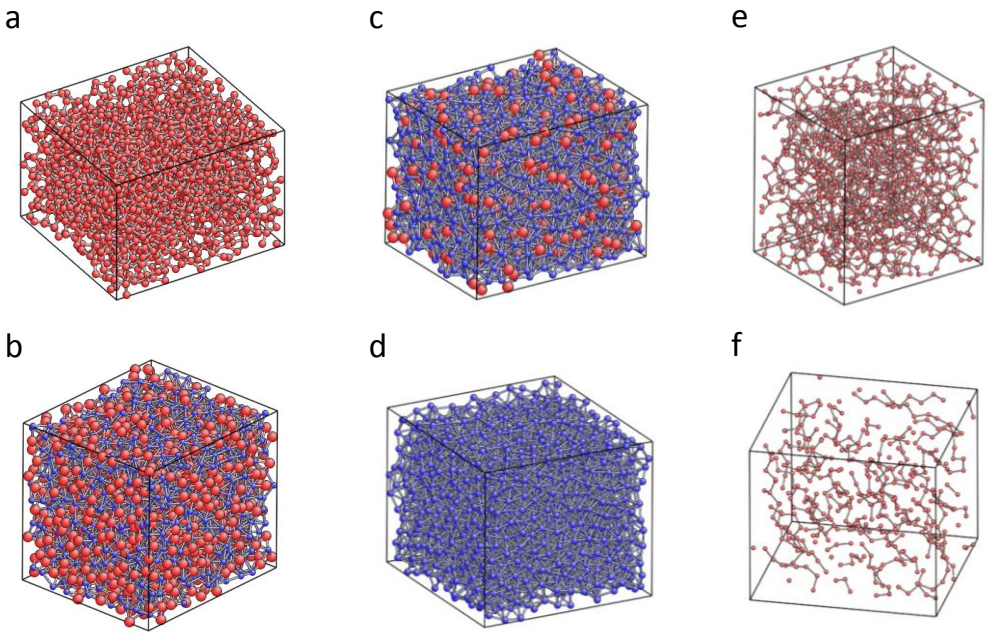

Figure 2.2 Visual representation of as-built systems for selected amorphous LixSi alloys, showing that the structures are amorphous. Red spheres represent Si atoms, while blue ones represent Li atoms. (a) *a*-Si,

(b) *a*-LiSi, (c) *a*-$Li_{15}Si_4$, (d) *a*-Li, (e) broken Si network in *a*-LiSi (Li-poor phase), and (f) Si chains in *a*-$Li_{15}Si_4$ (Li-rich phase).

Breaking of the random covalent network of Si during Li insertion can be characterized by the evolution of ring statistics (Figure 2.3 (a)). The ring fraction of pure *a*-Si has a peak at the 6-membered ring, and the rings with other numbers of atoms arise because of amorphization. As Li concentration increases, 3-membered rings become increasingly dominant. In highly lithiated Si alloys, the fraction of the rings with other numbers of atoms almost diminishes. The distribution is consistent with previous results from molecular orbital theory calculation [30], in which the DFT study shows that Li atoms prefer to stay in large space of Si network. With very low Li concentration, Si-Si bonds are not broken but weakened. As Li content increases, the local environment of a Si atom is mainly occupied by Li atoms, resulting in the dominance of three-atom rings. Figure 2.3 (b) and (c) show the local environment of Si atoms in *c*-$Li_{15}Si_4$ and *a*-$Li_{15}Si_4$. Each Si atom in *c*-$Li_{15}Si_4$ is isolated, while in our *a*-$Li_{15}Si_4$ system, there are only a few isolated single Si atoms. The surrounding atoms of a Si atom in the *a*-$Li_{15}Si_4$ system contain both Li atoms and Si atoms. These Si-Si bonds are weakened by the neighboring Li atoms, and pure covalent bonding in Si is expected to be transited to metallic-covalent mixed bonding.

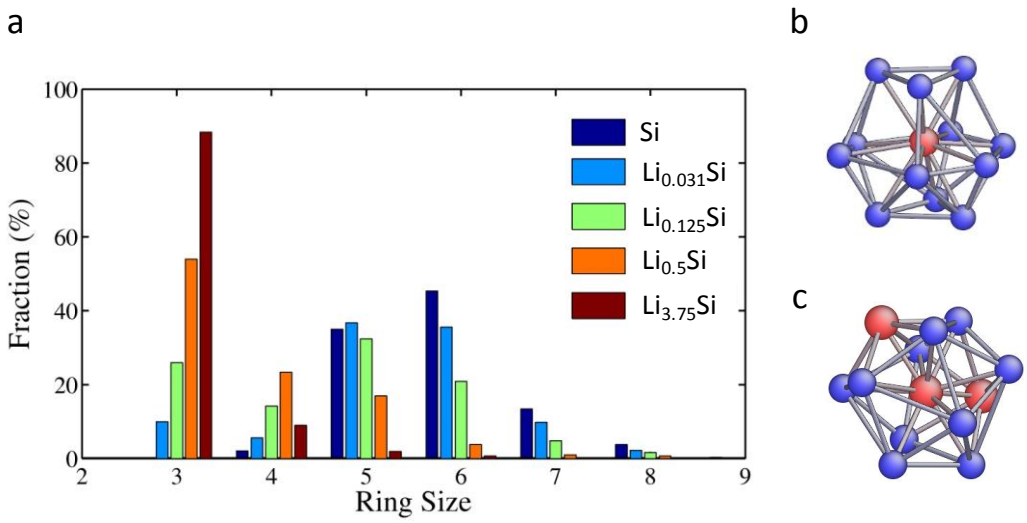

Figure 2.3 (a) The distribution of ring sizes in *a*-Si and *a*-Li_xSi alloys. (b) A Si atom is surrounded by Li atoms in a *c*-$Li_{15}Si_4$ structure, indicating each Si atom is isolated. (c) Environment for a Si atom in *a*-$Li_{15}Si_4$ structure, indicating in the amorphous phase there exist Si-Si bonds which are weakened by surrounding Li atoms.

The local structural evolution and bonding environment in *a*-Li_xSi can also be characterized through radial and angular distribution functions. Figure 2.4 (a) shows total (g_{total}) and partial radial distribution functions (RDFs) ($g_{Li\text{-}Si}$, $g_{Li\text{-}Li}$, and $g_{Si\text{-}Si}$) for the as-built *a*-Li_xSi structures with selected compositions. The results of the RDFs do not exhibit sharp peaks, confirming the amorphous nature of the structures. The right shift of the first peak in the total RDF demonstrates that as Li content increases Si-Si pairs are dispersed and Li-Si and Li-Li pairs become dominant gradually. We note that there is an undesired peak between 3.0 Å and 3.5 Å in the total RDF of *a*-Si and *a*-$LiSi_{32}$. This peak is caused by the fast quench rate, which results in "liquid-like" environment in *a*-Si [52, 100, 101]. The peak is not expected when quench rate is slow enough, and slow quench rate can generate a "solid-like" environment [52, 100, 101]. Angular distribution functions (ADFs) are presented (Figure 2.4 (b)) to provide complementary information

on the local structural evolution and bonding environment in *a*-Li_xSi during the increase of Li concentration. Two well-defined peaks are developed and gradually become narrow with increasing Li concentration. We note that the shoulder in the ADFs for the as-build *a*-Si structure is a sign of the "liquid-like" feature of *a*-Si caused by fast quenching.

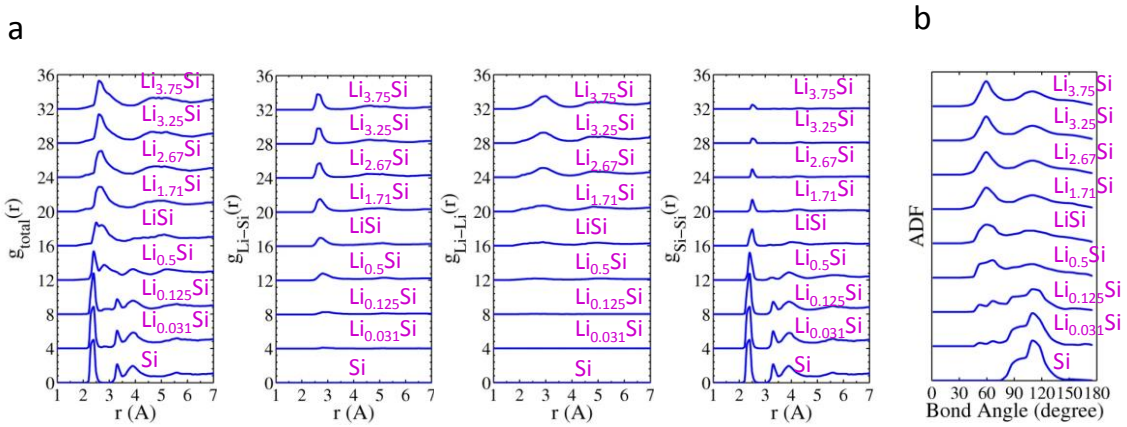

Figure 2.4 (a) Total and partial pair-distribution functions for selected *a*-Li_xSi alloys. For each composition, two independent samples are used. (b) Angular distribution functions for selected *a*-Li_xSi alloys. For each composition, two independent samples are used.

2.3 Elastic Softening of Li_xSi Alloys

Using ReaxFF, we evaluate the open-cell voltage [30], volume expansion and Young's modulus of *a*-Li_xSi, as a function of Li concentration, as shown in Figure 2.5. Regarding the lithiation-induced volume expansion, it can be affected by the initial structure of an *a*-Si network. In our simulations, *a*-Si is generated by the melting-quenching method, and hence its structure can be influenced by the quench rate. Under the simulated quench rate in our MD, *a*-Si is more liquid-like with a mass density of $1.069\rho_0$ (where ρ_0 is the density of *c*-Si), and contains less free volumes to accommodate

the Li insertion. In contrast, the *a*-Si in experiment (and *c*-Si) usually has a lower density, is more solid-like, and contains more open volumes. Therefore, the volume change caused by Li insertion in our simulated *a*-Si is larger than that for *c*-Si or experimental *a*-Si at low Li concentrations [100]. For example, our ReaxFF gives a volume change of 3.7% from *c*-Si to $Li_{0.125}Si$ by inserting Li atoms to interstitial sites, and 7.0% from as-quenched *a*-Si to *a*-$Li_{0.125}Si$.

Despite the aforementioned structure difference, elastic moduli predicted from our simulations show overall agreement with experimental measurements [52], i.e., the decrease of elastic modulus with increasing Li concentration [101]. However, Young's moduli from the ReaxFF are closer to the rule of mixtures than DFT calculations [36] and experimental measurements [101]. At this moment, the origin of discrepancy is not clear. While such discrepancy might arise from the inaccuracy of the ReaxFF, we also note the limitations of other approaches. In the experiments, the measured Young's modulus might not correspond to the elastic properties of a single phase Li_xSi when $0 < x < 3.75$. This is because it is not clear whether the Li distribution is uniform or not in partially lithiated samples, considering the two-phase lithiation has been observed in *a*-Si [44]. In DFT calculation, the results could be limited by the relaxation time and system sizes that affect the statistical accuracy to represent the amorphous structures of *a*-Li_xSi alloys.

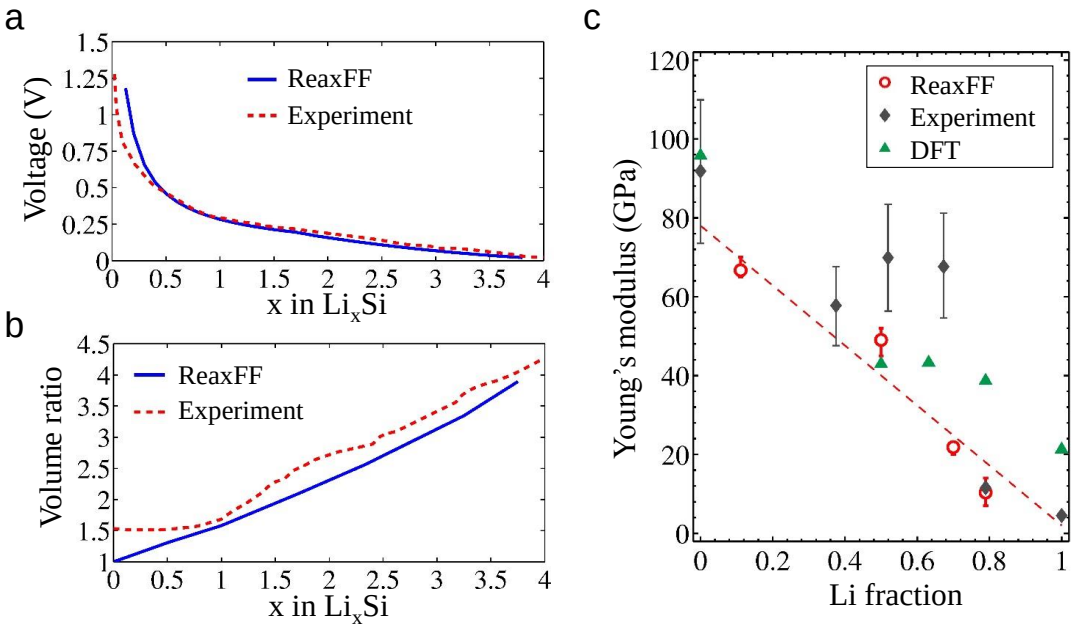

Figure 2.5 Comparison of properties of *a*-Li$_x$Si between experimental measurements and predictions from ReaxFF and DFT. (a) Voltage versus Li concentration x. Experimental results are taken from Ref. [8]. (b) Ratio of the current volume and initial volume versus Li concentration x. Experimental results are taken from Ref. [20]. (c) Young's moduli of *a*-Li$_x$Si alloys at 300K. Experimental results are taken from Ref. [20]. DFT results are taken from Ref. [36].

2.4 Plastic Behavior of Li$_x$Si Alloys

Experimental measurements of stress generation in *a*-Li$_x$Si thin films indicate that plastic flow occurs during lithiation/delithiation for accommodating large deformation [8, 19, 22, 55]. The measurements also show that the yield stress of *a*-Li$_x$Si gradual decreases as Li concentration increases. These experimental results suggest a prominent lithiation-induced plastic softening in *a*-Li$_x$Si alloys. In addition, first-principles studies show that Si-Si bonds break and reform continuously during large plastic deformation in *a*-Li$_x$Si alloys with low concentrations [51]. However, the atomic processes controlling

plasticity in *a*-Li_xSi alloys and the atomic-scale mechanisms responsible for the lithiation-induced drop in yield stress are not completely understood.

There would be therefore a need to completely understand the yield behavior of *a*-Li_xSi alloys. In this section, we investigate the details on the yield behavior of *a*-Li_xSi, with x equal to 0.125 and 3.75, using MD simulations. We compute the yield and fracture strengths of *a*-Li_xSi under mechanical loading conditions, including biaxial compression, uniaxial tension and compression. We also calculate the yield surfaces of *a*-Li_xSi for biaxial stress states, and the calculated yield surfaces show an asymmetry on the magnitudes of yield stress in tension and compression. Following these calculations, we discuss the plasticity carrier in *a*-Li_xSi and the asymmetry in the yield surfaces by linking atomistic-level mechanisms in metallic glasses and covalent glasses.

2.4.1 Biaxial Compression, Uniaxial Tension, and Uniaxial Compression

Biaxial compression

One effective method of measuring the yield stress of *a*-Li_xSi is to measure the stress generation in an *a*-Si thin film on an inactive substrate in lithiation/delithiation cycling [19, 55, 102]. During the lithiation of a constrained thin film, compressive stress is generated owing to concurrent electrochemical reaction of Li with Si and mechanical deformation of *a*-Li_xSi, both of which involve the similar atomic processes of bond breaking, switching, and reformation. MD modeling and simulations of lithiation in an *a*-Si thin film and a discussion on simulation results will be provided in Section 3.2.

Alternatively, one can evaluate the mechanical properties of *a*-Li_xSi alloys through a sequence of chemical lithiation followed by mechanical deformation. That is, *a*-Si is first lithiated to a specific Li concentration under a stress-free condition, and then is subjected to biaxial compression while keeping the Li concentration fixed. To correlate the yield stress obtained from the lithiation of Si thin film with that from the pure *mechanical* deformation of *a*-Li_xSi alloys, one needs to define the strain at the "yield point" in the latter case.

To simulate the mechanical deformation, we take a supercell of *a*-Li_xSi, which is generated through the pre-described melt-quench method, as a representative volume element (RVE). This supercell is subjected to period boundary conditions. It is free to expand in one direction and subjected to biaxial compression in the other two directions. Figure 2.6 (a) shows the simulated stress-strain curves of biaxial compression under a strain rate of 5×10^8 s^{-1} at 300 K with several representative Li concentrations. A salient feature in these stress-strain responses is the yield point phenomenon, featuring the peak stress, load drop, and steady-state flow with a limited strain hardening. Notably, the degree of yield drop varies with the Li content. In Li-poor phases, the high peak of yield stress is usually observed and the associated load drop is pronounced. The large peak stress indicates the need of a high load to create enough plastic carriers during the early stage of deformation, a process usually referred to as rejuvenation for creating an amorphous structure amenable to plastic flow [101]. In contrast, the yield point phenomenon is less pronounced in the Li-rich phases, which implies the existence of a high fraction of easily flowing components and thus lends a support to constitutive modeling of the Li-rich phase as a visco-plastic solid [22].

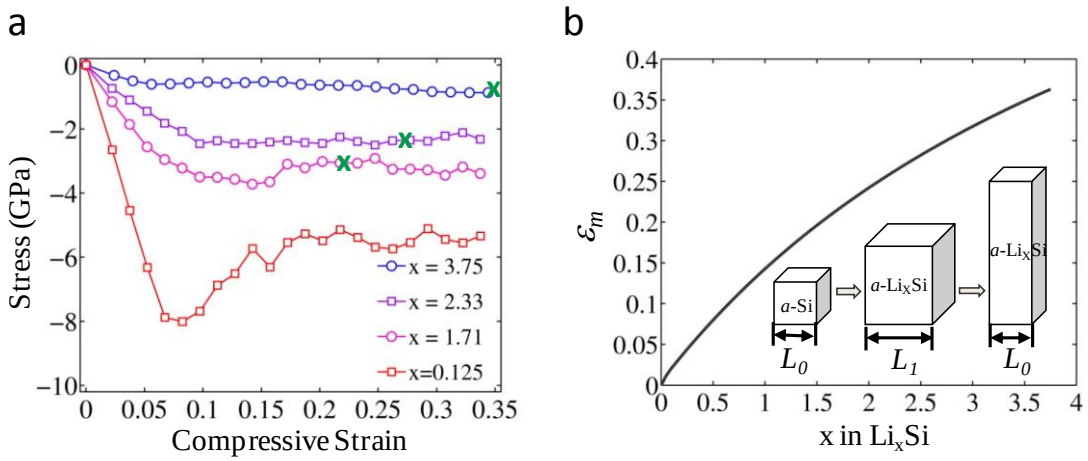

Figure 2.6 MD simulations of biaxial compression of a representative volume element (RVE) of *a*-Li_xSi alloys. (a) Stress-strain curves at four Li concentrations. The green cross symbol indicates the respective yield strengths of σ_y^m, which correspond to the compression strain, ε_m, specified in (b) for each selected concentration. (b) Strain-composition curve for *a*-Li_xSi alloys. The inset describes a sequential loading mode, which consists of a stress-free chemical expansion from *a*-Si with an initial size of L_0 to *a*-Li_xSi with a size of L_1, and a biaxial compression on *a*-Li_xSi under an external compression strain of $\varepsilon_m = (L_1 - L_0)/L_1$, so that *a*-$Li_xSi$ has the same in-plane dimensions as *a*-Si.

Although the detailed atomic processes underlying the yield point phenomenon in *a*-Li_xSi alloys warrant further study, we focus on extracting the yield strength of σ_Y^m from the above *mechanical* (*m*) deformation of biaxial compression. The results enable us to correlate σ_Y^m with the yield strength of σ_Y^{cm} evaluated from thin-film lithiation that involves a concurrent *chemomechanical* (*cm*) process (Section 3.2). Note that in order to determine σ_Y^m at a specific Li concentration from the stress-strain curve, one needs to determine the corresponding strain at yielding, as shown in Figure 2.6 (b). Here we define the strain at yielding as $\varepsilon_m = (L_1 - L_0)/L_1 < 0$, where L_1 and L_0 respectively denote the supercell size of the stress-free *a*-Li_xSi and the initial *a*-Si, as schematically

shown in the inset of Figure 2.6 (b). Application of such a strain at yielding to *a*-Li_xSi cancels the in-plane expansion induced by the stress-free lithiation, consistent with the boundary condition of rigid in-plane constraints during thin-film lithiation. Given ε_m at a specific Li concentration, we determine the associated compressive yield strength σ_Y^m from the biaxial compressive stress-strain curve in Figure 2.6 (a). As indicated by the cross symbols in Figure 2.6 (a), σ_Y^m corresponds to the characteristic plateau stress of plastic flow.

The above yield strengths are at variance with previous reports of simulations [47, 48] and experiments [51]. The discrepancy of our computed yield strengths with references [47, 48] arises mainly from the different definitions of yield strength. As shown in Figure 2.6 (a), the stress-strain curve from MD simulation usually exhibits the yield point phenomenon, which involves a peak stress that is followed by stress drop (i.e., softening) and subsequent steady state flow at a plateau stress. The value of the yield peak depends sensitively on various factors such as the applied strain rate and temperature, sample preparation (e.g., annealing temperature and rate), as well as chemical composition of the alloys. The conventional 0.2% offset yield stress, as defined by Cui *et al*. [48], is closely correlated with the yield peak, thus being dependent on the aforementioned factors. On the other hand, the stress-controlled energy minimization is performed by Zhao *et al*. [47], and the yield strength is defined as the critical stress at the load drop or strain jump, which is also closely correlated to the yield peak. In addition, the simulations in reference [47] are performed in a rather small amorphous system with a highly non-uniform atomic structure and thus the results are likely a function of system size, an effect that has not been studied systematically by Zhao *et al*. [47].

In contrast, we define the yield strength as the steady state flow stress, which is not so sensitive to the value of yield peak. More importantly, our definition facilitates a correlation of the yield strength between biaxial deformation and thin film lithiation. This is because Figure 2.6 (b) shows that the typical compressive strains during thin-film lithiation are mostly larger than 10%, and hence the steady state flow stress in biaxial deformation, which prevails at large strains, is more relevant to the yield strength in thin film lithiation. In addition, the steady state flow stress obtained in our simulations is insensitive to the system size, which ranges from 3nmx3nmx3nm (~2,000 atoms) to 6nm x 6nm x 6nm (~16,000 atoms).

Hertzberg *et al*. [16] report the experimental measurements of hardness of *a*-Li_xSi alloys using the indentation method. Due to the well-known strain rate effects on MD, it is not possible to quantitatively compare MD with experimental results. However, we note that while these measurements represent the first experimental effort to quantify the yield strength of *a*-Li_xSi alloys, there are several uncontrolled factors in experiments, such as uncertainty on the spatial distribution of lithium considering the recently discovered two-phase mechanism in the first lithiation of *a*-Si [44, 47], as well as uncertainty on the structural and composition changes when the lithiated samples were transferred to mechanical testing. Hence, the well-controlled experimental studies are critically needed in the future research.

Uniaxial tension

In addition to the biaxial compression of *a*-Li_xSi, we conduct the MD studies of uniaxial deformation. Uniaxial tension of *a*-Li_xSi nanowires is simulated by applying a

constant strain rate of 10^8 s^{-1} at 300 K. Figure 2.7 (a) shows the tensile stress-strain curves for a Li-poor (*a*-$Li_{0.125}Si$) and a Li-rich (*a*-$Li_{3.75}Si$) nanowire, both of which exhibit the initially linear and subsequently non-linear responses followed by a load drop. The linear response corresponds to elastic deformation, with Young's moduli fitted as 65 GPa for *a*-$Li_{0.125}Si$ and 12 GPa for *a*-$Li_{3.75}Si$. Evidently, the nanowires undergo elastic softening with increasing Li concentration. This result is indicative of the stiffer bonding of Si-Si than Li-Li, which is consistent with the previous experimental measurements [48] and first-principles calculations [36]. Compared to that of the *a*-$Li_{0.125}Si$ nanowire, the stress-strain curve of *a*-$Li_{3.75}Si$ exhibits a considerably larger range of nonlinearity beyond the proportional limit. Such a difference can be ascribed to the existence of an increasing fraction of easily flowing components with increasing Li concentration, an effect that is also responsible for different yield point responses during biaxial compression, as discussed earlier.

Unique to uniaxial tension, the nanowires are prone to necking instability. It has been previously understood that the onset of necking arises from the insufficient strain hardening to compensate for the geometrical softening associated with the reduction of cross-sectional area during tensile elongation [47]. Since the amorphous solid usually lacks strain hardening as shown earlier in biaxial compression, the neck grows in both *a*-$Li_{0.125}Si$ and *a*-$Li_{3.75}Si$ nanowires (Figure 2.7 (b) and (c)), causing fracture in the necked region. Because the associated load drop prevents an extensive plastic flow, uniaxial tension is not an effective loading mode to study the post-yielding behavior. Nevertheless, MD results furnish an estimate of the ultimate tensile strength of 4.7 GPa and 0.5 GPa for *a*-$Li_{0.125}Si$ and *a*-$Li_{3.75}Si$, respectively. The corresponding failure strains are similarly

around 13%. Because of the high strain rate and short relaxation time in MD, the predicted fracture stress and strain of *a*-$Li_{3.75}Si$ nanowires represent the upper limit of experimental results from the tensile testing of lithiated Si nanowires [47]. In addition, we note that the *a*-$Li_{0.125}Si$ nanowire exhibits an abrupt load drop, as opposed to a gradual decrease in *a*-$Li_{3.75}Si$. This difference in the post-necking response can be attributed to the relatively high elastic stiffness of the *a*-$Li_{0.125}Si$ nanowire, which results in a large elastic energy release to drive a sharp load drop in the fracture process. Our MD simulations also show that the slope of the descending stress-strain curve is sensitive to the applied strain rate, with a faster load drop at a lower strain rate.

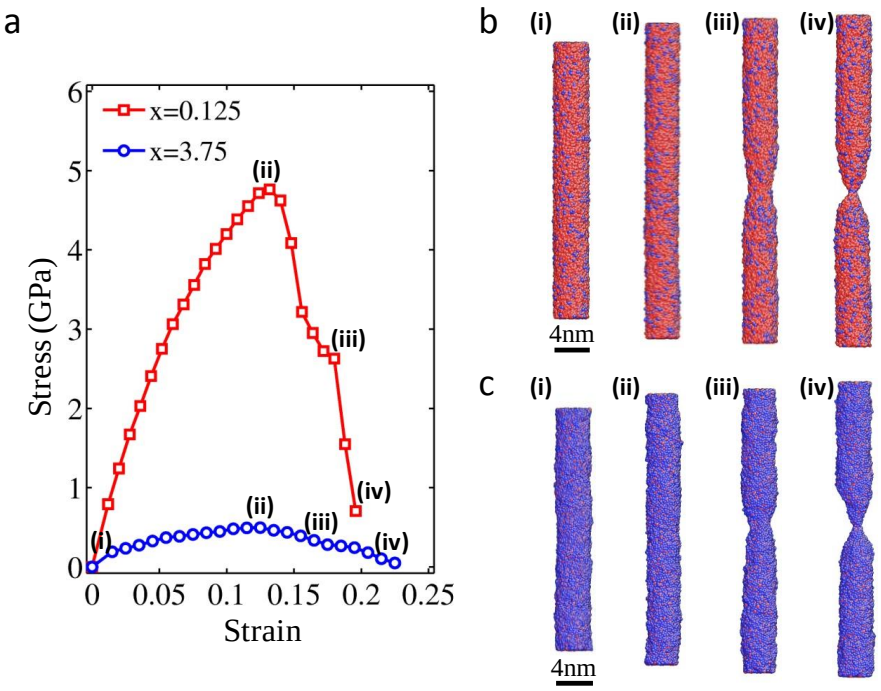

Figure 2.7 MD simulations of uniaxial tension of *a*-Li_xSi nanowires. (a) Engineering stress-strain curve for both the representative Li-poor (*a*-$Li_{0.125}Si$) and Li-rich (*a*-$Li_{3.75}Si$) nanowires. (b) Atomic structures of an *a*-$Li_{0.125}Si$ nanowire at the state of (i) zero stress, (ii) maximum stress

(before the onset of necking), (iii) severe necking and (iv) fracture. (c) Same as (b) except for an *a*-$Li_{3.75}Si$ nanowire.

Uniaxial compression

In recent years, nanopillar compression has emerged as a popular and effective means of testing the mechanical properties of small-volume materials [103-106]. Compared to uniaxial tension, it avoids the necking instability and thus enables the study of both yield strengths and post yielding properties. Figure 2.8 (a) shows the simulated stress-strain curves of uniaxial compression for *a*-$Li_{0.125}Si$ and *a*-$Li_{3.75}Si$ nanopillars under a strain rate of 5×10^{8} s^{-1} at 300 K. Similar to the nanowires under uniaxial tension, the compressed nanopillars undergo the initial elastic deformation. The fitted Young's moduli for *a*-$Li_{0.125}Si$ and *a*-$Li_{3.75}Si$ are consistent with those in tension. Moreover, the magnitude of the flow stress is close to that of the ultimate strength in the tensile tests for both *a*-$Li_{0.125}Si$ and *a*-$Li_{3.75}Si$.

In contrast to the biaxial compression of a RVE as shown in Figure 2.6, the yield drop phenomenon disappears in the Li-poor nanopillars of *a*-$Li_{0.125}Si$ under uniaxial compression at 300K. It has been previously shown that the magnitude of the peak yield stress and the sharpness of the associated load drop in amorphous solids are controlled by the interplay of the annealing rate during sample preparation and the applied strain rate during deformation [101], which respectively controls the amount of the pre-existing and deformation-induced plastic flow carriers. However, both the annealing and strain rates are the same in our simulations of biaxial compression and uniaxial compression. The major difference is that nanopillars have free surface while the RVE with periodic boundary conditions does not. Hence, we attribute the absence of the yield drop

phenomenon in nanopillar compression to the effect of free surface, *i.e.*, a large number of surface dangling bonds enhance plastic flow and thus suppress the yield peak. In addition, the simulated nanopillars experience the steady flow (Figure 2.8 (a)) with a large range of homogenous compression (Figure 2.8 (b) and (c)), rather than the development of a dominant, localized shear band that would cause premature failure and load drop. This phenomenon can be attributed to the relatively small size of our nanopillars that effectively prevents the shear band formation, a well-known sample size effect on deformation in amorphous solids [107]. Lastly, we note that the above MD study of uniaxial deformation in terms of free-standing nanowires and nanopillars, instead of RVEs, is motivated by the consideration that these simulations could provide valuable references and insights for future experiments on *a*-Li_xSi nanowires and nanopillars.

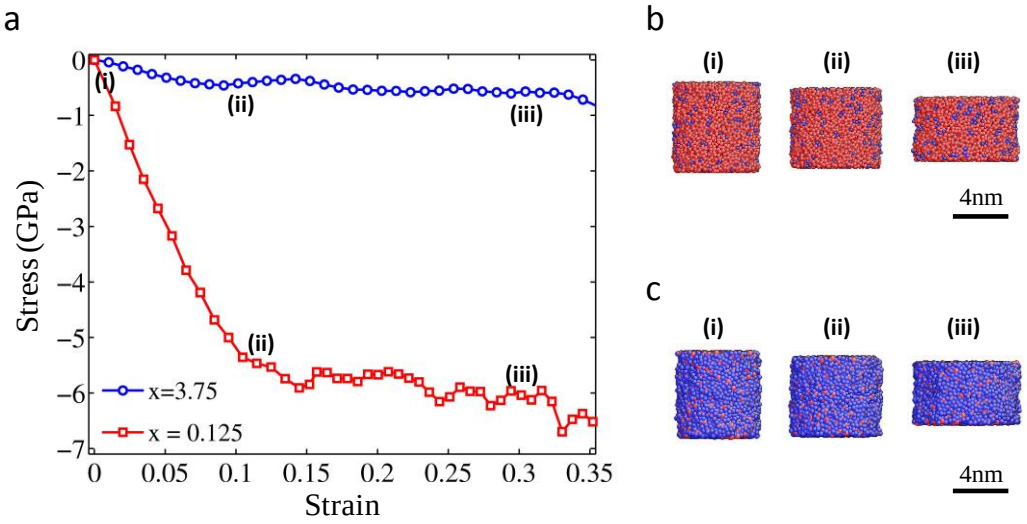

Figure 2.8 MD simulations of uniaxial compression of *a*-Li_xSi nanopillars. (a) Engineering stress-strain curve for both the representative Li-poor (*a*-$Li_{0.125}Si$) and Li-rich (*a*-$Li_{3.75}Si$) nanopillars. (b) Atomic structure of an *a*-

$Li_{0.125}Si$ nanopillar at the compressive strain of (i) zero, (ii) 10%, and (iii) 30%. (c) Same as (b) except for an *a*-$Li_{3.75}Si$ nanowire.

2.4.2 Biaxial Yield Surface

Finally, we summarize the simulated results of yield strengths in Figure 2.9 in terms of the biaxial yield surface in the true stress space, in order to provide a unified perspective on the mechanical properties of a-LixSi alloys. Besides the yield strengths obtained in Sections 2.4.1 and 3.2, we include in Figure 2.9 the additional results of flow strengths in uniaxial tension and compression of RVEs. Despite the limited data set, several salient features emerge. First, plastic yielding depends sensitively on the Li content. This has been demonstrated through a Li-poor phase of *a*-$Li_{0.125}Si$ in Figure 2.9 (a) and a Li-rich phase of *a*-$Li_{3.75}Si$ in Figure 2.9 (b). Such a difference arises because the plastic flow characteristics of the former are dominated by the strong covalent Si-Si bonds but the latter by the weak metallic Li-Li bonds. Second, the asymmetry in tension and compression exists, as seen in uniaxial deformations from Figure 2.9 (a) and (b). Such asymmetry is a hallmark of amorphous solids [108], manifesting the effect of normal stress on shear strength. It is observed in both the Li poor and rich *a*-Li_xSi alloys, despite the drastically different structures and bonding characteristics. That is, the directional, covalent network of Si dominates in the former, as opposed to the randomly close-packed metallic Li in the latter. The initial yielding behavior in an amorphous material is expected to have a relatively high sensitivity on pressure, since the nucleation of plasticity carriers such as shear transformation zones is usually accompanied by the dilatation of atomic structure. However, our yield strength is defined as the steady state flow stress at strains greater than 10%, and its pressure-dependence can be different from

that of the initial yielding. Specifically, when a system is deformed to large strains, it should have already generated a significant amount of plasticity carriers. It follows that the system volume is not necessarily required to change significantly to sustain the steady state flow at high strains, such that plastic yielding becomes less sensitive to pressure, as observed in our MD results. Third, the biaxial compression yield strength is a little higher than the uniaxial one, owing to the geometrical confinement effects on plastic deformation. Fourth, Figure 2.9 (c) shows that the normalized biaxial yield surfaces are similar between the *a*-$Li_{0.125}Si$ and *a*-$Li_{3.75}Si$ phases, despite their dominant atomic bonding characteristics are drastically different. Overall, all the aforementioned features are fundamentally governed by the nature of atomic bonding in *a*-Li_xSi alloys, and the unique mechanical properties of *a*-Li_xSi alloys reflect the effective behavior of the mixed covalent and metallic bonds with different fractions and spatial arrangements [103].

Regarding the plastic properties, the previous study shows that the liquid-like *a*-Si contains a relatively large number of flow defects facilitating plastic deformation [101]. Hence, the yield strengths predicted from our *a*-Si should represent the upper limit at low Li concentrations. However, we emphasize that the initial structures in all of our simulations, including both the lithiation of thin film and the mechanical loading of *a*-Li_xSi alloys, are generated using the same protocol of melting-quenching and the resultant structures enable a self-consistent study of how the Li composition affects the mechanical properties of *a*-Li_xSi alloys. Nevertheless, the effects of different amorphous structures and mass densities on the yield strength of *a*-Li_xSi alloys warrant a more detailed study in the future.

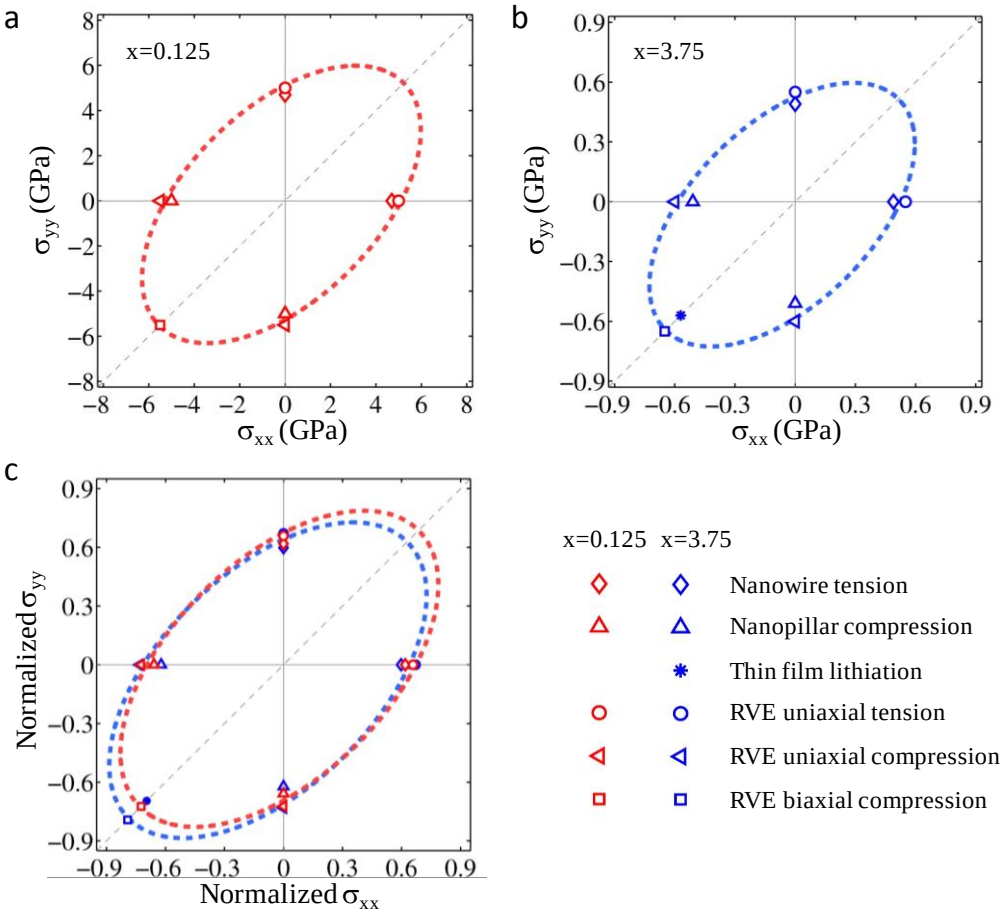

Figure 2.9 Biaxial yield surface of a-LixSi alloys. (a) Yield surface in true stress space of a Li-poor phase of *a*-$Li_{0.125}Si$ under various loading modes. All the three loading modes on RVEs are performed under a strain rate of 5×10^{8} s^{-1} at 300 K. Reflection symmetry is employed about the line of $\sigma_{xx} = \sigma_{yy}$, since amorphous solids are isotropic. The dashed line is drawn to guide eyes. (b) Same as (a) except for a Li-rich phase of *a*-$Li_{3.75}Si$. (c) Results in (a) and (b) are normalized by the respective value of the long radius of the ellipse. (Simulation details and results of thin film lithiation are provided in Section 3.2.)

Evolution of atomistic structures during deformation

We study the atomic-level mechanisms of mechanical relaxation by analyzing the evolution of atomic coordination numbers as a function of tensile strain. The evolution of

atomic coordination numbers during deformation provides basic information on the atomistic structural changes under mechanical loading, which can be correlated to the dominant bonding characteristics. In Figure 2.10 (a) and (b), we compare the coordination numbers of Si and Li atoms for *a*-$Li_{0.125}Si$ and *a*-$Li_{3.75}Si$ alloys under uniaxial tension at $\varepsilon = 0$ and 0.4, respectively. In both *a*-$Li_{0.125}Si$ and *a*-$Li_{3.75}Si$, the number of Si atoms with small coordination numbers increases, and the number of Si atoms with large coordination numbers decreases. In addition, the change in the coordination number distribution of Li atoms in *a*-$Li_{0.125}Si$ is more obvious than that in *a*-$Li_{3.75}Si$. These results indicate (a) Si-Si and Si-Li bonds break during deformation; (b) in *a*-$Li_{0.125}Si$, most Li atoms are located in the interstitial sites of the covalent Si network, and the structural relaxation under high strain occurs mainly through breaking and reformation of covalent Si-Si bonds; (c) in *a*-$Li_{3.75}Si$, a large fraction of metallic Li atoms and their high mobility enable the effective bond switching and reforming to accommodate the imposed mechanical strain.

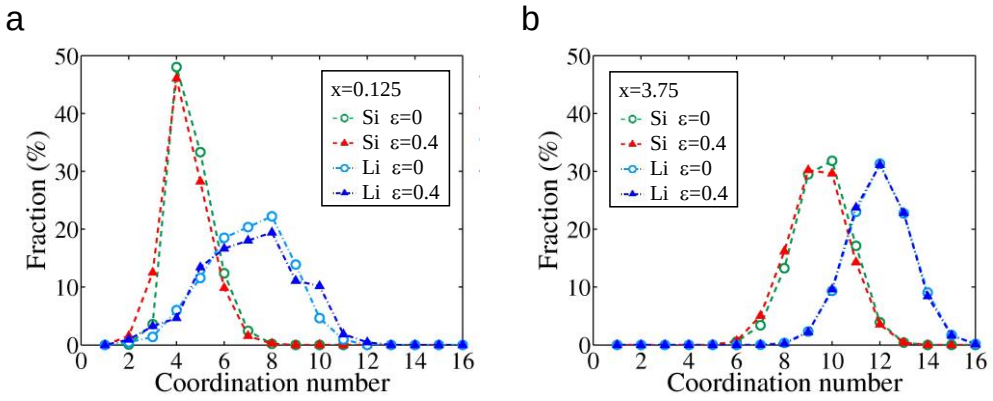

Figure 2.10 Evolution of coordination numbers under uniaxial tension. (a) Distribution of the coordination numbers of Si and Li atoms in *a*-$Li_{0.125}Si$ at the strain of $\varepsilon = 0$ and 0.4. (b) Same as (a) except for *a*-$Li_{3.75}Si$.

Plastic Relaxation and Plasticity Carrier

Irreversible stress relaxation events during deformation in random covalent network materials, e.g. *a*-Si, and metallic glasses have been investigated through atomistic simulations [100, 105]. Although there are apparent differences in composition, atomic packing and bonding between covalent network materials and metallic glasses, irreversible shear events in both of the two kinds of amorphous materials exhibit similar features [101, 108]. In *a*-Si, atomic local environment with "liquid-like" mass is considered as plasticity carriers, and large shear propagation triggered by a local shear event is observed in atomistic simulations using the Stillinger-Weber (SW) potential [100]. In metallic glasses, local shear transformation zones and the regions with free volume are taken as plasticity carriers, and subsequent autocatalytic propagations of shear transformation zones have been observed in atomistic simulations. In this work, we consider *a*-Li_xSi as an intermediate state between *a*-Si and *a*-Li. *a*-Li_xSi with a very low Li concentration may exhibit a random-covalent-network behavior, while Li-rich *a*-Li_xSi tends to be similar to metallic glasses. The bonding in *a*-Si is direction-sensitive. The insertion of Li atoms results in metallic-covalent mixed bonding, and with increasing Li concentration, Li-Li metallic bonding becomes dominant in *a*-Li_xSi. Such a transition in bonding leads to changes in the atomic environment of local shear events.

2.5 Fracture mechanism: A Brittle-To-Ductile Transition

During the charge/discharge cycling, Si undergoes large volume change, leading to fracture and cracking in Si anodes [3, 6, 7, 33, 41]. The fracture behavior of Si anodes has gained increasing attention in both theoretical [17, 28, 29, 35, 39, 109-111] and

experimental works [46, 112]. An important question in these works is: What is the criterion of fracture in lithiated Si? To resolve this question, we first need to understand the fracture mechanisms in lithiated Si, *a*-Li_xSi. In this section, we report atomistic simulations of precracked *a*-Li_xSi samples under tensile loading, with emphasis on whether fracture occurs in a brittle or ductile manner.

We study fracture mechanisms in two *a*-Li_xSi alloys, *a*-$Li_{0.5}Si$ and *a*-$Li_{2.5}Si$, in which bonding environments are covalent-bond dominant and metallic-bond dominant, respectively. Atomic interactions are modeled by the ReaxFF described in Section 2.1. The two *a*-Li_xSi samples are prepared from a melting-and-quenching simulation with a quench rate of 2×10^{12} K s^{-1}. The samples are generated in a stress-free condition, with final dimensions of ~16 nm x 10 nm x 1.5 nm (Figure 2.11). A sharp pre-crack with a length of ~3 nm is made to facilitate fracture and cracking behavior. The samples are then loaded in tension with a strain rate of 5×10^8 s^{-1}. During the simulations of tension and fracture, temperature is maintained at 5 K to reduce the thermal effects. Periodic boundary conditions are applied along the loading and the thickness directions. The time step for all the MD simulations is 1 fs. The simulations are performed under both the plane-strain condition and the plane-stress condition. Here, only the results for the plane strain condition are presented and discussed because the simulation results for these two conditions do not exhibit fundamental difference in fracture mechanisms.

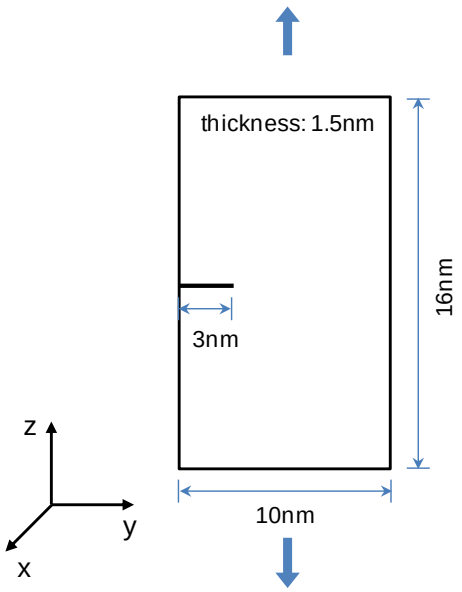

Figure 2.11 *a*-Li_xSi sample dimensions in MD simulations. Periodic boundary conditions are applied along x and z directions. The sample is loaded in tension along z direction.

The fracture simulations find two distinct types of fracture behavior in the precracked *a*-Li_xSi samples under tensile loading. Figure 2.12 shows selected snapshots of fracture simulations of *a*-$Li_{0.5}Si$ and *a*-$Li_{2.5}Si$ precracked samples. The simulations reveal two distinct types of fracture behavior: brittle fracture through crack propagation in *a*-$Li_{0.5}Si$ (Figure 2.12 (a)) and ductile fracture through crack-tip blunting in *a*-$Li_{2.5}Si$ (Figure 2.12 (b)). Tensile strain causes bond breaking in the *a*-$Li_{0.5}Si$ sample, and such bond breaking generates nanoscale voids ahead of the crack tip. Further bond breaking results in void coalescence and crack propagation. We note the crack surface is not atomically sharp at nanoscale, as an amorphous solid lacks long range order or periodicity in its atomic structure. In addition, crack propagates through a void nucleation and coalescence mechanism, and the propagation direction is influenced by local shear around the crack tip. Then, the crack in the *a*-$Li_{0.5}Si$ sample exhibits a zigzag feature, as

shown in Figure 2.12 (a). In contrast to *a*-$Li_{0.5}Si$, *a*-$Li_{2.5}Si$ exhibits continuous crack-tip blunting under applied tensile loading Figure 2.12 (b). This blunting occurs due to extensive shear banding developed around the crack tip region in the sample. Comparing with crack propagation in *a*-$Li_{0.5}Si$, crack-tip blunting in *a*-$Li_{2.5}Si$ dissipates a large amount of energy, resulting in high fracture toughness in Li-rich *a*-Li_xSi. These two fracture mechanisms have been reported for other amorphous solids [113, 114].

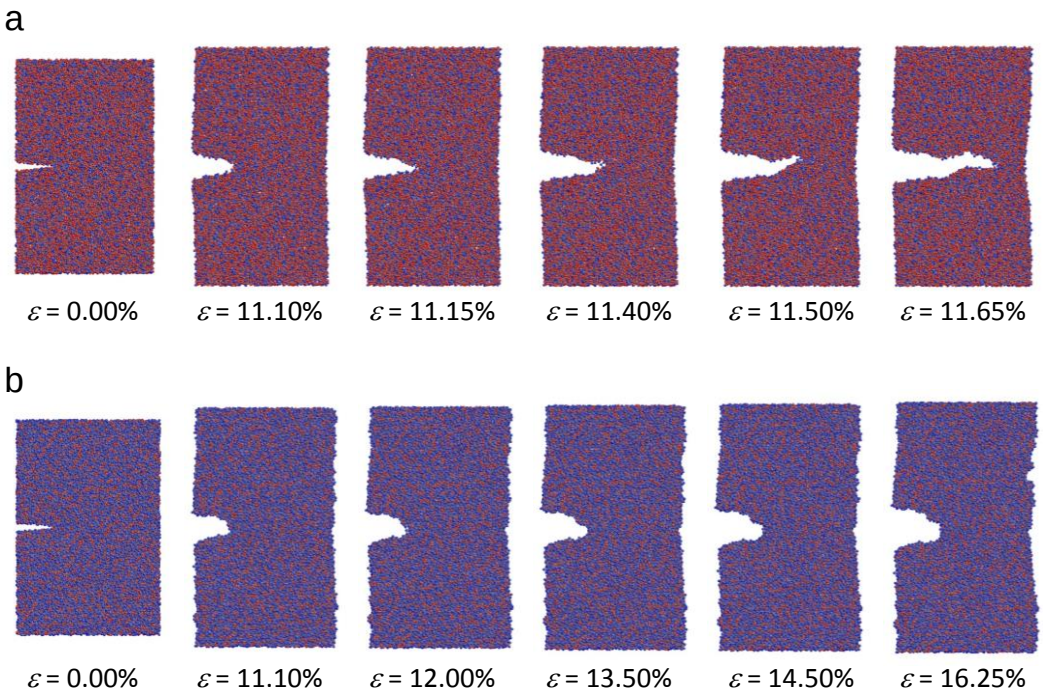

Figure 2.12 Fracture mechanisms in Li-poor and Li-rich *a*-Li_xSi precracked samples. Red spheres represent Si atoms, while blue ones represent Li atoms. (a) Crack propagation in an *a*-$Li_{0.5}Si$ sample with a precrack at various applied tensile strains. (b) Crack-tip blunting in an *a*-$Li_{2.5}Si$ sample with a precrack at various applied tensile strains.

The MD simulations reveal a brittle-to-ductile transition in fracture mechanisms for *a*-Li_xSi, which is Li-concentration dependent. In a Li-poor lithiated Si phase, crack grows through void nucleation and coalescence, resulting in brittle fracture. In a Li-rich

phase, extensive shear banding occurs in the crack tip region, resulting in ductile fracture. The origin of such a brittle-to-ductile transition in the fracture mechanisms is that the lithiation of Si induces a gradual transition from covalent to metallic bonding in *a*-Li_xSi, as described in Sections 2.2 and 2.4. Competition between these two fracture mechanisms in *a*-Li_xSi is related to whether cavitation or shear banding dominates in the region ahead of the crack tip. A further interest in the fracture mechanisms is in understanding extrinsic controlling factors for the propensity of *a*-Li_xSi for void nucleation and coalescence or shear banding in front of the crack tip, and this work warrants a more detailed study. In addition to the fracture mechanisms, fracture toughness and energy, which are important parameters for modeling and design of Si-based electrodes, can be calculated by performing MD simulations.

2.6 Summary

We have conducted an atomistic study of the mechanical behavior of *a*-Li_xSi alloys by molecular dynamics with a reactive force field (ReaxFF). We have simulated a variety of mechanical deformation processes, including biaxial compression, uniaxial tension and compression. The results reveal the effects of stress states and compositions on mechanical properties and fracture mechanisms, which are correlated to the atomic bonding characteristics. The mechanical behavior of *a*-Li_xSi includes elastic softening, plastic softening, asymmetry in biaxial yield surface, and a brittle-to-ductile fracture transition. Since the *a*-Li_xSi alloys undergo a large range of change in composition during electrochemical cycling, their mechanical behavior is extremely rich, exhibiting the features of both covalent and metallic amorphous solids. The detailed analyses of the

molecular dynamics results in this section provide the atomistic insights for understanding the mechanical behavior and designing mechanical testing experiments on *a*-Li_xSi alloys.

3 CHEMO-MECHANICS OF SI ELECTRODES: AN ATOMISTIC STUDY

Recent electrochemical charging/discharging experiments have shown that during lithiation Si electrodes undergo dramatic volume expansion, anisotropic expansion, lithiation-induced stress generation, and fracture events [3, 6-8, 11-14, 17, 22, 25, 33, 41, 43, 54]. Understanding such chemo-mechanical behavior of the Si electrodes is critical to reducing performance degradation in high-capacity electrodes. In this chapter, we study the chemo-mechanical behavior of Si electrodes during the first lithiation of *c*-Si nanopillars (Section 3.1) and the subsequent lithiation of an *a*-Si thin film after the first cycle (Section 3.2). We calculate lithiation-induced stresses by performing MD simulations with a ReaxFF. By analyzing the results, we obtain an understanding of (1) surface fracture in *c*-Si nanopillars and (2) stress measurements in *a*-Si thin film lithiation experiments.

In Section 3.1, we simulate the lithiation of *c*-Si nanopillars, which features a two-phase mechanism and anisotropic expansion. The MD simulation results show the development of tensile hoop stress at the pillar surface and the directionality of the surface stress development. The work provides mechanistic insights into the mechanical failure of Si electrodes. In Section 3.2, we simulate the lithiation of an *a*-Si thin film and compare the yield strengths obtained from thin film lithiation with those from pure mechanical loading. The results provide mechanistic insights for interpreting experiments on *a*-Li_xSi, understanding the chemo-mechanical behavior and designing mechanical testing.

3.1 Chemo-Mechanical Behavior of *c*-Si Nanopillars

TEM experimental characterizations have revealed that the first electrochemical lithiation process of *c*-Si occurs in a two-phase mechanism [17-19]. In the mechanism, a sharp phase boundary with a thickness of ~1 nm exists between pristine *c*-Si and lithiated products, *a*-Li_xSi alloys, and the lithiation kinetics are controlled by the migration of the *c*-Si/*a*-Li_xSi phase boundary, which proceeds through the movement of ledges on close-packed atomic planes. The *a*-Li_xSi alloys are generated through layer-by-layer peeling of the {111} atomic facets from a *c*-Si lattice. Such a ledge mechanism results in orientation-dependent mobility of the phase boundary.

The first lithiation of *c*-Si nanostructured electrodes, such as nanopillars and nanoparticles, are accompanied by dramatic volumetric expansion and anisotropic swelling. Such expansion and swelling causes fracture and even pulverization of the electrodes. The underlying failure mechanisms have attracted research efforts in analytical modeling and numerical simulations [31, 33, 37, 39, 51, 111, 115-117]. These works develop continuum approaches based on elasticity- and plasticity theories for capturing lithiation-induced stress generation. To link the electrochemical reaction at the phase boundary to continuum-level physical processes, the approaches assume that (1) lithiation induces elastic and/or plastic deformation at the *c*-Si/*a*-Li_xSi phase boundary, and (2) the total strain is decomposed into a chemical part and a mechanical part. The approaches worked well for explaining surface cracking and size-dependent fracture in the lithiation of *c*-Si nanopillars and nanoparticles. However, these approaches are challenged by a thermodynamic model because of an analysis on stress relaxation mechanisms during electrochemical lithiation [40]. Then, the following questions may

arise: How to further validate the modeling and simulation results? And do the continuum models have major limitations when predicting chemo-mechanical behavior in two-phase lithiation?

To bridge the gap between the atomic-scale processes of two-phase lithiation in *c*-Si and the continuum-based approaches, we performed atomistic simulations with a reactive force field (ReaxFF) developed for lithiated Si using the large-scale atomic/molecular massively parallel simulator (LAMMPS) [98]. The ReaxFF provides accurate descriptions of bonding environment in *a*-Li_xSi systems, and it is capable of capturing the physical properties and the mechanical behavior of *a*-Li_xSi alloys (Chapter 2). In addition, the computational cost of the ReaxFF enables large-scale atomistic simulations, which allow a direct output of lithiation-induced morphological evolution of nanostructured electrodes and associated stress distributions.

In this section, we studied the chemo-mechanical behavior of *c*-Si nanopillars during the first lithiation. We simulate the electrochemical reactions of Li and Si through a Li-insertion protocol, in which Li atoms are inserted into a *c*-Si lattice in a layer-by-layer manner. This protocol is capable of simulating the two-phase lithiation mechanism and the anisotropic mobility of the *a*-Li_xSi/*c*-Si phase boundary. We then examine resulted morphological evolution and stress generation in the nanopillars. The results show the origin of lithiation-induced fracture in *c*-Si nanopillars, demonstrating that the fracture is due to the combined effect of plastic flow, two-phase mechanism, and anisotropic lithiation. This work provides insights into the elasticity/plasticity-based continuum approaches.

3.1.1 Two-Phase Lithiation

Focusing on the effect of two-phase lithiation on the mechanical degradation, we study the chemo-mechanical behavior of a <111>-oriented *c*-Si nanopillar. Recent experiments have revealed anisotropic swelling in *c*-Si nanopillars upon lithiation, with the largest expansion in its <110> directions [25]. However, for a <111>-oriented *c*-Si nanopillar, there are six equivalent <110> directions within the cross section, such that the isotropic lithiation in the nanopillar cross section can be reasonably assumed. With the assumption of isotropic lithiation, we investigate lithiation-induced morphological evolution and stress generation in the nanopillar using atomistic simulations.

The initial configuration of the simulated system is a *c*-Si cylinder. A periodic boundary condition is applied along the axial direction of the cylinder. The simulation is performed in the plane strain condition by fixing the dimension of the simulation box along the cylinder axial direction. To mimic the two-phase lithiation, we develop a Li-insertion protocol, in which the insertion of Li into the *c*-Si lattice proceeds in a layer-by-layer manner, mimicking the two-phase lithiation of a *c*-Si nanopillar. The protocol includes the following steps (Figure 3.1):

1. Calculate the distribution of Li concentration in the current system; determine a target layer, which is to be lithiated in the next step.
2. Randomly insert Li atoms into the target layer, ensuring that the Li atoms are inserted into big spherical voids [30, 51].

3. Relax the structure and the in-plane stresses in the system. During the relaxation simulation, the energy minimization method is used to eliminate the thermal effects.
4. Repeat step 3 multiple times until the system energy reach a local minimum and the in-plane stresses are zero.
5. Repeat steps 1-4 with updated configurations.

An essential feature of this protocol is that Si atoms are dissociated from the *c*-Si lattice through a layer-by-layer manner, as the insertion of Li is based on Li concentration profile. This protocol is capable of forming a core-shell structure in a partially lithiated *c*-Si nanopillar, which consists an *a*-Li_xSi/*c*-Si phase boundary that separates an inner core of *c*-Si with an outer shell of *a*-Li_xSi ($x \approx 3.75$). We note that the simulation using this protocol does not take long-range diffusion into account due to time-scale limitations of atomistic simulations.

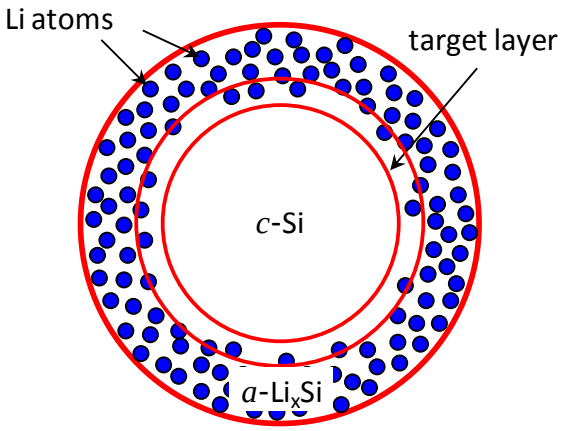

Figure 3.1 Schematic illustration of the Li-insertion protocol for a <111>-oriented *c*-Si nanopillar in the atomistic simulation. Li atoms are inserted into the *c*-Si lattice in a layer-by-layer manner, mimicking the two-phase electrochemical lithiation process.

Figure 3.2 shows Si atoms on a close-packed {111} atomic plane are dissociated from the pristine *c*-Si lattice in the simulation. During lithiation, Li atoms first occupy interstitial sites in the *c*-Si lattice near the *a*-Li_xSi/*c*-Si phase boundary. As more Li atoms are inserted into the target layer, the Si atoms in this layer break away from the *c*-Si lattice. When local Li concentration in the layer reaches a critical value, at which $x \approx 3.75$, most Si-Si covalent bonds in this target layer are disrupted, resulting in the scenario that several Li atoms enclose a single Si atom or a Si-Si pair near the phase boundary.

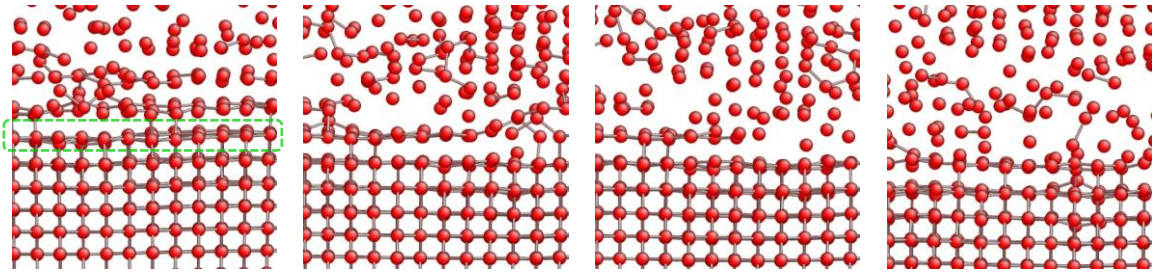

Figure 3.2 Dissociation of Si atoms on a close-packed {111} atomic plane from the *c*-Si lattice. Si atoms are represented by red spheres, while Li atoms are not displayed. During lithiation, the Si atoms enclosed by the green dotted line are dissolved into the *a*-Li_xSi phase, indicating layer-by-layer removal of Si atoms.

Figure 3.3 shows the morphological evolution of a <111>-oriented *c*-Si nanopillar in the lithiation simulation. The initial radius of the nanopillar is 50Å. Upon lithiation, each configuration of the nanopillar includes a pristine *c*-Si core and an *a*-Li_xSi shell with $x \sim 3.75$, separated by a phase boundary with a thickness of ~1 nm. Here, we note that the assumed isotropic lithiation results in a circular *a*-Li_xSi/*c*-Si phase boundary instead of a hexagonal one. Therefore, the evolution of the cross section does not exhibit anisotropic swelling, and the distribution of lithiation-induced stress should be uniform along the hoop direction.

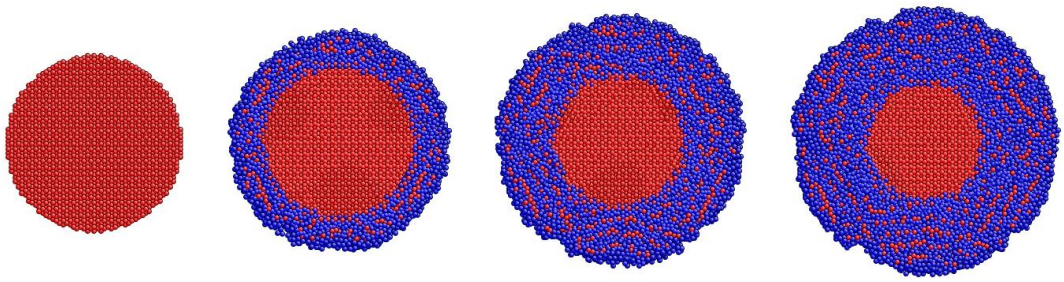

Figure 3.3 Morphological evolution of a <111>-oriented *c*-Si nanopillar in the simulation, in which isotropic lithiation is assumed. The development of the cross section indicates dramatic volumetric expansion. Red and blue spheres represent Si and Li atoms, respectively.

We then examine stress generation in the nanopillar during the simulated two-phase electrochemical lithiation. As the stress has axial symmetry with respect to the central axis of the nanopillar, we focus on stress distribution along the radial direction. In order to determine stress components at a spatial point, we first need to define volumes for the stress calculation. We consider a through-thickness bin in the system that which has a center located at the point. The bin has in-plane dimensions of 6 Å x 6 Å and contains ~60 atoms. Then, we compute stress components in the bin in Cartesian coordinates and transformed the stress into cylindrical coordinates. The computed stress is considered as that at the center of the bin.

Figure 3.4 (a) and (b) report the distribution of both hoop stress and hydrostatic stress in the <111>-oriented nanopillar at an early stage of lithiation. We highlight three regions in the nanopillar: a pristine *c*-Si core, an *a*-Li_xSi shell, and a phase boundary between the core and the shell. The shell and the phase boundary are under hoop compressive stress, while the core is dominantly under hydrostatic tension.

Figure 3.5 (a) and (b) report the radial distribution of hoop stress and hydrostatic stress at an intermediate stage of lithiation. The results show that both the hoop stress in the surface layer of the nanopillar becomes tensile, indicating that the *a*-Li_xSi shell undergoes a transition from hoop compression to hoop tension. Such a change in the sign of the hoop stress is due to the "push-out" effect [118, 119], which is the lithiation-induced expansion of the material at the phase boundary pushes out the a-Li_xSi shell. This "push-out" action associated with the curved phase boundary causes further displacement of the material in the *a*-Li_xSi shell along the outward radial direction and simultaneously stretches the material along the hoop direction. As lithiation proceeds, the push-out effect becomes large enough, so as to reverse the initial hoop compression in the surface layer to hoop tension.

Figure 3.6 reports the hoop stress and hydrostatic stress in the nanopillar along its radial direction in a later lithiation stage. The results indicate that as the phase boundary continues moving toward the central axis of the nanopillar, the *a*-Li_xSi shell is dominantly under tension, and the magnitude of hydrostatic stress at the phase boundary increases. In addition, the insertion of Li pushes both sides of the phase boundary. It produces an increase in the magnitude of the hydrostatic stress at the phase boundary.

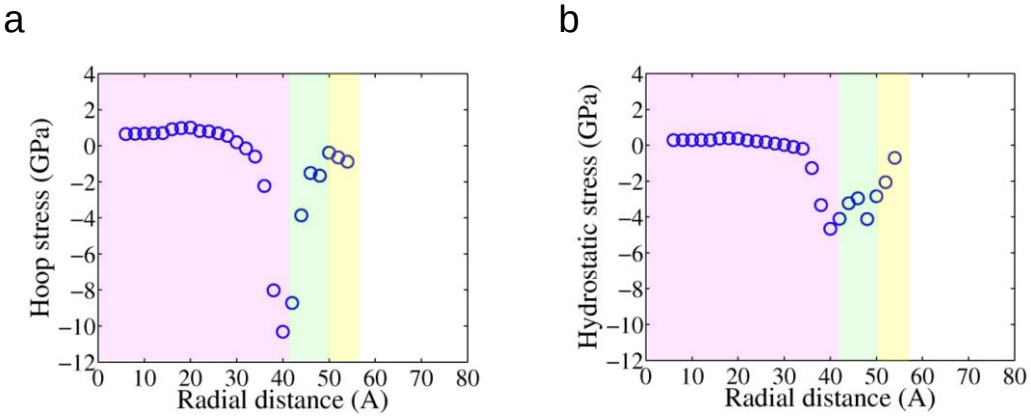

Figure 3.4 Stress distribution along the radial direction of the nanopillar at an early stage of lithiation. A core-shell structure is developed in the nanopillar. The *c*-Si core and the *a*-Li_xSi shell regions are highlighted by pink and yellow rectangles. The phase boundary is highlighted by a green rectangle. (a) Radial distribution of hoop stress. (b) Radial distribution of hydrostatic stress.

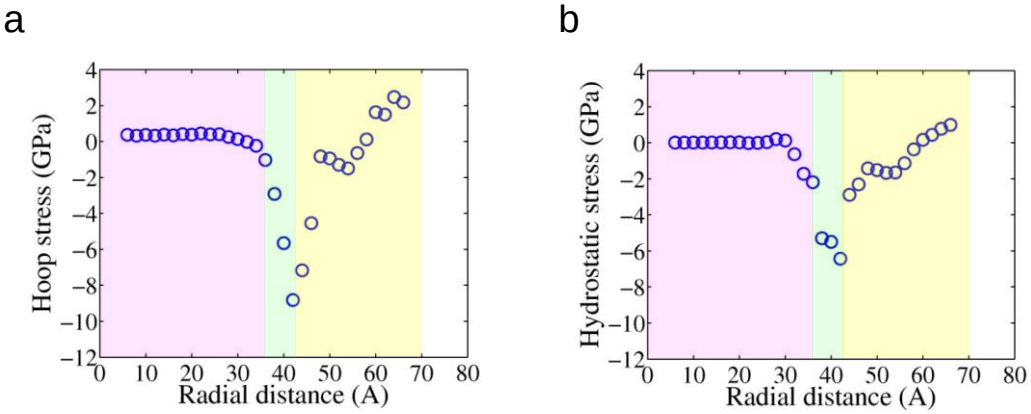

Figure 3.5 Stress distribution along the radial direction of the nanopillar at an intermediate stage of lithiation. The nanopillar exhibits a core-shell structure. The *c*-Si core and the *a*-Li_xSi shell regions are highlighted by pink and yellow rectangles. The phase boundary is highlighted by a green rectangle. (a) Radial distribution of hoop stress. (b) Radial distribution of hydrostatic stress.

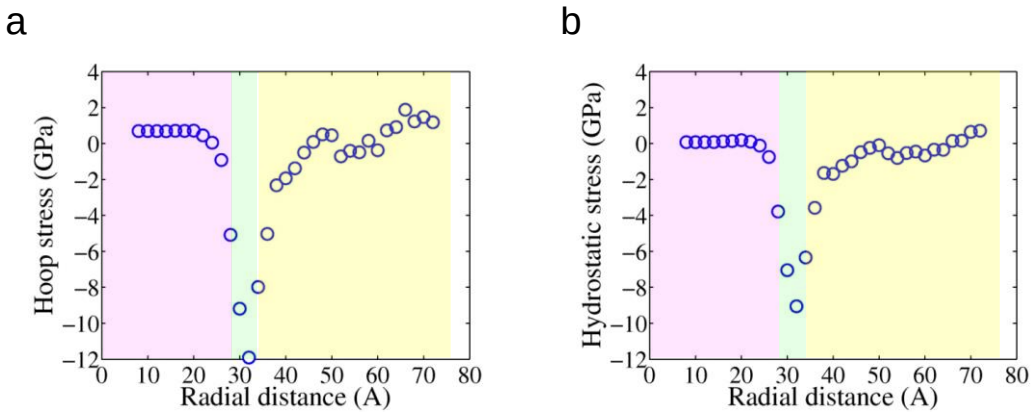

Figure 3.6 Stress distribution along the radial direction of the nanopillar at a later stage of lithiation. The nanopillar exhibits a core-shell structure. The *c*-Si core and the *a*-Li_xSi shell regions are highlighted by pink and yellow rectangles. The phase boundary is highlighted by a green rectangle. (a) Radial distribution of hoop stress. (b) Radial distribution of hydrostatic stress.

Experimental results have shown that the electrochemical lithiation of <111>-oriented *c*-Si nanopillar induces surface cracking [41]. The cracking has been attributed to the large hoop tension developed in the surface layer of the *a*-Li_xSi shell in classical continuum analyses [111, 115, 120, 121]. These works model the electrochemical reaction of Li and Si at the *c*-Si/*a*-Li_xSi phase boundary by considering the lithiation-induced deformation as a strain compatibility problem at the sharp phase boundary. The approaches to stress relaxation at the phase boundary are based on the plasticity theory. In these approaches, associated volumetric deformations under constrained conditions are accommodated by plastic flow. The findings demonstrate that the surface hoop tension is developed owing to the combined effect of plastic yielding and the "push-out" action. Our atomistic simulations directly mimic the two-phase lithiation in *c*-Si by using a Li-insertion protocol and the structural and stress relaxation. The simulations produce the

"push-out" action, and the results of stress generation indicate the development of surface hoop tension. The results of the atomistic simulations are in general consistent with those of the continuum analyses. This consistency validates the treatment of the abrupt volumetric change at the phase boundary in plasticity based approaches.

A self-limiting phenomenon in *c*-Si nanopillars and nanoparticles during the first lithiation has been revealed in recent *in-situ* TEM experiments [23, 24]. The direct time-dependent experimental measurements of the diameter of a *c*-Si core have shown that the lithiation apparently slows down as the *c*-Si/*a*-Li_xSi phase boundary moves deeply to the center of the nanopillar or nanoparticle. The kinetics of the first lithiation in *c*-Si has been studied through combined experimental and theoretical methods [23, 24, 122]. These works have suggested the rate of lithiation is controlled by atomic processes at the phase boundary and the slowing of the lithiation rate is primarily caused by stress-retardation effect. In our atomistic simulations, the magnitude of the hydrostatic compressive stress at the phase boundary increases as lithiation proceeds. Such hydrostatic compression could retard the lithiation by altering the driving force for the reaction of Li and Si and the reaction rate. In addition, our simulation results indicate a hydrostatic stress gradient in the *a*-Li_xSi shell. The internal layer of the shell undergoes hydrostatic compression. The compression could impede Li transport because it reduces the solubility of Li in *a*-Li_xSi. The Li transport could also contribute to the self-limiting lithiation.

3.1.2 Anisotropic Lithiation

Recent experiments have shown lithiation-induced swelling in a <111>-oriented *c*-Si nanopillar is highly anisotropic. The volumetric expansion along <110> direction is

much larger than that along <111> and <100> directions [25, 41]. *In-situ* TEM experiments have found that the mobility of the *c*-Si/*a*-Li_xSi phase boundary is orientation-dependent, with {110} and {112} phase boundaries migrating much faster than {111} and {100} boundaries [17, 18]. Including such orientation-dependent lithiation in the Li-insertion protocol described in Section 3.1.1, we perform atomistic simulations for a <100>-oriented *c*-Si nanopillar and investigate the effect of anisotropic lithiation on the chemo-mechanical behavior. Figure 3.7 shows the schematic illustration of the Li-insertion protocol for anisotropic lithiation in a <100>-oriented *c*-Si nanopillar. The protocol takes account of both the two-phase mechanism and the orientation-dependent phase boundary mobility. During the lithiation simulation, the {110} phase boundaries migrate inwards, leaving a square *c*-Si core.

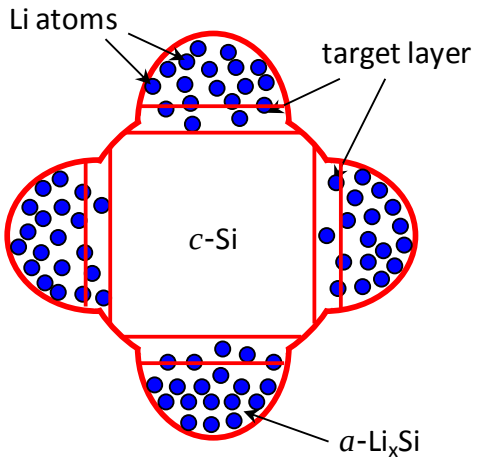

Figure 3.7 Schematic illustration of the Li-insertion protocol for a <100>-oriented *c*-Si nanopillar in the atomistic simulation. Li atoms are inserted into the *c*-Si lattice in a layer-by-layer manner, mimicking the two-phase electrochemical lithiation process with orientation-dependent mobility of the *c*-Si/*a*-Li_xSi phase boundary.

The lithiation simulation including Li insertion and relaxation processes is under the plane strain condition. The thickness of the simulation box is maintained ~2 nm. The initial radius of the <100>-oriented *c*-Si nanopillar is 45 Å. Figure 3.8 shows anisotropic lithiation-induced expansion of the nanopillar, with lateral expansion along <110> directions dominating that along <100> directions. Such morphological evolution of the cross section is due to the orientation-dependent migration of the *c*-Si/*a*-Li_xSi phase boundary during lithiation in *c*-Si.

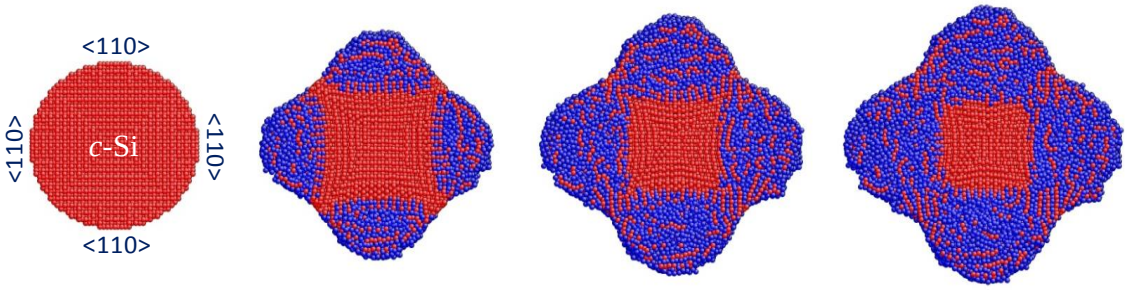

Figure 3.8 Morphological evolution of a <100>-oriented *c*-Si nanopillar in the simulation. The development of the cross section shows anisotropic swelling. Red and blue spheres represent Si and Li atoms, respectively.

Next, we examine the stress generation in the cross section of the <100>-oriented *c*-Si nanopillar. Figure 3.9 reports the hoop stress distribution developed in the nanopillar along two different paths: one is from the center of the cross section to the surface along a <110> direction (the green path in Figure 3.9), and the other is along a <111> direction (the blue path). The simulation results show that during lithiation hoop tension is developed in the surface layer of the *a*-Li_xSi shell. For each path, the trend of hoop stress distribution is similar to that for a <111>-oriented *c*-Si nanopillar discussed in Section 3.1.1. However, the surface hoop tension for the blue path is higher than that for the green orientation. In other words, the lithiation-induced hoop tension is nonuniform in the

surface layer, and higher hoop tensile stress is developed at the angular sites between two adjacent {110} facets in the cross section. Such concentration of hoop tension at the particular angular sites arises as a result of the orientation-dependent mobility of the phase boundary. At the phase boundaries, a dramatic volumetric expansion occurs owing to the electrochemical reaction of Li and Si. Such expansion pushes the lithiated product behind the phase boundaries outwards. As a result of the outward pushing normal to the {110} phase boundaries, large stretch at the intersections of the adjacent {110} facets are generated, leading to the concentration of hoop tension. This concentration of hoop tension in the surface layer of the nanopillar may cause surface cracking at the particular angular sites.

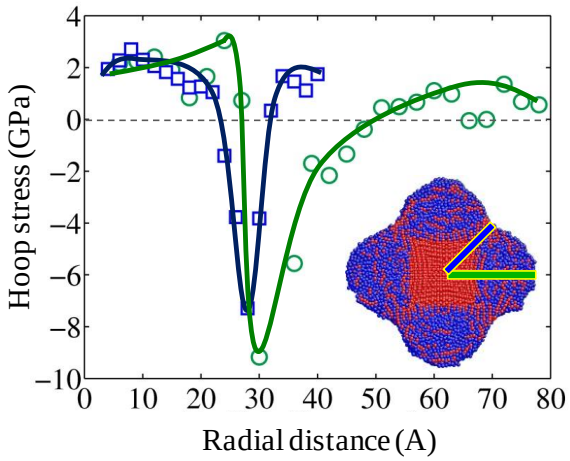

Figure 3.9 Hoop stress distribution along the radial direction in the lithiated <100>-oriented *c*-Si nanopillar. The inset figure shows two selected paths in the cross section for stress distribution profiles: green and blue. The green circles represent simulation results for hoop stress along the green path, while the blue squares represent simulation results for hoop stress along the blue path. The green and blue lines are fitting curves.

3.2 Chemo-Mechanical Behavior of *a*-Si Thin Films

Our ReaxFF-based MD simulations focus on the chemo-mechanical behavior of *a*-Li_xSi alloys under concurrent electrochemical lithiation and mechanical deformation. Currently, one effective method of measuring the mechanical properties of *a*-Li_xSi is to test the lithiation stress response of a Si thin film on an inactive substrate (e.g., a Cu underlayer on a Si wafer) [19, 32, 55]. Upon electrochemical lithiation, volume expansion in the lithiated Si thin film is constrained by the substrate, generating a biaxial compressive stress in the film, as shown in Figure 3.10. The film stress can be determined from the curvature change of substrate based on the Stoney equation. The lithiation stresses measured from such thin film experiments were often taken as the yield strengths of *a*-Li_xSi alloys in recent literature. Based on the results of these studies, we raise the following questions: Can these thin-film stresses well represent the plastic properties of *a*-Li_xSi alloys? What is the relationship between the yield strength measured from the thin-film experiment during lithiation and that from the mechanical deformation of biaxial compression, uniaxial tension and compression of *a*-Li_xSi after lithiation? Considering the limited experimental data available, in this section we address these questions with ReaxFF-based MD simulations and provide insights into the chemo-mechanical behavior of *a*-Li_xSi and the effects of loading sequence, namely concurrent and sequential electrochemical lithiation and mechanical deformation, on the mechanical properties of *a*-Li_xSi alloys.

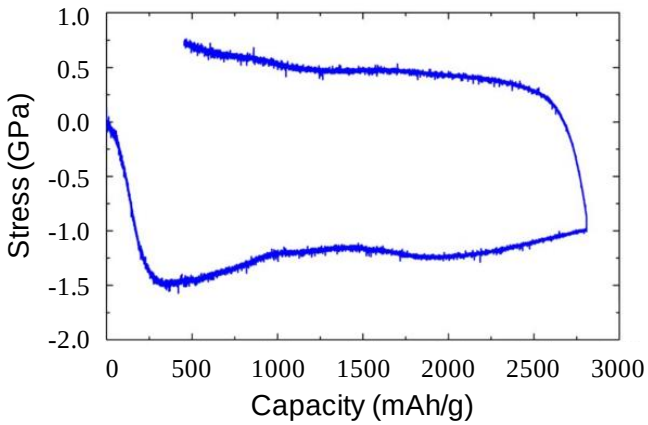

Figure 3.10 Biaxial stress generation in a Si thin film during lithiation and delithiation. Reproduced from Ref. [55].

3.2.1 Stress Generation during the Lithiation of a-Si Thin Films

We perform MD simulations to study the stress generation in an *a*-Si thin film during Li insertion after the first cycle. The atomic structure of *a*-Si is created by melting and quenching of single-crystal Si. To simulate the lithiation response, we take a supercell of *a*-Si as a representative volume element (RVE) in an *a*-Si thin film, as schematically shown in Figure 3.11. This supercell is subjected to period boundary conditions. Its size is free to change in the out-of-film direction, but fixed in the plane of the thin film, mimicking a RVE in a thin film constrained by the substrate. As the lithiation of *a*-Si occurs in a single phase mechanism [44] and the film thickness is small, we assume Li concentration in the film is uniform during the lithiation process. We randomly insert 20 Li atoms at a time and then relax the system at 300K for 10 ps. The Li concentration is approximately uniform in the system, excluding the concentration gradient-induced stress. This process of insertion and relaxation is repeated until the Li concentration reaches a desired level. The in-plane biaxial stress is calculated after each

step of Li insertion and relaxation. The MD simulations show that both the atomic structures and associated stresses are insensitive to the specific scheme of Li insertion, *i.e.*, the number of Li atoms at each insertion and frequency of insertion.

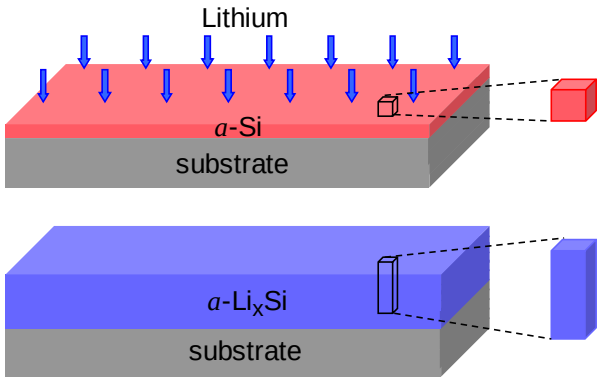

Figure 3.11 Schematic illustration of the lithiation of an *a*-Si thin film constrained by the substrate before and after lithiation. As a result of the in-plane geometrical constraint, a representative volume element in the film undergoes colossal expansion in the out-of-film direction.

During the MD simulations, the volume increase associated with Li insertion is mostly accommodated by free expansion in the out-of-film direction. Figure 3.12 shows the atomic structures of pristine *a*-Si, a partially lithiated phase of *a*-LiSi, and fully lithiated *a*-$Li_{3.75}Si$. The starting system of *a*-Si consists of 432 Si atoms, and the final one of *a*-$Li_{3.75}Si$ a total of 2052 Li and Si atoms in the supercell. The dimension of the supercell along the out-of-film direction increases dramatically, and the in-plane dimensions remain the same because of the constraint to the supercell. Figure 3.13 shows that the atomic structure characteristics of *a*-Si and *a*-$Li_{3.75}Si$ in terms of radial distribution function (RDF), angular distribution function (ADF), and ring statistics, with the dominant features consistent with previous quantum calculations [27, 30] and structural characterization results in Section 2.2. The structural characterizations indicate

that the atomic structure undergoes a transition from a random covalent network of Si-Si bonds to one similar to metallic glasses.

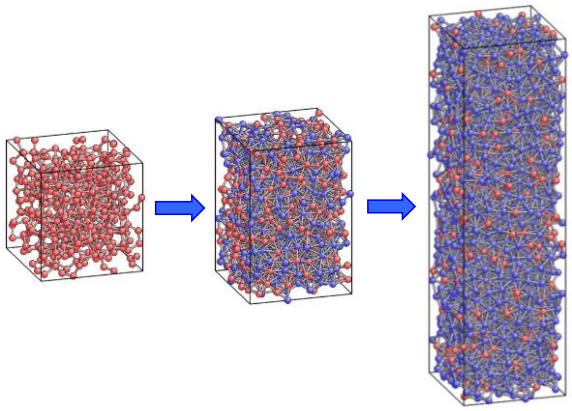

Figure 3.12 MD simulated atomic structures of pristine *a*-Si, *a*-LiSi, and *a*-$Li_{3.75}Si$, showing the colossal expansion in the out-of-film direction. Red and blue spheres represent Si and Li atoms, respectively. During Lithiation, in-plane dimensions of the system remain the same.

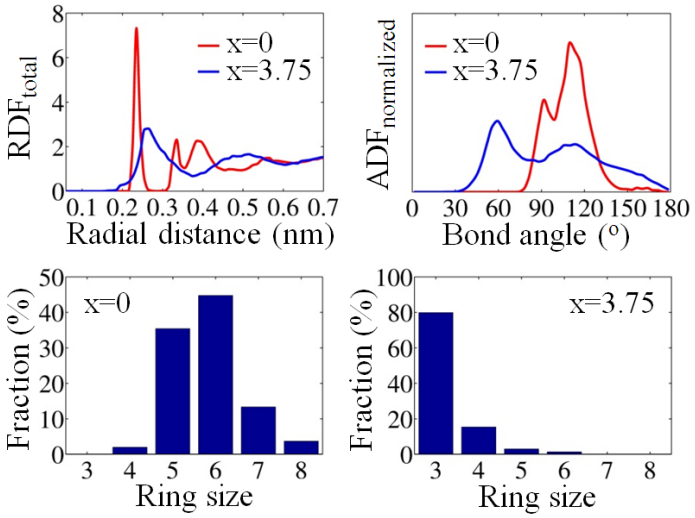

Figure 3.13 Characterization of atomic structures of a-Si and a-Li3.75Si in terms of radial distribution function (RDF), angular distribution function (ADF), and ring statistics.

Figure 3.14 shows that the *a*-Li_xSi thin film initially experiences a sharp increase in the in-plane biaxial compressive stress with increasing Li concentration (the blue squares and the blue curve). This stage of stressing is dominated by elastic compression, which arises from the geometrical constraint on the supercell that suppresses the lithiation-induced expansion in the film plane. The biaxial compression reaches a maximum of -6.5 GPa at x ~ 0.2, indicative of the onset of plastic yielding. Further lithiation causes a decrease in the magnitude of the film stress, indicating the decrease of the yield stress with increasing Li concentration. Such plastic softening can be attributed to the decreasing fraction of the strong covalent Si-Si bonds that resist against bond switching and ensuing plastic flow [51], as well as the concomitant increase of the weak metallic Li-Li bonds that facilitate plastic flow.

Overall, the trend of change of the film stress from MD is similar to that from experimental measurements. However, the magnitude of the MD-simulated compressive film stress is higher at the corresponding Li concentration. For example, the experimentally measured peak value was about -1.9 GPa at x = 0.2 [51]. This quantitative difference can be attributed to the short MD simulation time scale that limits the extent of stress relaxation. Nevertheless, MD simulations capture the dominant feature of plastic softening during lithiation.

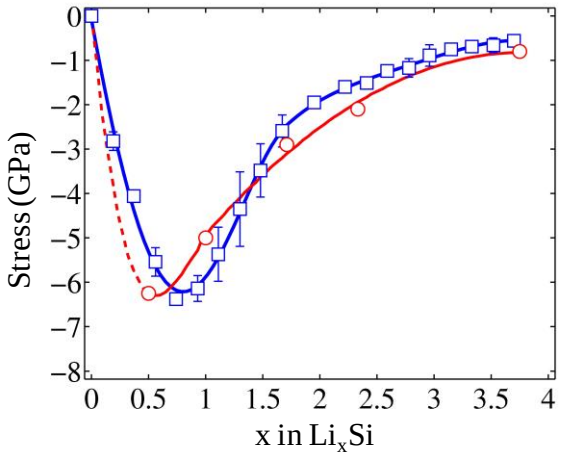

Figure 3.14 Lithiation-induced biaxial compressive stress in the film as a function of Li to Si ratio, x. Squares represent the MD results, and the blue curve is the numerical fitting. The error bars are due to the results of several configurations at a fixed Li concentration. Red circles represent the stresses calculated from an alternative loading mode, i.e., biaxial compression of an initially stress-free *a*-Li$_x$Si RVE (Section 2.4).

3.2.2 Concurrent and Sequential Loading

In this section, we discuss the effect of loading sequence on the mechanical properties of *a*-Li$_x$Si and address the questions raised in the beginning of Section 3.2. Figure 3.15 shows schematic illustrations of two different loading modes: concurrent loading, i.e., electrochemical lithiation and mechanical deformation occur concurrently (Figure 3.15 (a)), and sequential loading, i.e., electrochemical lithiation and mechanical deformation occur sequentially (Figure 3.15 (b)). We then examine the stresses obtained from both concurrent and sequential loading when the two loading modes generate same final products. In Section 2.4, σ_Y^m denotes the yield strength from the *mechanical* (*m*) deformation of biaxial compression, and σ_Y^{cm} denotes the yield strength from thin-film lithiation, which involves a concurrent *chemomechanical* (*cm*) process.

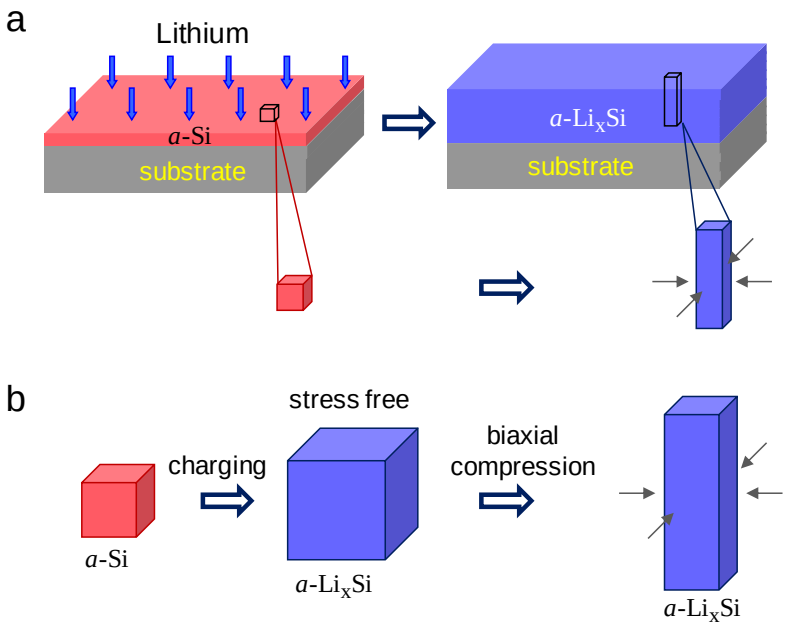

Figure 3.15 Schematic illustrations of two loading modes: (a) concurrent and (b) sequential loading. (a) Electrochemical lithiation and mechanical deformation occur concurrently. One example of concurrent loading is the lithiation of a Si thin film. (b) *a*-Si is lithiated to *a*-Li_xSi under a stress-free condition. Then, the *a*-Li_xSi is subjected to pure mechanical loading.

To compare σ_Y^m with σ_Y^{cm}, we add σ_Y^m in Figure 3.14 as a function of Li concentrations (the red circles and the solid line). It is seen that the yield strengths of σ_Y^m from biaxial compression are consistent with those of σ_Y^{cm} from thin-film lithiation, by noting that the time scales achievable in MD simulations are similar for the two cases studied. This consistency indicates that the steady state flow stress during the *mechanical* deformation of an *a*-Li_xSi alloy can be effectively taken as its yield strength, even under the *chemomechanical* loading condition.

3.3 Summary

We have studied the chemo-mechanical behavior of Si electrodes during electrochemical lithiation using atomistic simulations with a reactive force field. The atomistic simulations are able to capture the key features of the chemo-mechanical behavior, such as morphological evolution and stress generation during electrochemical lithiation. First, we have investigated the chemo-mechanical behavior of *c*-Si nanopillars by accounting for a two-phase lithiation mechanism and anisotropic lithiation. We have shown the development of tensile hoop stress at the surface of the lithiated nanopillars, which may result in fracture and cracking in the nanopillars. The hoop tension generated during lithiation is due to the combined effect of plastic flow, the two-phase mechanism, and anisotropic mobility of the *a*-Li_xSi/*c*-Si phase boundary. Second, we have investigated the chemo-mechanical behavior of an *a*-Si thin film electrode. We have shown lithiation in the thin film induces biaxial compressive stress. Initially, the magnitude of the stress increases as Li concentration in *a*-Li_xSi increases, and this behavior is dominated by elastic deformation. Then the magnitude decreases as Li concentration further increases, and this decrease in the magnitude is caused by plastic softening in *a*-Li_xSi. The findings in this work suggest that the chemo-mechanical behavior of high-capacity nanostructured electrodes must be taken into account for designing and improving the mechanical aspects of the electrodes.

4 ATOMISTICALLY-INFORMED CONTINUUM MODELING

The electrochemical lithiation of high-capacity nanostructured electrodes involves species transport, reaction at the phase boundary, phase transformation, microstructural evolution, stress generation, and cracking formation. To develop continuum models that capture essential features of the lithiation-induced fracture and failures in the electrodes, we need to understand key atomic-level processes in lithiation and incorporate controlling mechanisms. In this Chapter, we first develop continuum models to simulate the lithiation process in the nanostructured electrodes (Section 4.1). Then, we apply the models to the study of two-phase lithiation and associated stress generation in both crystalline and amorphous Si anodes (Section 4.2). The continuum modeling studies incorporate atomic-level lithiation mechanisms by tightly coupling with *in-situ* TEM experiments and atomistic simulation results. The modeling studies together with *in-situ* experiments reveal unexpected electrochemical reaction mechanisms and novel failure mechanisms in Si anodes during charge and discharge cycling.

4.1 Physical-Based Model: Diffusive Reaction and Large Deformation

The rates of charging and discharging in lithium-ion batteries (LIBs) are critically controlled by the kinetics of Li insertion and extraction in solid-state electrodes. Silicon is being intensively studied as a high-capacity anode material for LIBs. However, the kinetics of Li reaction and diffusion in Si remain unclear. Recent *in-situ* TEM experiments have provided direct measurements of the nanoscale growth kinetics in lithiated Si, by measuring the rate of growth of a surface layer of *a*-Li_xSi in *c*-Si nanowires and nanoparticles [23, 24]. The results show a self-limiting lithiation, which is

attributed to the retardation effect of the lithiation-induced stress. In Section 4.1.1, we report a theoretical study of the lithiation kinetics in individual Si nanowires. This work has implications for the design of nanostructured electrodes for achieving high capacity and rate in LIBs.

Another critical issue associated with those high-capacity electrodes is the large volume change during Li insertion and extraction, e.g., ~ 310% for Si. The resulting high stresses can cause fracture and pulverization of electrodes, thus limiting the cycle life of LIBs. To address these issues, it is essential to understand how the stress arises and evolves in lithiated materials. In Section 4.1.2, we develop a model to study the stress generation in the electrodes subjected to lithium insertion. The model accounts for both large plastic deformation and the coexistence of lithium-poor and lithium-rich phases with a sharp phase boundary. Such two-phase and inelastic deformation characteristics often arise during lithiation of crystalline particles with high capacity. Our work highlights the important effects of plastic deformation, phase boundary-mediated lithiation mechanism, finite curvature of particle geometry, and large lithiation strain at the phase boundary, which can critically control the stress generation and fracture in high-capacity electrode materials for lithium ion batteries.

4.1.1 Diffusion and Reaction

Experiments show that Li insertion into Si nanomaterials, such as nanowires and nanoparticles, occurs through the growth of *a*-Li_xSi (x ~ 3.75) [17, 18, 25, 54]. Such a Li-rich amorphous product is separated from the pristine *c*-Si by an atomically sharp phase boundary. During progressive lithiation, the Li is supplied from the

nanowire/nanoparticle surface and must diffuse across the *a*-Li_xSi layer, which grows with increasing thickness. While the lithiation processes have been studied by various experimental techniques, the kinetics of lithiation in Si nanomaterials remain unclear. From both the experimental [24, 122, 123] and modeling standpoints [121, 124-126], there is currently a strong need to quantify the lithiation kinetics in Si.

Recent *in-situ* TEM experiments have investigated the lithiation kinetics in *c*-Si nanoparticles and nanowires with different initial diameters [23, 24]. Taking advantage of the large contrast in electron transparency between crystalline and amorphous phases, real-time imaging through TEM allows a direct measurement of the growth rate of *a*-Li_xSi at the nanoscale. The measurements of the positions of the *c*-Si/*a*-Li_xSi phase boundary during lithiation have revealed the self-limiting lithiation, which is that the migration of the phase boundary slows down during the lithiation process (Figure 4.1 (a) and (b)). Such self-limiting lithiation was attributed to a stress-retardation effect. These works raise a series of fundamental questions: Is the slowing of the lithiation rate primarily caused by the stress retardation effect on Li reaction at the phase boundary or Li diffusion in the lithiated *a*-Li_xSi layer? How is the slowing of the lithiation rate affected by the curved phase boundary and the applied voltage? And what is the size effect of nanoparticles/nanowires on the lithiation rate?

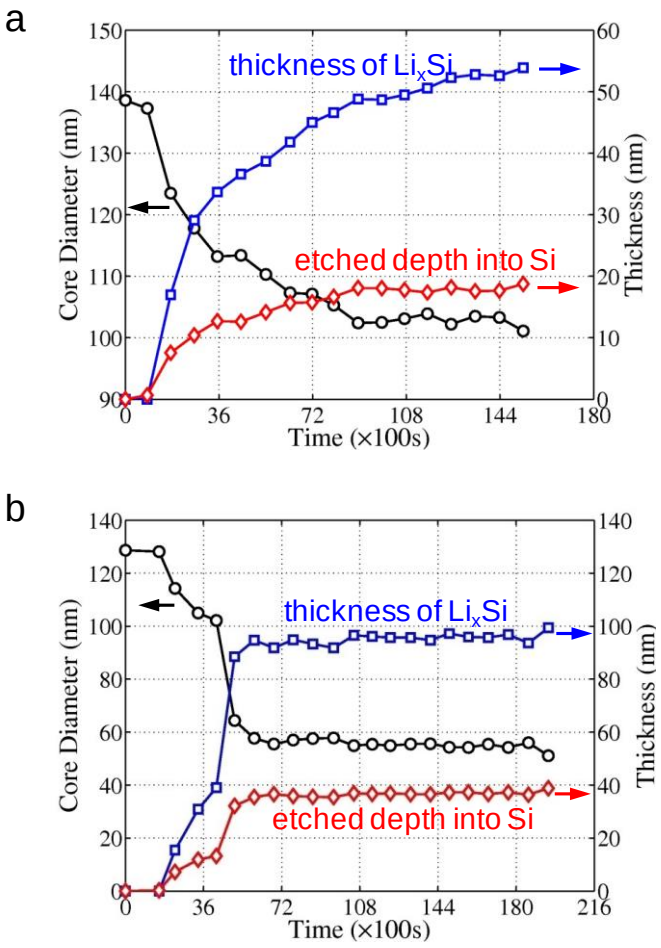

Figure 4.1 Lithiation kinetics of *c*-Si nanowires. (a) Plots of measured etch depth and diameter of a *c*-Si nanowire, SiNW_A in Ref [23], and thickness of the *a*-Li_xSi shell versus time. (b) Plots of measured etch depth and diameter of another *c*-Si nanowire, SiNW_B in Ref [23], and thickness of the *a*-Li_xSi shell versus time. The growth of *a*-Li_xSi slowed down in both nanowires during the long lithiation process. Reproduced from Ref. [23].

Focusing on the intrinsic chemical lithiation behavior of Si nanomaterials, we outline a general theory of solid-state reactions involving the moving phase boundaries [127, 128]. To highlight the essential physics, we first consider a simplified geometry where a planar film of *a*-Li_xSi (γ phase) grows between the pure phases of Li (α) and Si

(β), as shown in Figure 4.2 (a). The growth kinetics of the *a*-Li_xSi alloy layer is determined by two types of processes: (1) the *diffusion* of Li across the *a*-Li_xSi alloy layer with increasing thickness; (2) the *reaction* at the phase boundary that usually involves a reaction barrier. Figure 4.2 (b) shows that in the diffusion-controlled limit, the Li concentration at the phase boundary is given by the equilibrium values of $C_{\gamma\alpha}^{eq}$ and $C_{\gamma\beta}^{eq}$, defined in terms of the common tangent of the free energy curves, as schematically shown in Figure 4.2 (c). The corresponding rate-controlling parameter is the inter-diffusion coefficient D in the lithiated alloy. Because the mobility of Li is usually much higher than that of Si, D can be reasonably regarded as the Li diffusivity. Figure 4.2 (b) also shows that in the reaction-controlled limit, the actual concentrations at the phase boundaries are $C_{\gamma\alpha} < C_{\gamma\alpha}^{eq}$ and $C_{\gamma\beta} > C_{\gamma\beta}^{eq}$, respectively. The associated rate-controlling parameter is the interfacial reaction rate constants of $\kappa_{\gamma\alpha}$ and $\kappa_{\gamma\beta}$. Between the two limits, the rate of change of the layer thickness, $X_\gamma = X_{\beta\gamma} - X_{\alpha\gamma}$, is given by

$$\frac{dX_\gamma}{dt} = \frac{(C_{\gamma\alpha}^{eq} - C_{\gamma\beta}^{eq})\kappa_\gamma H_\gamma}{1 + \frac{\kappa_\gamma X_\gamma}{D}} \tag{4.1}$$

where the effective interfacial reaction constant κ_γ is $1/\kappa_\gamma = 1/\kappa_{\gamma\alpha} + 1/\kappa_{\gamma\beta}$ and the growth coefficient H_γ is $H_\gamma = 1/(C_{\alpha\gamma}^{eq} - C_{\gamma\alpha}) + 1/(C_{\gamma\beta} - C_{\beta\gamma}^{eq})$. Eq. (4.1) reveals the key dimensionless parameter, $\kappa_\gamma X_\gamma / D$, that governs the aforementioned reaction- and diffusion-controlled limits. Namely, when $\kappa_\gamma X_\gamma / D << 1$, the interface reaction dominantly controls the growth rate. Correspondingly, Eq. (4.1) is reduced to

$$\frac{dX_\gamma}{dt} = M^i \tag{4.2}$$

where $M^i = (C^{eq}_{\gamma\alpha} - C^{eq}_{\gamma\beta})\kappa_\gamma H_\gamma$. Integration of Eq. (4.2) gives the thickness X_γ proportional to t, called the linear growth. When $\kappa_\gamma X_\gamma / D >> 1$, this is the regime of diffusion-controlled growth. It follows that Eq. (4.1) is reduced to

$$\frac{dX_\gamma}{dt} = \frac{M^d}{X_\gamma} \tag{4.3}$$

where $M^d = D(C^{eq}_{\gamma\alpha} - C^{eq}_{\gamma\beta})H_\gamma$ and $H_\gamma = 1/(C^{eq}_{\alpha\gamma} - C^{eq}_{\gamma\alpha}) + 1/(C^{eq}_{\gamma\beta} - C^{eq}_{\beta\gamma})$. Integration of Eq. (4.3) yields the thickness X_γ proportional to $\sqrt{t}$, called the parabolic growth. It should be noted that for conceptual clarity the above variables are all defined in terms of the reference state of pure Si, as opposed to the current lithiated state. For example, the Li concentration is the number of Li per reference volume in pristine Si and X_γ is the thickness of the pristine Si layer that has been lithiated.

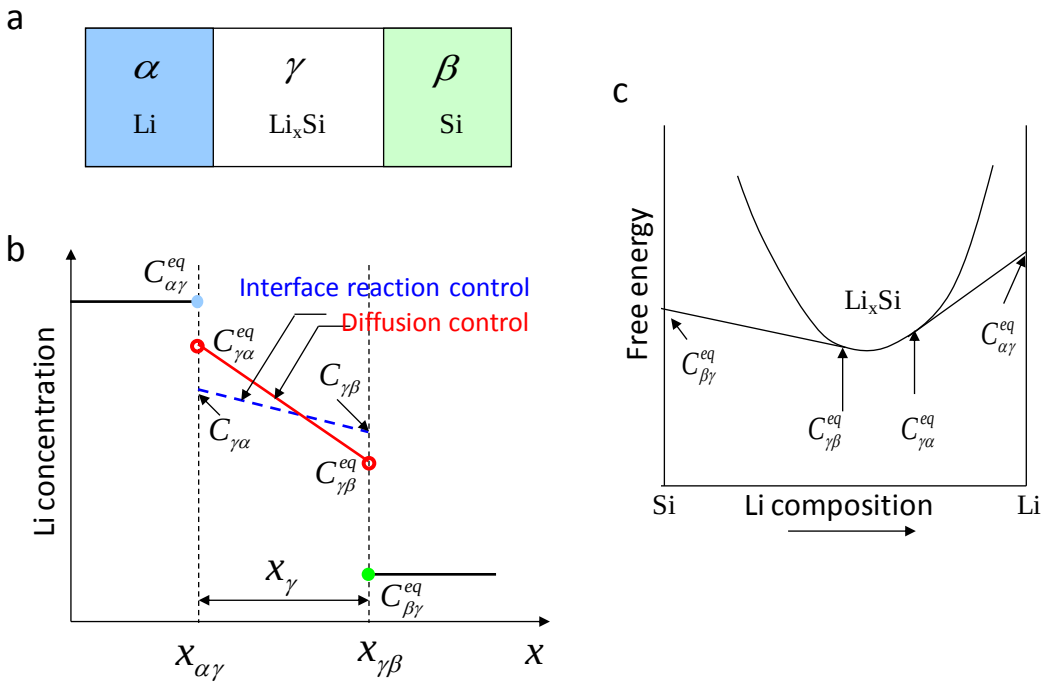

Figure 4.2 Free energy and concentration profile governing the growth of an amorphous Li_xSi layer, adapted from Gosele and Tu [127, 128]. (a) The product phase of Li_xSi (γ) grows in between the parent phases of Li (α) and Si (β).(b) Li concentration profile through the thickness of the multilayer, showing the limits of the interface reaction control and the diffusion control. The equilibrium Li concentration in α and β phase is denoted by $C_{\alpha\gamma}^{eq}$ and $C_{\beta\gamma}^{eq}$, respectively; within the layer of γ phase, the equilibrium concentrations at the $\gamma-\beta$ and $\gamma-\alpha$ interface are denoted as $C_{\gamma\alpha}^{eq}$ and $C_{\gamma\beta}^{eq}$, respectively. These concentrations can be determined by the common-tangent method in the plot of free energy as a function of Li concentration, as schematically shown in (c).

In the experiments in Ref. [23], the initial radius of a Si nanowire (SiNW), *B*, the current radius of lithiated a SiNW, *b*, and the current radius of Si core, *A*, were all directly measured. As a result, one can study the time-dependent thickness of the lithiated Si shell either in the reference state (i.e., the pristine Si shell that has been lithiated,

$X_\gamma = B - A$) or in the current state (i.e., the *a*-$Li_{3.75}Si$ shell, $x_\gamma = b - A$). Formulation in terms of the reference state is often adopted in continuum mechanics for problems with large deformation. Such an approach avoids the complication on Li flux arising from volume expansion. The following analyses will be performed on the basis of the reference state. However, given the one-to-one correspondence between X_γ and x_γ measured in experiments, the final results will be presented in terms of the current thickness, which is more intuitive.

We then apply the above theory to analyze the measured lithiation kinetics in a nanowire, SiNW_A in Ref. [23]. Recall that lithiation occurs through the core-shell mode, *i.e.*, a shell of *a*-Li_xSi grows with concomitant shrinkage of a *c*-Si core. Figure 4.3 reveals that the tapering of the Si core is negligibly small in the longitudinal direction, suggestive of considerably faster Li diffusion on the surface than in the bulk. On this basis we focus on the radial lithiation within a representative cross section of SiNW_A by taking the surface Li concentration as a boundary condition. As such, the 3D lithiation problem is reduced to 2D. Moreover, recent experiments have revealed the anisotropic swelling in *c*-Si nanowires and microslabs upon lithiation, with the largest expansion in the <110> direction [18, 25, 54]. However, for a <111>-orientated SiNW, there is a high number of (*i.e.*, six) equivalent <110> directions within the cross section, such that the isotropic lithiation in the nanowire cross section can be reasonably assumed. Hence the 2D analysis is further reduced to 1D in the radial direction. As such, the following analyses of lithiation kinetics should be considered as those related to <110> phase boundaries.

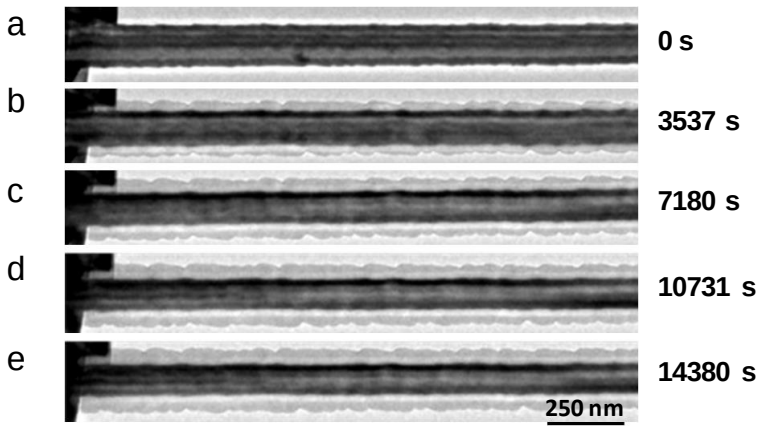

Figure 4.3 Morphological evolution of a Si nanowire, SiNW_A in Ref. [23], in 4 hours during lithiation. Reproduced from Ref. [23].

We note that the rate of growth of the *a*-Li_xSi shell (as given by the slope of the blue curve in Figure 4.1 (a)) is not constant in SiNW_A. The origin of such non-linear growth cannot be clearly determined at the moment of this study. This is because the lithiation-induced compressive stress in the *a*-Li_xSi layer could dominantly retard either the Li diffusion in the shell or the reaction of Li and Si at the core-shell interface, or the *c*-Si/*a*-Li_xSi phase boundary. To shed light on the stress-lithiation coupling, we consider both the limits of *diffusion*- and *reaction*-control, respectively.

First, we assume that the growth kinetics are controlled by Li diffusion. Taking the Li concentration at the nanowire surface C_s, as a prescribed boundary condition, we reduce the rate coefficient M^d in Eq. (4.3) to

$$M^d = D\frac{C_s - C_{\gamma\beta}^{eq}}{C_{\gamma\beta}^{eq} - C_{\beta\gamma}^{eq}} \tag{4.4}$$

Numerical integration of Eqs. (4.3) and (4.4) yields the time law of growth, *i.e.*, thickness of the lithiated layer as a function of time, when the phase boundary is planar.

To account for the self-limiting behavior of lithiation in SiNWs, we note that the *c*-Si/*a*-Li_xSi phase boundary is curved. Our analysis indicates that the self-limiting of lithiation cannot be simply explained by a geometrical curvature effect, which leads to the increased circumferential length with radial distance. This is shown in (b) by the large discrepancy between the experimental data and the modeling result (green dashed line) from direct numerical integration of Eqs. (4.3) and (4.4) with the geometrical curvature effect incorporated. Apparently, the measured data is highly nonlinear and deviates from the classic linear or parabolic relation [127-129]. We attribute the discrepancy between experiment and modeling to the stress retardation effect that will be accounted for in Eqs. (4.3) and (4.4), rather than inadequate parameter optimization.

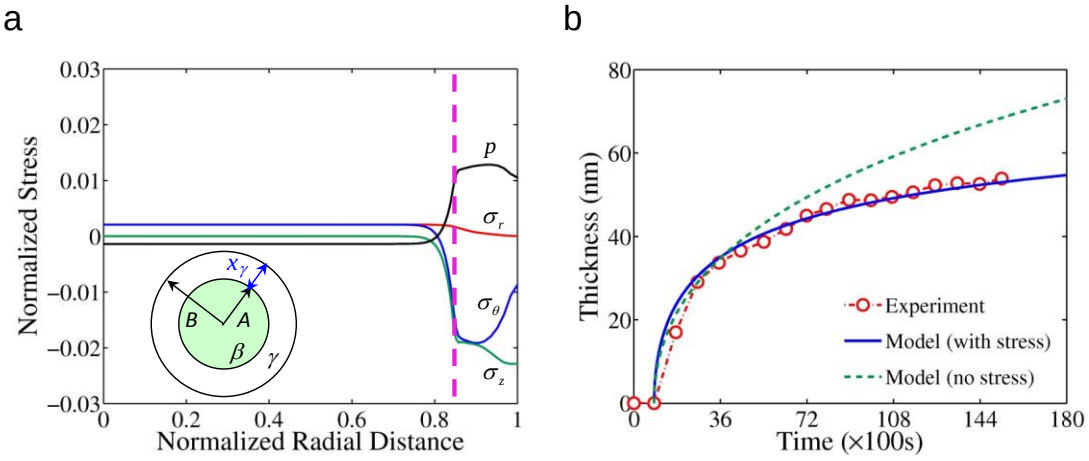

Figure 4.4 Modeling of stress generation and self-limiting lithiation in a SiNW. (a) Computed radial stress distribution at the cross section, including the radial σ_r, hoop σ_θ, axial σ_z, and hydrostatic compression $p=-(\sigma_r+\sigma_\theta+\sigma_z)/3$ components, which are normalized by Young's modulus. The radial distance is normalized by the cross-sectional radius of the SiNW. The dashed line indicates the current location of the core-shell interface. Inset shows the schematic of the cross section of a partially lithiated SiNW, where an *a*-Li_xSi shell encloses a *c*-Si core. (b) Thickness

of the *a*-Li_xSi shell versus time: comparison between experiment (circles) and modeling that includes the stress-retardation effect (blue line); also shown is the fitting curve (green dashed line) from the stress-free model where the stress-independent diffusivity is optimized to improve the overall quality of fitting.

To rationalize the slowing of the phase boundary migration, we note that large compressive stress can develop in the lithiated shell, owing to geometrical constraints from the unlithiated *c*-Si core, as shown in Figure 3.4 (b) and Figure 3.5 (b). At this moment, the stress evolution in lithiated Si cannot be quantitatively evaluated, due to a lack of experimentally measured chemo-mechanical properties of *a*-Li_xSi such as chemical strains of Li insertion and elasto-plastic properties. All of those properties depend sensitively on Li concentration and possibly on crystal orientations [20, 36]. Nevertheless, we employ a chemo-mechanical model, as described in detail in Section 4.1.2, to qualitatively capture the dominant feature of lithiation-induced stresses in SiNWs when the two-phase mechanism of lithiation is involved. In Figure 4.4 (a), we plot the representative results of lithiation-induced stresses, showing the large hydrostatic compression generated in the lithiated shell.

To evaluate the impact of the lithiation-induced compressive stress, we assume, in a first approximation, a uniform hydrostatic compression p within the lithiated shell. Then the effective diffusivity can be expressed as $D = D_0 \exp(-p\Omega / k_B T)$, where D_0 is the Li diffusivity at zero stress, Ω is the activation volume of Li diffusion, and $k_B T$ is the thermal energy. As shown in Figure 4.4 (a), the uniform pressure p represents a reasonable approximation, when the lithiated shell is thin. However, the pressure p can become highly non-uniform as the reaction front further moves to the center of the SiNW.

This has been recently shown to be caused by the increasing importance of the curvature effect of the reaction front, *i.e.*, the lithiation-induced volume expansion at the curved reaction front pushes out materials in the lithiated shell, leading to the reversal of hoop stress from the initial compression to tension in the shell. In SiNW_A, the slowing of the reaction front occurs when the lithiated shell is thin, such that the use of a uniform p is reasonably justified. Furthermore, during the early stage of lithiation, the pressure p increases as the lithiated shell thickens. This arises similarly owing to the effect of the curved reaction front, namely, the lithiation-induced pressure at the reaction front has to increase in order to push out the materials in the thickening shell. To account for the effect of increasing pressure in the lithiated shell, we rewrite the above stress-dependent Li diffusivity as

$$D = D_0 \exp[-(\alpha X_r / B)^\beta] \tag{4.5}$$

where B denotes the initial radius of the SiNW and is introduced to normalize X_r. In Eq. (4.5), α and β are the dimensionless fitting parameters. This empirical formula involves a stretched exponential function, giving the effective diffusivity that decreases with increasing shell thickness. As shown in Figure 4.4 (b), the modeling results can well match the experimentally measured values of X_r as a function of time. The fitting parameters are $\alpha = 5$ and $\beta = 2$. The effectiveness of Eq. (4.5) suggests a strong non-linear influence of lithiation-induced stresses on the lithiation kinetics, while the linear stress effect has been usually assumed in previous models of stress-diffusion coupling for Si electrodes. In addition, we obtain the fitting value of $D_0 \approx 10^{-13} \mathrm{cm}^2/\mathrm{s}$, corresponding to the Li diffusivity in *a*-$Li_{3.75}Si$ at zero stress and room temperature. We note that this

diffusivity is extracted indirectly and should be considered as an estimate. Moreover, the Si substrate also absorbs Li, thus affecting the Li concentrations at the surface of SiNW_A and accordingly the driving force of Li diffusion into the bulk of SiNW_A. These effects cannot be quantitatively evaluated at this moment. Nevertheless, our estimated diffusivity is reasonably close to the reported experimental values in the literature (in the range of 10^{-13} to $10^{-12}\mathrm{cm}^2/\mathrm{s}$), considering that various factors such as doping could change the lithiation rate.

Although the self-limiting lithiation might be caused by the stress-retarded diffusion owing to the high compressive stresses generated in the lithiated shell, the present experimental results cannot exclude the possible cause of self-limiting lithiation by the stress-retarded interface reaction. To evaluate the interface-reaction limit, we assume that the Li reaction at the nanowire surface is faster than in the bulk, and thus take the surface Li concentration of SiNW, C_s, as a prescribed boundary condition. It follows that the rate coefficient M^i in Eq. (4.2) becomes

$$M^i = \frac{C_s - C_{\gamma\beta}^{eq}}{C_s - C_{\beta\gamma}^{eq}} \kappa_{\gamma\beta} \tag{4.6}$$

where the Li concentration $C_{\gamma\beta}$ at the core-shell interface has been approximated by C_s. Similar to the above diffusion-limited case, we adopt an empirical function to represent the non-linear effect of lithiation-induced pressure at the core-shell interface, *i.e.*, $\kappa_{\gamma\beta} = \kappa_{\gamma\beta 0} \exp[-(\alpha X_r / B)^\beta]$, where $\kappa_{\gamma\beta 0}$ denotes the rate constant at the reaction front at zero stress; this relation physically reflects the fact that the pressure at the core-shell interface increases as the shell grows thicker, thus increasing the activation energy barrier

and accordingly lowering the reaction rate. Figure 4.5 shows that the modeling result well matches the experimentally measured values of X_r as a function of time. The fitting parameters are $\kappa_{\gamma\beta 0} = 5\times 10^{-10}$ m/s, $\alpha = 6$ and $\beta = 2$.

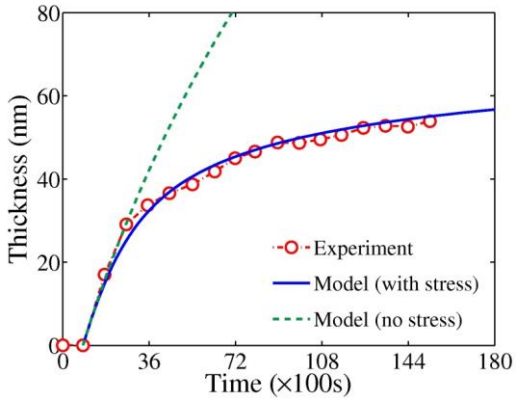

Figure 4.5 Comparison between experiment and modeling in terms of the lithiated shell thickness versus time, assuming that the self-limiting lithiation is controlled by stress-retarded interface reaction. Also shown is the modeling result without the stress effect (green line).

We note that the lithiation-induced stress generally affects both the thermodynamics (e.g., diffusion potential) and kinetics (e.g., energy barrier) of diffusion/reaction simultaneously. In the above analyses of diffusion/reaction control, we adopt the Arrhenius rate relation to account for the stress retardation effect. This approach allows us to directly fit the measured data of lithiation kinetics and also renders a strong non-linear influence of stress on lithiation. In the future, it is interesting to study the relationship between such a kinetic approach and the thermodynamic analysis in terms of the stress-retarded diffusion/reaction potential.

4.1.2 Large Deformation Elastic-Plastic Constitutive Modeling

Recent experiments indicate that plastic deformation can readily occur in the high-capacity electrode materials during lithiation [34, 55, 130]. Interestingly, *in-situ* TEM experiments have revealed that lithiation often proceeds through Li diffusion and electrochemical reactions at phase boundaries [17-19]. For example, the TEM images in Figure 4.6 show the formation of a core-shell structure in a partially lithiated Si nanoparticle, which consists of a two-phase boundary that separates an inner core of *c*-Si with an outer shell of *a*-Li_xSi ($x \sim 3.75$). The observation of such a sharp phase boundary suggests that the Li-poor and Li-rich phases do not transform continuously into each other with changing composition. Namely, there is a large solubility gap between the two phases, manifested as an abrupt change of Li concentrations across the phase boundary. Moreover, Figure 4.6 (b) reveals the formation of a surface crack, indicating the development of hoop tension in the surface layer during Li insertion. While theoretical models have been developed to analyze the Li diffusion, reaction, and associated stress states in lithiated materials [125, 131-141], the effects of large plastic deformation and two-phase microstructures on the stress generation are not yet well understood. Here, we report in this section a theoretical model that accounts for both factors.

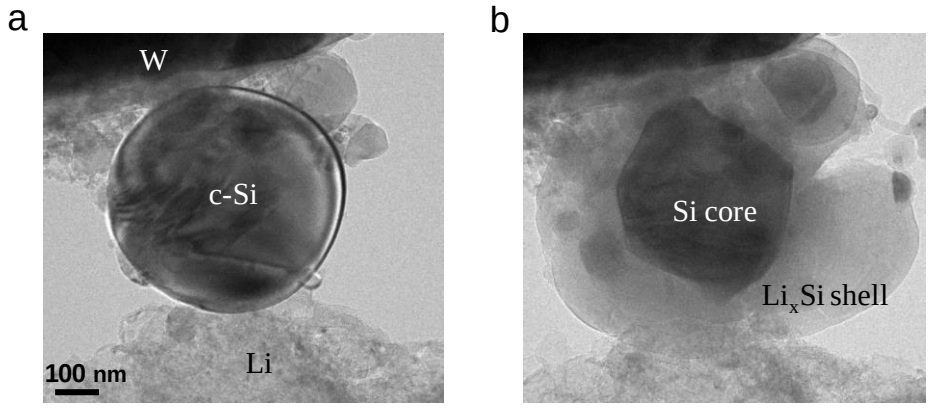

Figure 4.6 *In-situ* TEM observation of lithiation and cracking in a *c*-Si nanoparticle. (a) A *c*-Si nanoparticle is in contact with a W electrode and a Li metal counter electrode, whose surface is covered with Li_2O acting as a solid electrolyte. (b) Under an applied voltage between the two electrodes, Li quickly covers the particle surface and then flows radially into the particle, forming the structure of a pristine inner Si core (black) and an *a*-Li_xSi (x ~ 3.75) shell (grey) with a sharp phase boundary in between. The lithiation-induced swelling causes crack initiation from the particle surface. Reproduced from Ref. [17].

Nanomaterials, such as nanoparticles and nanowires, are being intensively studied as the basic building blocks of electrodes for LIBs [142]. This is motivated by the notion that the nanometer size scale can shorten the diffusion path and enable facile strain relaxation, thus enhancing both the rate capability and flaw tolerance of the nanomaterial-based electrodes [13, 105, 143]. In this section, we focus on the stress generation associated with a curved two-phase boundary, i.e., core-shell interface, which arises frequently during lithiation of nanoparticles and nanowires. It is important to note that lithiation at a moving core-shell interface affects not only the local stress states, but also the stresses in the material behind the moving boundary [17, 21, 34]. This may have a

dramatic effect on the fracture behavior of lithiated nanoparticles, e.g., leading to cracking in the outer surface during Li insertion, as shown in Figure 4.6 (b).

To focus on the essential physical effects of lithiation on stress generation, we adopt a simple elastic-plastic model to evaluate the deformation and stress states during Li insertion [138]. The total strain rate, $\dot{\varepsilon}_{ij}$, is taken to be the sum of three contributions,

$$\dot{\varepsilon}_{ij} = \dot{\varepsilon}_{ij}^{c} + \dot{\varepsilon}_{ij}^{e} + \dot{\varepsilon}_{ij}^{p} \tag{4.7}$$

where $\dot{\varepsilon}_{ij}^{c}$ is the chemical strain rate caused by lithiation and is proportional to the rate of the normalized Li concentration $\dot{c}$,

$$\dot{\varepsilon}_{ij}^{c} = \beta_{ij}\dot{c} \tag{4.8}$$

where β_{ij} is the lithiation expansion coefficient and c varies between 0 (pristine Si) and 1 (fully lithiated $Li_{3.75}Si$). In Eq. (4.7), $\dot{\varepsilon}_{ij}^{e}$ denotes the elastic strain rate and obeys Hooke's law,

$$\dot{\varepsilon}_{ij}^{e} = \frac{1}{E}\left[(1+\nu)\dot{\sigma}_{ij} - \nu\dot{\sigma}_{kk}\delta_{ij}\right] \tag{4.9}$$

where E is Young's modulus, ν is Poisson's ratio, $\delta_{ij} = 1$ when $i = j$ and $\delta_{ij} = 0$ otherwise, repeated indices mean summation. In Eq. (4.7), the plastic strain rate, $\dot{\varepsilon}_{ij}^{p}$, obeys the classic J_2-flow rule. That is, plastic yielding occurs when the effective stress, $\sigma_e = \sqrt{3\sigma'_{ij}\sigma'_{ij}/2}$, equals the yield strength σ_Y, where $\sigma'_{ij} = \sigma_{ij} - \sigma_{kk}\delta_{ij}/3$ is the deviatoric stress. The plastic strain rate is given by

$$\dot{\varepsilon}_{ij}^{p} = \dot{\lambda}\sigma'_{ij} \tag{4.10}$$

where $\dot{\lambda}$ is a scalar coefficient and can be determined by solving the boundary value problem.

We study the evolution of a two-phase core-shell particle and associated stress generation by using finite element simulations. We employ a non-linear diffusion model for simulating the two-phase core-shell structure in the finite element package ABAQUS . To capture the co-existence of Li-poor and Li-rich phases, we assume that diffusivity *D* is non-linearly dependent on the local Li concentration *c*. Note that our diffusion simulations mainly serve to generate a sequence of core-shell structures for stress analysis, rather than provide a precise description of the dynamic lithiation process, which would be difficult due to lack of experimental measurements for model calibration. To this end, we take a simple non-linear function of $D = D_0[1/(1-c) - 2\Omega c]$, where D_0 is the diffusivity constant and Ω is tuned to control the concentration profile near the reaction front. On the basis of the free energy function of a regular solution model, $f = \Omega c(1-c) + [c\ln c + (1-c)\ln(1-c)]$, the above formula of diffusivity *D* is derived according to a definition that can sharply increase the diffusion rate at high Li concentrations, $D = -D_0 c d^2 f / dc^2$. In diffusion simulations, the normalized Li concentrations behind the reaction front can quickly attain the high values (slightly below 1), while those ahead of the front remain nearly zero. This produces a sharp reaction front that is consistent with experimental observation, thereby providing a basis of further stress analysis. It should be noted that a small gradient of lithium concentration still exists behind the reaction front, so that Li can continuously diffuse through the lithiated shell,

so as to advance the reaction front toward the particle center. Finally, we emphasize that the above non-linear diffusivity function is entirely empirical, and taken as a numerical convenience for generating a sharp phase boundary for stress analyses. In the future study, a mechanistically based model is needed to characterize both the phase boundary migration and Li diffusion in each phase.

We have numerically implemented both the above diffusion model and the elastic-plastic model in this section in ABAQUS. The Li and stress-strain fields are solved with an implicit, coupled temperature-displacement procedure in ABAQUS/Standard. That is, the normalized concentration is surrogated by temperature and the lithiation expansion coefficient β_{ij} is equivalently treated as the thermal expansion coefficient. The user material subroutine for heat transfer (UMATHT) is programmed to interface with ABAQUS to update diffusivities based on the current Li concentration (*i.e.*, temperature). The Li distribution and accordingly elastic-plastic deformation are updated incrementally. In finite element simulations, we take $\Omega = 1.95$ and assign a constant Li concentration $c = 1$ at the surface; the alternative flux boundary condition gives similar results of stress generation. For numerical stability, the maximum of D is capped at $10^4 D_0$. The axis-symmetric condition is used to reduce the computational cost in ABAQUS.

We choose the material properties that are representative of high-capacity electrode materials such as Si: yield stress $\sigma_Y = 0.05E$ and Poisson's ratio $v = 0.3$. It is important to emphasize that a physically-based assignment of lithiation strains is not yet possible due to the lack of experimental measurement. Assuming the lithiation strains are

dilational, we take the lithiation expansion coefficients $\beta_r = \beta_\theta = \beta_\varphi = 0.26$, yielding a volume increase by ~ 100%. Effects of lithiation strains on the stress generation will be further studied later by examining a limiting case of uniaxial lithiation strain in the radial direction. In addition, we take the rate sensitivity exponent $m = 0.01$ to approximate the rate-independent limit, and the effective strain rate constant $\dot{\bar{\varepsilon}}_0^p = 0.001$.

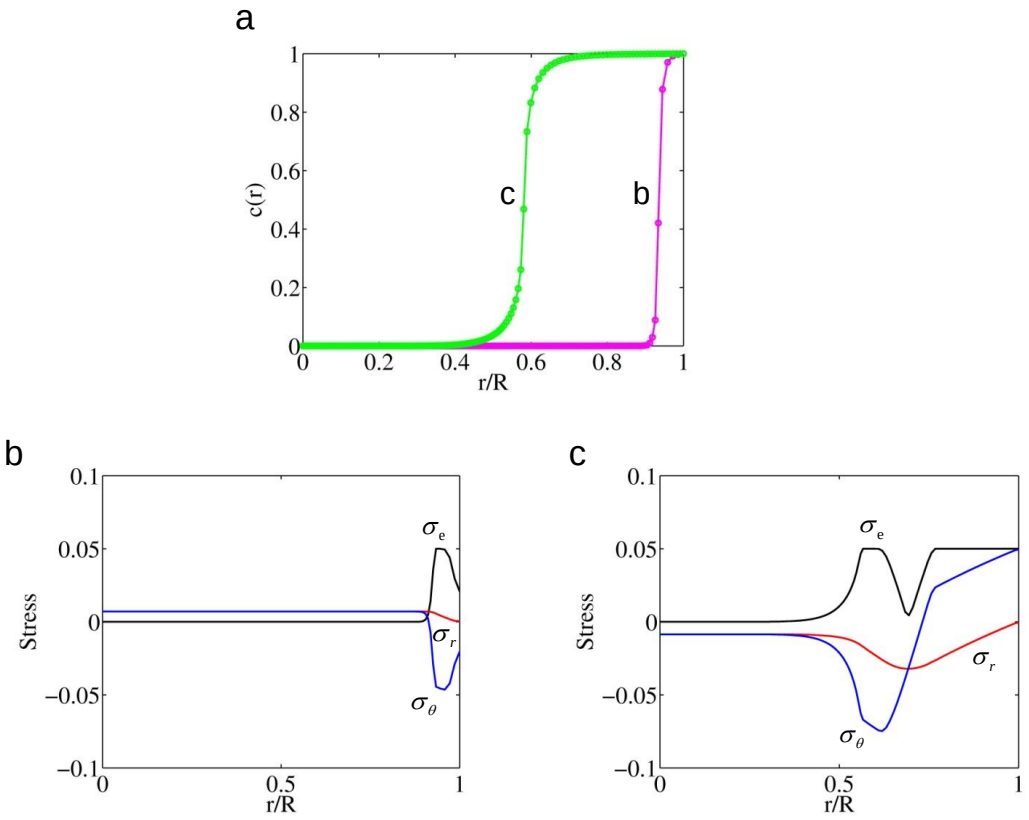

Figure 4.7 Numerical results of a two-phase particle with dilational lithiation strain from finite element modeling. (a) Radial distributions of normalized Li concentration *c*. (b-c) Radial distributions of the von Mises effective stress σ_e, radial stress σ_r, and hoop stress $\sigma_\theta = \sigma_\varphi$ (normalized by Young's modulus *E*)

Figure 4.7 (b) and (c) show the simulated results of radial stress distributions that correspond to the Li profiles in Figure 4.7 (a). The most salient feature is the

development of the tensile hoop stresses in the surface layer in the late stage of lithiation, Figure 4.7 (c), and such hoop tension reverses the initial compression, Figure 4.7 (b). Correspondingly, the core is first subjected to hydrostatic tension and later changed to hydrostatic compression. This change results from the buildup of hoop tension in the surface layer, as well as the requirement that the integrated hoop stresses over any cross section must be zero in a free-standing particle.

Previous studies of oxidation-induced stresses have indicated that correct assignment of the oxidation strain is important to understanding the stress generation [118, 144]. It has been noted that the assumed dilational oxidation strain would cause a large strain mismatch between the oxidized and un-oxidized materials at a sharp phase boundary, where the oxygen concentration changes abruptly. To reduce the mismatch strain and associated strain energy, the reactive layer model [144] has been proposed, where the oxidation-induced swelling can become uniaxial along the normal direction of the phase boundary. It has been suggested that during Si oxidation, the reactive layer can be as thin as a few atomic layers, and the oxidation occurs through a series of bond reconstructions within the layer. From the standpoint of continuum mechanics modeling, such an interfacial process can be effectively represented by assigning a uniaxial oxidation strain to the material swept by the moving reactive layer. In other words, the oxidation-induced swelling in a particle can be assumed to occur only in the radial direction, normal to the core-shell interface, and further straining of the material behind the moving phase boundary is mainly caused by the push-out effect, as discussed earlier.

Motivated by the above analysis of the oxidation strains, we study the effect of radial lithiation strain on stress generation in a two-phase particle, while the exact atomic

processes of strain transformation at the phase boundary are not yet clear. In order to compare with the results obtained from the assumed dilational lithiation strain in Figure 4.7, we take the same volume increase by ~ 100%, i.e., the lithiation expansion coefficients $\beta_r = 1$, and $\beta_\theta = \beta_\varphi = 0$. Figure 4.8 (a) and (b) show the calculated stress distributions that correspond to the two Li profiles in Figure 4.7 (a), respectively. In both plots, one can identify the approximate location of the phase boundary where the hoop stress begins to deviate from a constant value in the core.

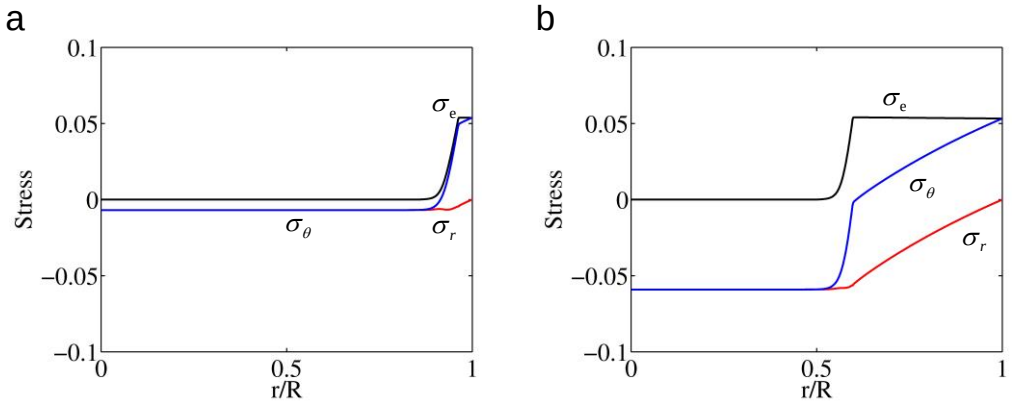

Figure 4.8 Effects of the uniaxial lithiation strain on stress generation in a two-phase particle with the same radial distributions of Li as Figure 4.7 (a). (a) Same as Figure 4.7 (b) except that the lithiation strain is uniaxial. (b) Same as Figure 4.7 (c) except the lithiation strain is uniaxial.

Comparing Figure 4.8 with Figure 4.7, we notice the following similarities and differences in stress states between the cases of dilational versus radial lithiation strains in a two-phase particle. As lithiation proceeds, the lithiated shell can readily achieve plastic yielding in both cases, underscoring the importance of plasticity in stress generation in the high-capacity electrode undergoing large lithiation-induced swelling. However, in the case of *radial lithiation strain*, Figure 4.8 shows that the pristine core is

subjected to hydrostatic compression. Within the lithiated shell, the hoop stress is compressive near the phase boundary, but it increases sharply and continuously, such that the tensile plastic yielding is achieved within a small radial distance, and the hoop tension further increases all the way to the particle surface. In contrast, in the case of *dilational lithiation strain*, Figure 4.7 shows that the core is first subjected to hydrostatic tension, and later changed to hydrostatic compression as lithiation proceeds. Within the lithiated shell, near the phase boundary the hoop stress decreases sharply and almost discontinuously, such that the hoop stress becomes compressive and plastic yielding is achieved. This hoop compression is reversed to tension at the larger radial distance due to the push-out effect, as discussed earlier.

The above results, regarding both the stress states in the core and near the phase boundary for the early stage of lithiation, agree qualitatively with those from an elastic model of oxidation-induced stresses [118], for both cases of radial and dilational lithiation strains. Hsueh and Evans have clearly explained why the core is subjected to hydrostatic compression in the case of radial oxidation strain, while the hydrostatic tension develops in the core in the case of dilational oxidation strain. Since a similar stress development is predicted in the early stage of lithiation, it is instructive to briefly review their explanations here. The key to understanding the stress buildup in the core is to first consider the deformation of the oxide (i.e., equivalent to the lithiated shell) in its "unconstrained" state, i.e., the oxide shell is assumed to detach from the core. In the case of dilational oxidation strain, the tangential component of the oxidation strain induces an unconstrained outward radial displacement, and the hydrostatic tension in the core results from the positive traction imposed to achieve displacement continuity at the core-shell

interface. In contrast, the radial oxidation strain would induce the mixed tangential tension and compression in the unconstrained state of oxide. The hydrostatic compression in the core results from the negative traction imposed to achieve displacement continuity at the core-shell interface. Here it should be noted that while the analysis by Hsueh and Evans provides a direct physical appreciation of the stress states under different assumptions of oxidation strains, their work is only limited to *elastic* deformation. In contrast, the present model accounts for the *plastic* deformation that can readily develop during the lithiation of candidate high-capacity anode materials (Si, Ge, SnO_2, etc.), as shown in recent experiments [21, 22, 34, 130].

Finally, we note that both dilational and radial lithiation strains represent the limiting case of coarse-graining the effective transformation strains associated with Li insertion at the atomically sharp phase boundary. The main difference in the predicted stress states between the two cases only lies in the early-stage response, as discussed above. In fact, the contrast of the stresses in the core predicted by the two cases, i.e., hydrostatic tension versus compression, suggests an experimental route of testing which assumption of lithiation strain is more appropriate, e.g., by measuring the elastic lattice strain in the core through high resolution TEM or electron diffraction experiments. Nevertheless, despite the somewhat different stress distributions between the two cases, the two-phase models can well capture the physical effect of large swelling at the phase boundary. Namely, the hoop tension develops in the surface layer due to the push-out effect, in a manner similar to inflation of a balloon causing its wall to stretch. The buildup of large hoop tension in the surface layer provides the main driving force of surface cracking, as observed in TEM experiments of Figure 4.6 (b).

In summary, we have studied the stress generation in a lithiated particle, accounting for both plastic deformation and the coexistence of Li-poor and Li-rich phases with a sharp and curved phase boundary. A key finding from this work is that the tensile hoop stress can develop in the lithiated shell even during Li insertion. This hoop tension originates from the lithiation-induced swelling at the sharp phase boundary with finite curvature, which often arises during lithiation of the crystalline material with curved geometry, such as Si nanoparticles and nanowires. The large hoop tension in the outer layer can consequently trigger the morphological instability and fracture in electrodes. Our work also reveals how the predicted stress states are affected by different assumptions of lithiation and deformation mechanisms, including the dilational versus radial lithiation strain, and the two-phase versus single-phase lithiation mechanism. Our results of lithiation-induced stresses provide a mechanics basis for further studying a wide range of lithiation-related phenomena, e.g., anisotropic swelling in Si nanowires [21], nanoporosity evolution in Germanium (Ge) nanowires [34], and size effect on fracture in Si nanoparticles [17].

4.2 Lithiation of Si-Based Electrodes

Silicon is an attractive high-capacity anode material for Li-ion batteries [2, 3, 5, 13, 45]. However, insertion of Li into Si causes large volume expansion of approximately 280% at the full capacity ($Li_{3.75}Si$) at room temperature. The issue of volume expansion is particularly significant in Si electrodes that have been often fabricated from crystalline Si (*c*-Si). This is because lithiation of *c*-Si occurs through a two-phase mechanism, *i.e.*, growth of amorphous Li_xSi (*a*-Li_xSi, $x \sim 3.75$) separated from *c*-Si by a sharp phase

boundary [17, 18, 24, 54]. A large change of Li concentration across this amorphous-crystalline interface of about 1 nm in width can cause drastically inhomogeneous volume expansion, leading to high stress, pulverization and capacity loss [6, 25, 41, 54]. In Section 4.2.1, we will show that the two-phase lithiation mechanism and orientation-dependent migration of the *c*-Si/*a*-Li_xSi phase boundary are key reasons for the mechanical degradation in *c*-Si nanostructured anodes during electrochemical lithiation.

Amorphous silicon (*a*-Si) is being intensively studied as a high-capacity anode material for next-generation lithium-ion batteries. Its lithiation has been widely thought to occur through a single-phase mechanism with gentle Li profiles, thus offering a significant potential for mitigating pulverization and capacity fade. *In-situ* transmission electron microscopy (TEM) experiments have discovered a surprising two-phase process of electrochemical lithiation in *a*-Si. The lithiation occurs by the movement of a sharp phase boundary between the *a*-Si reactant and an amorphous Li_xSi (*a*-Li_xSi, $x \sim 2.5$) product. Such a striking *amorphous-amorphous* interface exists until the remaining *a*-Si is consumed. Then a second step of lithiation sets in without a visible interface, resulting in the final product of *a*-Li_xSi ($x \sim 3.75$). In Section 4.2.2, we will show that the two-phase lithiation can be the fundamental mechanism underpinning the anomalous morphological evolution of micro-fabricated *a*-Si electrodes, *i.e.*, from a disk shape to a dome shape. Our results represent a significant step toward the understanding of the electrochemically-driven reaction and degradation in amorphous materials, which is critical to the development of micro-structurally stable electrodes for high-performance lithium-ion batteries.

4.2.1 Lithiation of Crystalline Si Electrodes

Figure 4.9 (a) shows a typical core-shell (*c*-Si core/*a*-Li_xSi shell) structure in a partially lithiated *c*-Si nanoparticle [58]. The original size of the nanoparticle is around 160nm. In the nanoparticle, the inner unlithiated core exhibits a hexagonal shape with {110} facets, which arises due to the fastest lithiation rate of the {110} faces in *c*-Si. The thickness of the lithiated shell is apparently orientation dependent, further evidencing the strong anisotropy in swelling during lithiation. Figure 4.9 (b) – (c) indicates that fracture occurs in a late stage of lithiation in the *a*-LixSi shell. In contrast with *c*-Si, *a*-Si exhibits robustness during lithiation. Recently, electrochemical lithiation experiments of *a*-Si nanoparticles with a wide range of diameters up to 870 nm and *a*-Si pillars with a few microns in diameter have been conducted [44]. For these *a*-Si nanoparticles and nanopillars, it has been generally recognized that the surface layer of the lithiated samples undergoes large hoop tensile deformation during lithiation. However, in these experiments, no cracking and fracture were observed in lithiated *a*-Si samples. This is contrast to the easy fracture induced by lithiation in large *c*-Si nanostructures, which is essentially related to the crystallographic effects on lithiation responses. The difference in the orientation dependence of lithiation between *c*-Si and *a*-Si has a significant impact on their fracture behavior. To appreciate the significance of such orientation-dependent lithiation, it is essential to understand why the large *c*-Si nanoparticles undergoing anisotropic swelling are fragile, but the *a*-Si nanoparticles undergoing isotropic swelling are not. To address this question in a clear and complete manner, it is necessary to review the key understandings of fracture in lithiated *c*-Si nanoparticles and nanopillars.

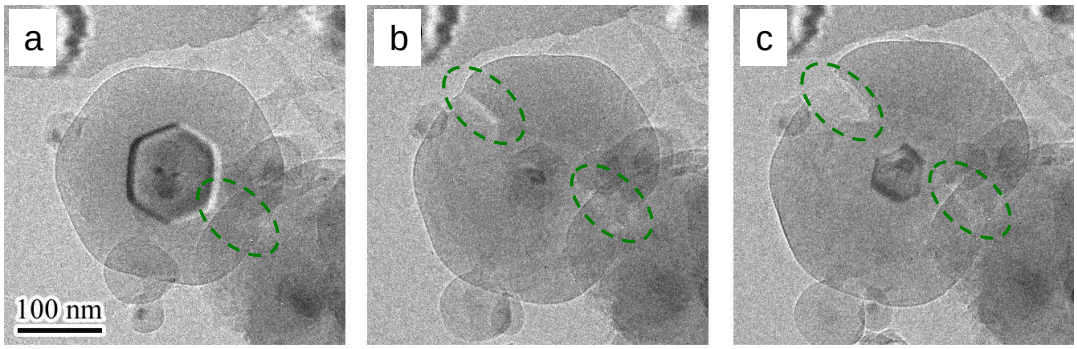

Figure 4.9 Lithiation-induced anisotropic swelling and fracture in a *c*-Si nanoparticle. The original size of the *c*-Si nanoparticle is about 160nm. (a) A partially lithiated Si nanoparticle showing the hexagon-shaped *c*-Si core with the {110} facets. (b - c) Fracture occurred in a late stage of lithiation. The well-defined fracture sites are indicated by green circles. Reproduced from Ref. [58].

First, despite compressive stress generated near the *c*-Si/*a*-Li_xSi phase boundary, large lithiation-induced expansion occurring at the *curved* phase boundary pushes out the material behind it, giving rise to a large hoop tension in the surface layer. This hoop tension drives the formation and propagation of surface cracks [17, 21]. Second, for a particle, whose size is comparable to the surface flaw size, the driving force of surface cracking, *i.e.*, energy release rate, is dependent on the particle size [17, 29]. Such a size-scaling explains the existence of a critical particle size, above which fracture occurs upon lithiation. While surface cracking and size dependence of fracture have been rationalized, the effects of anisotropic lithiation on fracture are not accounted for in the aforementioned analyses [17, 21]. Here, we show that the lithiation anisotropy is critical to the fragility of *c*-Si. In this regard, a key observation from the *in-situ* TEM experiments of lithiation in *c*-Si nanoparticles is the symmetry breaking of fracture along the circumferential direction. That is, fracture usually occurs on the well-defined angular

sites (indicated by green circles in Figure 4.9 (a-c)). These angular sites are located on the diameter planes (dashed line in Figure 4.10) that pass through the opposite vertices of the hexagon-shaped *c*-Si core. Such well-defined fracture planes have also been reported in recent experiments for *c*-Si nanopillars [41], showing the fracture sites consistent with our observations. This fracture characteristic implies the existence of intensified hoop tension in these planes, which likely originates from the anisotropic lithiation strain. Figure 4.10 provides a schematic illustration for the development of the intensified hoop tension. At each {110} facet of the *c*-Si/*a*-Li_xSi phase boundary, the anisotropic lithiation strain could be dominated by large expansion normal to the facet. Such anisotropic lithiation can result in a gap between the neighboring domains, if the domains are assumed to be lithiated independently. Then, to maintain material coherency (i.e., deformation compatibility), the large hoop tension arises near the interface plane of the neighboring domains in order to close the gap, as shown in Figure 4.10.

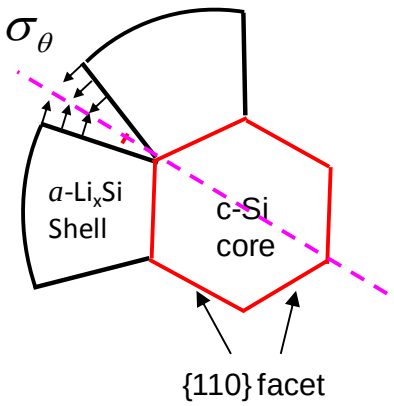

Figure 4.10 Development of an intensified hoop tension near the fracture plane (indicated by the pink dashed line). When the anisotropic expansion occurs independently on each of {110} facets, a gap will form between the neighboring domains (black blocks) in the lithiated shell. Closing the gap causes the intensified hoop tension near the neighboring domains.

To further appreciate the symmetry-breaking of the fracture in the circumferential direction as dictated by the anisotropy of lithiation strain, we invoke a recently developed continuum chemomechanical model to simulate the concurrent processes of phase transformation and stress evolution during lithiation of a nanowire. The use of the nanowire geometry simplifies the analysis, while capturing the essential physics. In the model, the total strain ε_{ij} consists of three parts, $\varepsilon_{ij} = \varepsilon_{ij}^{c} + \varepsilon_{ij}^{e} + \varepsilon_{ij}^{p}$, where the chemical strain $\varepsilon_{ij}^{c} = \beta_{ij} c$ (where c is the local Li concentration and β_{ij} is the expansion coefficient), ε_{ij}^{c} is the elastic strain, and ε_{ij}^{p} is the plastic strain. Here, the diagonal components of β_{ij} are allowed to take different values in the local coordinate system where the x_1 axis is along the <110> direction normal to the reaction front and the x_2 axis along the transverse direction of <112>. The anisotropic β_{ij} physically reflects the anisotropy of the lithiation strain that occurs at the sharp reaction front of {110} facet, and computationally mediates the anisotropy of the total strain ε_{ij}, as dictated by the requirement of deformation compatibility. In Figure 4.11, we show the simulated Li distribution c (giving the core-shell structure with {110} facets) and the associated hoop stress σ_θ under two different assumptions of chemical strain: one is isotropic (with $\beta_{11} = \beta_{22} = 0.4$) and the other is anisotropic (with $\beta_{11} = 0.7$ and $\beta_{22} = 0.2$), and both give rise to the same volume increase of ~ 100%. In the former case (Figure 4.11 (b)), the hoop tension σ_θ is almost uniform along the circumferential direction, which indicates that fracture, if occurred, would be possible at any surface location. Contrarily, non-uniform hoop tension develops in the latter case (Figure 4.11 (d)), with σ_θ intensified near the fracture planes observed in experiments.

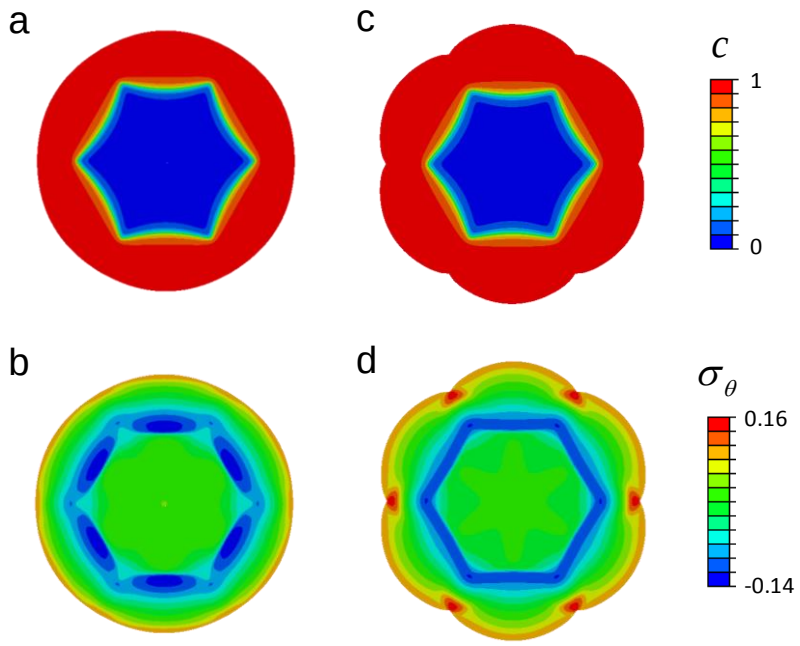

Figure 4.11 Chemomechanical modeling of the core-shell structure and stress generation in the cross section of a lithiated wire, showing the effect of the anisotropy of lithiation strain. (a - b) correspond to $\beta_{11} = \beta_{22} = 0.4$; (c - d) $\beta_{11} = 0.7$ and $\beta_{22} = 0.2$. (a - c) Li concentration normalized by the maximum of *a*-$Li_{3.75}Si$, *c*. (b - d) Hoop stress normalized by Young's modulus, σ_θ. A strong anisotropy of the lithiation strain can cause the intensified local hoop tension in the fracture plane observed in the TEM images in Figure 4.9.

The highly anisotropic lithiation strain in *c*-Si is correlated with the orientation-dependent lithiation reaction rate at the *c*-Si/*a*-Li_xSi phase boundary. While TEM experiments have shown that the lithiation of a {110} phase boundary in *c*-Si involves step-by-step ledge flow on the inclined, close-packed {111} atomic layers, it remains unclear as to what the exact local atomic arrangement of the *a*-Li_xSi product on the *c*-Si {110} phase boundary is. The atomistic origin of anisotropic lithiation strain thus warrants further study in the future.

At the continuum level, the lithiation strain should be generally larger in the normal direction than the tangential direction at the reaction front, owing to the constraint of the unlithiated core. However, considering the strong orientation-dependence of the reaction rate in *c*-Si, it is conceivable that a strong anisotropy in the lithiation strain could possibly develop at the *c*-Si/a-Li_xSi phase boundary. On the other hand, given the orientation-independence of the lithiation reaction rate in *a*-Si, the lithiation strain is expected to be more isotropic in *a*-Si than that in *c*-Si. As a result, the smaller anisotropy of the lithiation strain can effectively suppress the buildup of the high, non-uniform stress, giving rise to the tough response during the first lithiation of *a*-Si.

Discussions on anisotropic lithiation-induced strain

The present large-strain elastic-plastic modeling emphasizes that lithiation-induced anisotropic deformation is a key factor for the development of non-uniform distribution of hoop stress in *c*-Si nanopillars. In the continuum model and numerical simulations, an anisotropic expansion coefficient β_{ij} is adopted to promote the lithiation-induced anisotropic deformation. In other plasticity-based continuum models, the intrinsic lithiation-induced strain is assumed isotropic by utilizing an isotropic expansion coefficient, and such lithiation-induced deformation also results in concentration of hoop stress [111, 122, 145]. Although the isotropic expansion coefficient in these works is isotropic, the lithiation-induced large plastic strain occurring at the very sharp *c*-Si/*a*-LixSi phase boundary is highly anisotropic and tends to be normal to the phase boundary due to the constraints from the unlithiated *c*-Si core. Such anisotropic plastic strain promotes highly anisotropic deformation and induces the concentration of hoop stress. Here, we note that the exact local atomic arrangement of Li and Si atoms on the phase

boundary and the atomistic origin of the anisotropic lithiation deformation remain unclear. The atomistic processes at the phase boundary during the electrochemical reaction of Li and Si warrant further study in the future.

4.2.2 Lithiation of Amorphous Si Electrodes

To mitigate the degradation associated with the two-phase lithiation in *c*-Si, considerable efforts have been devoted to its amorphous counterpart [8, 14, 109, 142, 146-148]. Amorphous Si (*a*-Si) is intuitively thought to eliminate two-phase regions, resulting in a continuous Li reaction and homogenous volume expansion. However, whether lithiation of *a*-Si occurs by a single-phase or two-phase mechanism remains unclear [149-151]. A further interest in this question arises from the experiment reported in Ref. [147], which reveals anomalous shape changes during the electrochemical lithiation of patterned *a*-Si disk electrodes.

In situ TEM experiments of the electrochemical lithiation of *a*-Si have directly revealed a two-phase mechanism that occurs by movement of a sharp phase boundary between the *a*-Si reactant and an *a*-Li_xSi ($x \sim 2.5$) product [44]. It is unexpected to observe such an *amorphous-amorphous* interface (AAI), which has been rarely seen in the literature of solid-state phase transformations [152-154]. Unique to the lithiation of *a*-Si, there exists an abrupt change of Li concentration across the phase boundary that renders a marked contrast in electron transparency between the two coexisting amorphous phases, thereby facilitating the discovery of the AAI through *in situ* TEM. Upon the completion of two-phase lithiation, a second step of lithiation occurs in *a*-Li_xSi ($x \sim 2.5$) without a visible interface, resulting in the final product of *a*-Li_xSi ($x \sim 3.75$)

with a total volume expansion of about 280%. Nevertheless, the predominance of two-phase lithiation appears to be the key to anomalous shape growth in micro-fabricated *a*-Si electrodes, as shown by our chemo-mechanical modeling.

Figure 4.12 shows the anomalous shape changes of a patterned *a*-Si electrode during electrochemical lithiation [44, 147]. The as-fabricated electrode consisted of an array of equally-spaced circular micro-disks on a titanium (Ti) coated quartz substrate, as revealed by the scanning electron microscope (SEM) image in Figure 4.12 (a). Each disk had a thickness of 500 nm and a diameter of 5 μm and the distance between the neighboring disks was also 5 μm. Electrochemical lithiation was conducted with the patterned *a*-Si electrode, and SEM images were taken to follow the morphological evolution during various stages of lithiation (Figure 4.12 (b)-(c)). Figure 4.12 (d) shows the normalized voltage profile during the first lithiation, in which the red dots marked as "a" through "c" correspond to the SEM images shown in Figure 4.12 (a) – (c), respectively.

The growth of the *a*-Si disk electrodes upon lithiation was highly anisotropic, with the vertical expansion dominating the lateral one. The most striking shape change was the anomalous non-uniform expansion, namely, the vertical expansion of the disk electrode increased markedly with decreasing radial distance, resulting in a final dome shape at the conclusion of lithiation. From both SEM imaging and atomic force microscope (AFM) measurement, we estimate the volume expansion around 280%, confirming an approximately full lithiation to *a*-$Li_{3.75}Si$ [147]. In addition, the base of the lithiated disk electrode expanded by ~ 20% in the radial direction, which is suggestive of

the occurrence of interfacial sliding or plastic flow in the metallic substrate for accommodating the radial growth [109, 148].

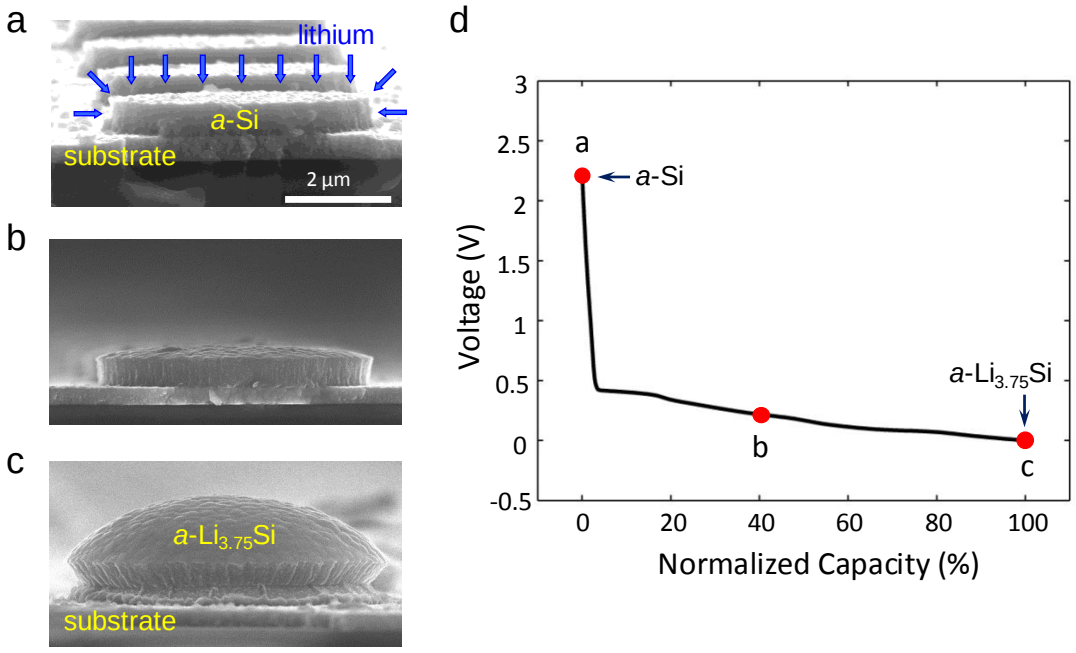

Figure 4.12 Anomalous shape growth of electrochemically lithiated *a*-Si disk electrodes. (a) SEM image of as-fabricated *a*-Si disk electrodes. (b) An intermediate state of a representative disk electrode during electrochemical lithiation. (c) A fully lithiated disk electrode exhibiting the dome-like shape. (d) Normalized voltage versus lithiation capacity. A full lithiation corresponds to the formation of *a*-$Li_{3.75}Si$. Red dots indicate the states shown in the SEM images of (a-c), respectively. Reproduced from Ref. [44, 147].

In situ electrochemical lithiation experiments inside a TEM have been conducted to directly visualize how *a*-Si was lithiated [44]. The *in situ* TEM experiments have revealed an unexpected two-phase process of electrochemical lithiation in *a*-Si. The results suggest the average value of x in the *a*-Li_xSi phase to be about 2.5. In addition, *in situ* TEM results have shown that the *a*-Si/*a*-Li_xSi two-phase boundary exists until the remaining *a*-Si is consumed. This is followed by a second step of lithiation in *a*-Li_xSi (x

~ 2.5) without a visible interface, resulting in the final product of *a*-Li_xSi (x ~ 3.75) with a total volume expansion of ~ 280%.

The disruption of a covalent Si network, either crystalline or amorphous, is generally known to be difficult. This is because of the strong covalent Si-Si bonding, *e.g.*, the energy needed to remove a Si atom from the *c*-Si surface has been measured to be a large fraction of the formation energy of a vacancy (2.4 to 3.5 eV, Ref. [129]), resulting in a low rate of Si dissociation from the Si network at room temperature. Incidentally, recent *in-situ* high resolution TEM experiment has revealed a two-phase lithiation mechanism of *c*-Si to *a*-Li_xSi through the movement of a sharp amorphous-crystalline phase boundary (Figure 4.13 (a)), facilitated by layer-by-layer ledge flow at the *c*-Si surface [17]. While the atomic structure of *a*-Si lacks the long-range order, it consists of a continuous random network of Si atoms. The local bonding environment in *a*-Si is similar to that of *c*-Si (Figure 4.13 (b) and (e)), in the sense that both *a*-Si and *c*-Si involve the strong, directional Si bonding with a small number of mis/over-coordinated defects. As a result, in both cases the local Li concentration near the phase boundary should be high in the Li-rich *a*-Li_xSi phase, so as to facilitate a process of several Li atoms enclosing a single Si or a Si-Si pair at the surface of *c*-Si or *a*-Si [99, 155], as illustrated in Figure 4.13 (c) and (f). The previous study of silicide formation indicates that a group of metallic atoms (Li in this case) can collectively weaken the Si-Si covalent bonding by electron transfer [129]. Hence, the Li "flocking" at the amorphous-amorphous phase boundary is expected to lead to easy dissociation of the Si atom from the covalently bonded *a*-Si (Figure 4.13 (f)), facilitating the lithiation process at room temperature.

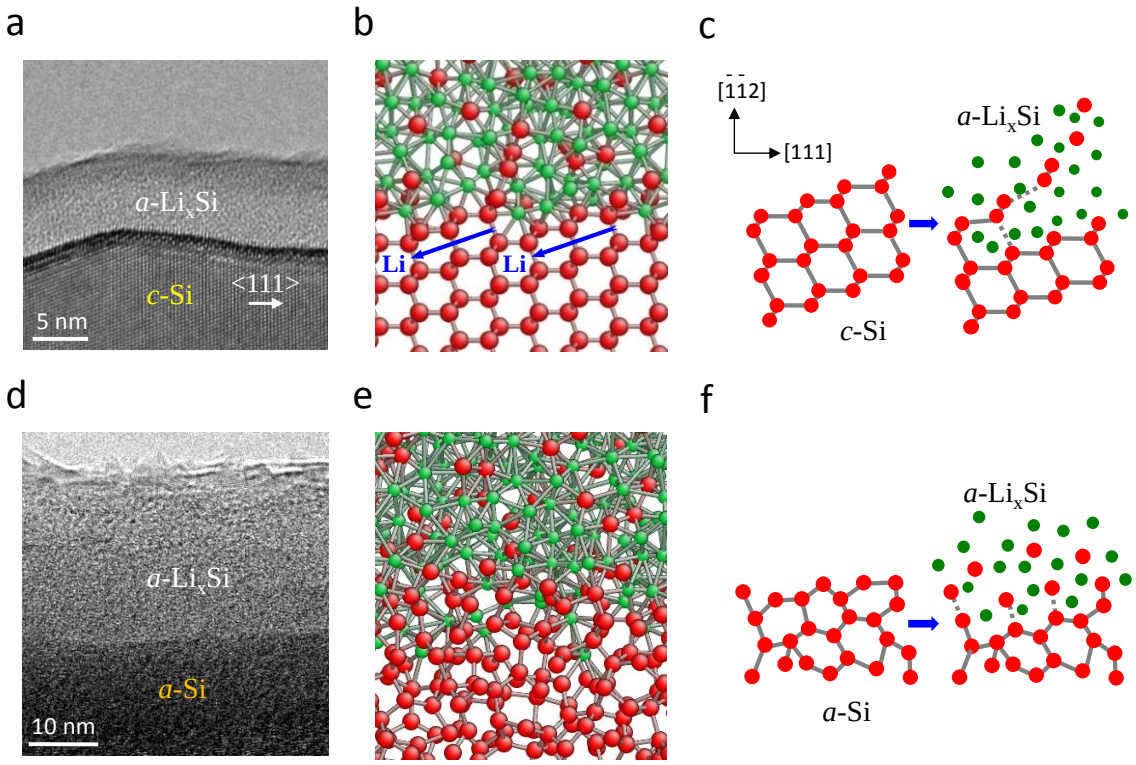

Figure 4.13 Comparison of the two-phase lithiation mechanism in *c*-Si and *a*-Si. (a) A high resolution TEM image showing a sharp phase boundary between the reactant of *c*-Si and the product of *a*-Li_xSi [18]. (b) A snapshot from molecular dynamics simulation showing the atomic structures near the amorphous-crystal phase boundary. The Li concentration is locally high near the surface of *c*-Si (red) and a group of Li atoms (green) collectively weaken the strong Si-Si covalent bonding, thereby facilitating the dissolution of Si atom from *c*-Si surface, as schematically shown in (c). (d) A high resolution TEM image showing a sharp phase boundary between *a*-Si and *a*-Li_xSi (x ~ 2.5). Reproduced from Ref. [44]. (e) A snapshot from molecular dynamics simulation showing the atomic structures near the amorphous-amorphous interface. The *a*-Si consists of a continuous random network of Si atoms. Similar to (b), the Li concentration is locally high near the surface of *a*-Si. (f) Schematics showing the proposed mechanism of dissolution of Si atoms from the *a*-Si surface into *a*-Li_xSi alloy.

We first simulate the two-phase lithiation that results in *a*-$Li_{2.5}Si$. The evolution of phase and microstructure is modeled by the non-linear diffusion of Li, as described in detail in our recent work. In finite element simulations of Li diffusion, the disk electrode is initially pristine and subjected to a constant Li flux I_0 at the surface. The normalized Li concentration behind the reaction front can quickly attain the high value (around $c = 0.67$, corresponding to *a*-$Li_{2.5}Si$), while that ahead of the front remains nearly zero. This produces a sharp reaction front, consistent with the experiment observation. To describe the lithiation-induced deformation, we adopt an elastic and perfectly plastic model. The total strain rate, $\dot{\varepsilon}_{ij}$, is a sum of three contributions, $\dot{\varepsilon}_{ij} = \dot{\varepsilon}_{ij}^{c} + \dot{\varepsilon}_{ij}^{e} + \dot{\varepsilon}_{ij}^{p}$. Here, $\dot{\varepsilon}_{ij}^{c}$ denotes the chemical strain rate caused by lithiation and is proportional to the rate of the normalized Li concentration, $\dot{c}$. That is, $\dot{\varepsilon}_{ij}^{c} = \beta_{ij}\dot{c}$, where β_{ij} is the coefficient of lithiation-induced volume expansion. We assume that the outer surface of the disk electrode is traction free, and the interface shear strength is constant between the electrode and rigid substrate. We also test the case of an elastic-perfectly plastic substrate with a perfectly bonded interface. The two interface conditions give nearly indistinguishable results of the final dome shape, though the detailed distributions of shear stresses near the interface are slightly different. The above diffusion and elastic-perfectly plastic model is numerically implemented in the finite element package ABAQUS. We also simulate the second step of single-phase lithiation that forms *a*-$Li_{3.75}Si$. In contrast to the aforementioned two-phase lithiation, we employ a constant diffusivity, giving a gentle variation of Li profiles. The axis-symmetric condition is used to reduce the computational cost. We choose the total volume increase of 280% for *a*-

$Li_{3.75}Si$; the yield stress $\sigma_Y = 0.03E$, where E is Young's modulus, and Poisson's ratio $v = 0.3$.

On the basis of the newly discovered two-phase lithiation in *a*-Si, our continuum chemo-mechanical simulation readily produced a dome shape during lithiation of the *a*-Si disk electrode shown in Figure 4.12 (c). Figure 4.14 (a) – (c) shows the snapshots of Li distributions and associated shape changes in a disk electrode undergoing two-phase lithiation. These results suggest two dominant factors that control the dome shape growth. Firstly, the sharp phase boundary between *a*-Si and *a*-Li_xSi (x ~ 2.5) is responsible for anisotropic swelling by effectively promoting the vertical expansion while suppressing the lateral expansion. This arises from the drastic change of Li concentration across the phase boundary. That is, in order to minimize the strain mismatch between the unlithiated and lithiated phases, the lithiation strain occurring at the phase boundary tends to align with the local normal direction of the phase boundary. Note that the disk electrode in the experiment features a large aspect ratio between diameter and height, so that the majority of the phase boundary is parallel to the substrate, as shown in Figure 4.14 (b). As a result, the lithiation-induced expansion occurs dominantly in the vertical direction. In addition, assuming a finite shear strength against interfacial sliding between the disk electrode and substrate [109, 148], our simulations capture the radial expansion of about 20%, as measured from the experiment.

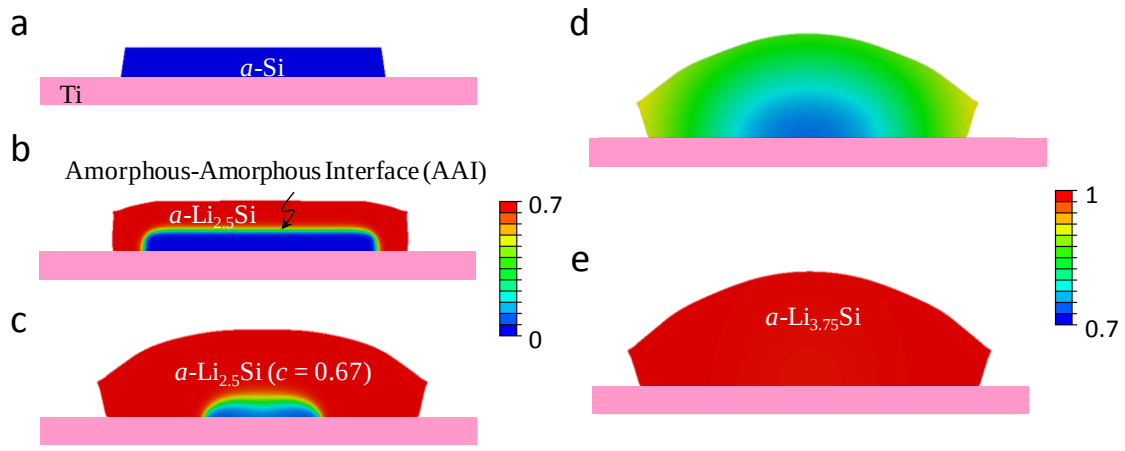

Figure 4.14 Chemo-mechanical simulation of morphological evolution in an *a*-Si disk electrode during lithiation. (a-c) The first step of two-phase lithiation to form *a*-$Li_{2.5}Si$, showing both the Li profile and shape growth: (a) a pristine *a*-Si electrode on a Ti substrate; (b) an intermediate state, showing the simulated amorphous-amorphous interface (AAI); and (c) a state close to the final *a*-$Li_{2.5}Si$. A drastic change of Li concentration occurs across the sharp AAI between *a*-Si and *a*-$Li_{2.5}Si$. Note that the remaining pristine *a*-Si undergoes a marked shrinkage in the radial direction. Contour indicates the normalized Li concentration of *c*; *a*-Si and *a*-$Li_{2.5}Si$ correspond to $c = 0$ and 0.67, respectively. (d-e) The second step of single-phase lithiation to form *a*-$Li_{3.75}Si$: (d) an intermediate state, showing the smooth and gentle Li distribution; and (e) the final state of *a*-$Li_{3.75}Si$. To display the gradual change of Li concentrations in (d-e), a color map different from (a-c) is used, with *a*-$Li_{3.75}Si$ corresponding to $c = 1$.

Secondly, the decreasing diameter of the unlithiated *a*-Si disk dictates the dome shape growth. Figure 4.14 (a) – (c) show that as lithiation proceeds, the diameter of the unlithiated *a*-Si disk decreases, due to simultaneous in-flow of Li from both the top and side surfaces. This leads to a progressive decrease of the area of the phase boundary that is parallel to the substrate. The vertical expansion occurs mostly at this part of phase boundary with reducing area, and thus gradually focuses onto the center of the disk

electrode. As a result, the dome shape develops, featuring a markedly increased vertical expansion with decreasing radial distance to the disk center. It should be noted that the second step of lithiation, either by a single-phase or two-phase reaction, will not qualitatively change the final result of formation of a dome shape in the lithiated disk electrode. For example, we simulated the second step of lithiation from *a*-$Li_{2.5}Si$ to *a*-$Li_{3.75}Si$ by assuming a single-phase reaction with gentle Li profiles. As shown in Figure 4.14 (d) – (e), the electrode with an already dome shape further expands in a nearly self-similar manner, giving a final volume expansion of ~ 280% at the conclusion of lithiation to *a*-$Li_{3.75}Si$.

Finally, we note that while the anomalous shape growth in the micro-fabricated *a*-Si electrode is rationalized in terms of the effects of two-phase lithiation, its origin requires further study regarding the influence of the lithiation stress on Li diffusion, reaction and deformation. At this point we cannot exclude the possibility that the dome-like shape would arise from the single-phase lithiation with gentle Li profiles, owing to the volume expansion mediated by the lithiation stress. Moreover, our chemo-mechanical simulations indicate that the stress effect on shape growth should be secondary compared to the two-phase mechanism of lithiation. Figure 4.15 shows a typical simulation result of single-phase lithiation.

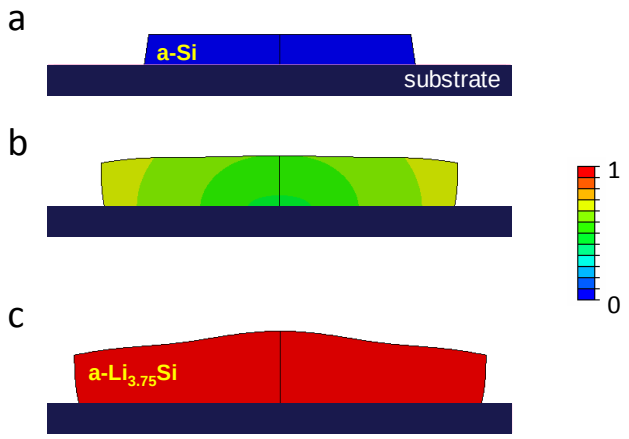

Figure 4.15 Chemo-mechanical simulation of morphological evolution of an *a*-Si disk electrode during lithiation, assuming the single-phase lithiation mechanism. (a-c) Snapshots showing the Li profile and shape growth. Contour indicates the normalized Li concentration, *c*: *a*-Si and *a*-$Li_{3.75}Si$ correspond to $c = 0$ and 1, respectively.

The occurrence of a sharp amorphous-amorphous interface during the electrochemical lithiation of *a*-Si is attributed to the need for a high local Li concentration at the phase boundary so as for it to break Si atoms away from the covalently bonded *a*-Si. The two-phase lithiation can cause the anomalous morphological change of micro-fabricated *a*-Si electrodes. Our work represents an important advance in the fundamental understanding of the working mechanisms of the high-capacity, amorphous electrodes in lithium-ion batteries [156, 157].

4.3 Summary

We have developed a physical-based model to simulate Li transport in the *a*-Li_xSi phase, reaction of Li and Si at the sharp phase boundary, phase transformation, microstructural evolution, stress generation, and crack formation in the electrodes. The

modeling studies are tightly coupled with the experiments that provide atomic-scale mechanisms to gain mechanistic insights into electrochemically-driven structural evolution and degradation in Si anodes. We have applied this model to the following topics:

First lithiation of c-Si

The chemo-mechanical behavior of *c*-Si nanoparticles and nanopillars during the first lithiation was studied with the model developed in Section 4.1. Through a stress analysis, we conclude that the anisotropy of the lithiation-induced deformation causes the non-uniform stress in the hoop direction in lithiated *c*-Si nanoparticles and nanopillars, leading to fracture in the well-defined planes. Our study of the anisotropic lithiation-induced deformation and fracture sheds light onto the mitigation of electrochemically-induced mechanical degradation in high-capacity electrode materials. Going beyond the *c*-Si studied herein, it can be followed that a-Si nanoparticles and nanopillars should remain relatively robust upon lithiation because of the lack of crystallography-related anisotropy in lithiation reaction. Interestingly, this prediction is consistent with a recent experimental observation [44]. Eliminating the anisotropy of the lithiation strain by amorphization thus presents a novel pathway to prevent the mechanical degradation in high-capacity electrode materials for advanced Li-ion batteries.

First lithiation of a-Si

Motivated by the anomalous morphological evolution of *a*-Si disk electrodes during electrochemical lithiation, our modeling studies elucidate the underlying mechanism responsible for the morphological evolution. We find that the newly

discovered two-phase lithiation mechanism in *a*-Si, which is in stark contrast to the widely believed single-phase mechanism in amorphous metals and alloys, causes the unexpected morphological evolution. Our work represents an important advance in the fundamental understanding of the electrochemical lithiation mechanisms in high-capacity amorphous materials in Li-ion batteries. Broadly, the demonstrated capability of predictive chemo-mechanical modeling combined with experimental characterization opens new opportunities for the study of electrochemical lithiation in amorphous materials.

5 CHEMO-MECHANICS OF MULTILAYER ELECTRODES

Nanostructured composites have great potential for applications in electrodes of rechargeable Li-ion and Na-ion batteries (NIB and KIBs) [5, 16, 61-67]. Utilizing nanostructured composites can enhance the performance of an electrode by minimizing side reactions with electrolytes, increasing electrical conductivity, as well as confining volume expansion. However, the structural complexity of composite electrodes may cause mechanical degradation of the electrodes due to compatibility issues between different materials. In this chapter, we will present modeling studies of the electrochemically-driven chemo-mechanical behavior of nanostructured composite electrodes.

In Section 5.1, we present chemo-mechanical modeling studies of hollow carbon nanofiber (CNF) anodes during sodiation. The CNFs are hollow and consist of a bilayer structure of a disordered-carbon (*d*-C) outer layer enclosing a crystalline-carbon (*c*-C) inner layer. We investigate the origin of the sodiation-induced geometrical changes of the CNFs and longitudinal cracks near the *c*-C/*d*-C interface. In Section 5.2, we present the modeling studies of lithiation process of SiO_2-coated Si nanowire anodes. We investigate this chemo-mechanical behavior of the SiO_2-coated Si nanowires using continuum modeling. The modeling results elucidate the dynamic process of lithiation-induced structural evolution, phase transformation and surface fracture of SiO_2-coated Si nanowires, which are observed in *in-situ* TEM electrochemical lithiation experiments. Our results provide mechanistic insight into the electrochemical reaction, microstructural evolution and mechanical degradation of nanostructured composite electrodes during charge/discharge cycling.

5.1 Sodiation of Bilayer Carbon Nanofibers

In-situ experiments of electrochemically-driven sodiation of CNFs have been conducted by using an all-solid nano-battery setup inside a TEM [158]. Figure 5.1 presents the microstructures of a hollow bilayer CNF before and after the beam-blank sodiation. For the pristine hollow CNF, its inner diameter is about 130 nm and wall thickness is about 63 nm (Figure 5.1 (c)). After full sodiation, the inner diameter decreases to 116 nm and the outer diameter increases to 263 nm. As a result, the total wall thickness increases to 73.5 nm, owing to sodiation-induced volume expansion. In addition, sodiation causes an increase of the thickness of the *c*-C layer from 25.5 nm to 29 nm, which corresponds to an average radial and volume strain of 13.7% and 6%, respectively. Similarly, the thickness of the *d*-C layer increases from 37.5 nm to 44.5 nm, which corresponds to an average radial and volume strain of 18.7% and 18.7%, respectively. Hence, the sodiated *d*-C exhibits about three times volume expansion of *c*-C, thus suggesting a much higher storage capacity of Na ions in *d*-C than *c*-C. Incidentally, a thin layer of Na_2O (2~3 nm thick) is observed to quickly form on the CNF surface (Figure 5.1 (d)) while the bulk sodiation is still ongoing, thus suggesting fast surface diffusion of Na on CNFs. Figure 5.1 (e) presents the line scan profiles across the CNF after sodiation, and the green arrows indicate the peak positions of Na and C intensity profiles. Na and C exhibit different spatial distributions, i.e., the Na intensity reaches a peak in the middle of the CNF wall and decreases gradually away from the peak, while the C intensity continually increases from the outer to the inner tube wall.

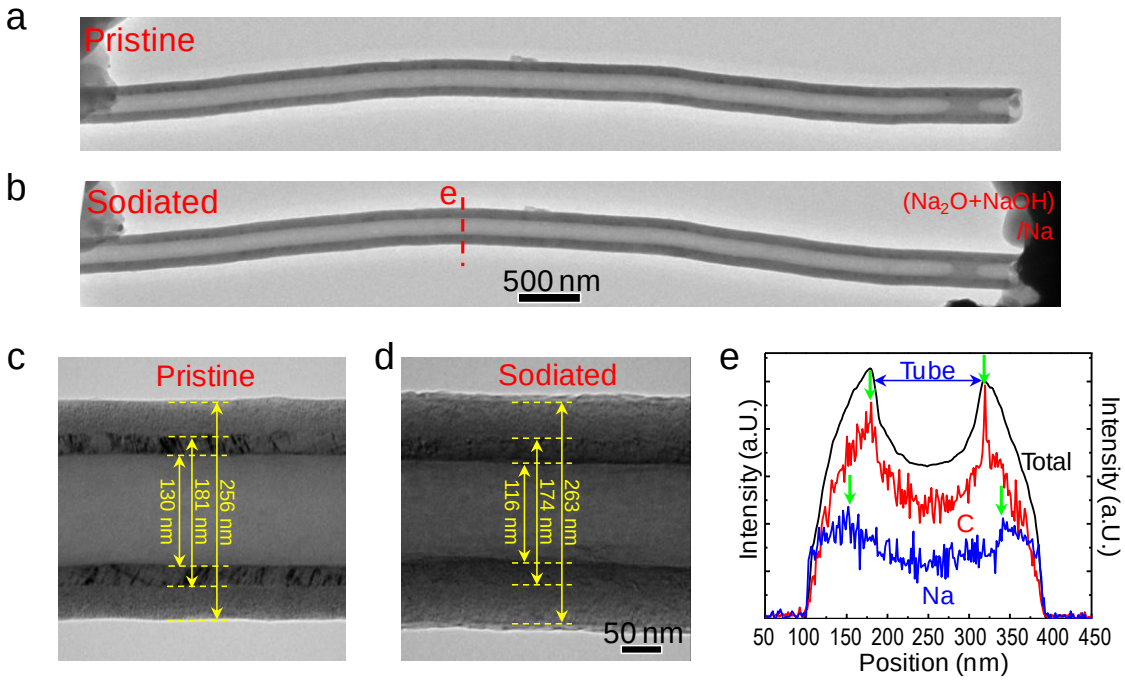

Figure 5.1 Geometry and structural changes of a bilayer CNF during sodiation under a beam-blank condition. (a, c) Pristine CNF. (b, d) Sodiated CNF. (e) The line scan profiles of C and Na across the CNF after sodiation. The green arrows point to the peak positions of Na and C intensity profiles. Reproduced from Ref. [158].

To understand the geometrical changes in CNFs, it is essential to elucidate the mechanism of strain generation and accommodation during sodiation. Particularly, one needs to explain the origin of the decreasing inner radius of the tube, as seen from Figure 5.1 (c) – (d). This result is somewhat counterintuitive, because one would expect that the sodiation-induced volume increase tends to cause an outward expansion of the tube that would result in an increase of the inner radius. To explain this unexpected result, we develop a continuum chemomechanical model to simulate the concurrent processes of Na diffusion and mechanical deformation. In the model, the strain at any material point ε_{ij} is assumed to consist of two parts, $\varepsilon_{ij} = \varepsilon_{ij}^{c} + \varepsilon_{ij}^{m}$, where ε_{ij}^{c} is the chemical strain induced

by Na insertion under a stress-free condition and ε_{ij}^{m} is the elastic strain due to chemically-induced mechanical deformation. The components of chemical strain ε_{ij}^{c} depend on the underlying atomic processes of Na insertion in *c*-C and *d*-C. A physical assignment of the appropriate values for ε_{ij}^{c} is critical to explain the sodiation-induced geometrical changes. We note that *c*-C consists of parallel graphene layers, and interlayer expansion is the primary deformation mode upon Na insertion. Hence, we assume the chemical strain ε_{ij}^{c} is highly anisotropic with only one non-zero component perpendicular to graphene layers, i.e., in the radial direction of a CNF. In contrast, *d*-C consists of patches of few-layered graphene that are approximately aligned in the radial direction of a CNF [159]. As a result, the chemical strain, ε_{ij}^{c}, in *d*-C C is similarly assumed to be highly anisotropic with only one nonzero component in the radial direction. In addition, because the longitudinal elongation of the CNFs is negligibly small in TEM experiments, the plane strain condition is assumed in the axial direction.

Finite element simulations based on the above chemomechanical model predict the geometrical changes in sodiated bilayer CNFs (Figure 5.2 (a) – (b)) that agree with experimental measurements. From the experimental data of volumetric chemical strains (being 6.0 and 18.7% in *c*-C and *d*-C layers, respectively) and considering the anisotropic nature of chemical strains as discussed above, we take $\varepsilon_r^{c,c-C} = 0.06$, $\varepsilon_\theta^{c,c-C} = \varepsilon_z^{c,c-C} = 0$ for *c*-C, and $\varepsilon_r^{c,d-C} = 0.187$, $\varepsilon_\theta^{c,d-C} = \varepsilon_z^{c,d-C} = 0$ for *d*-C. In our simplified elastic model, the radial displacement depends on Poisson's ratio (ν = 0.2), but is independent of Young's modulus. The solid line in Figure 5.2 (b) shows the predicted radial

displacement u_r as a function radial distance r. It is seen that u_r is negative in the c-C layer and so is u_r at the c-C/d-C interface. In the c-C layer, u_r becomes positive with increasing r and reaches the maximum at the outer surface of the tube. These modeling results are consistent with the experimental measurements (circles in Figure 5.2 (b)), and their numerical differences arise possibly due to a neglect of plastic strains in our model. It should be noted that previous studies have emphasized the critical role of chemical strain anisotropy in stress generation [58, 115, 118]. This work also supports the notation of anisotropic chemical strain, which results from the layered graphene lattice. At the moment of this study, the stress in the system cannot be quantitatively predicted, because the *in-situ* TEM setup is incapable of measuring the mechanical properties of nano-sized electrodes.

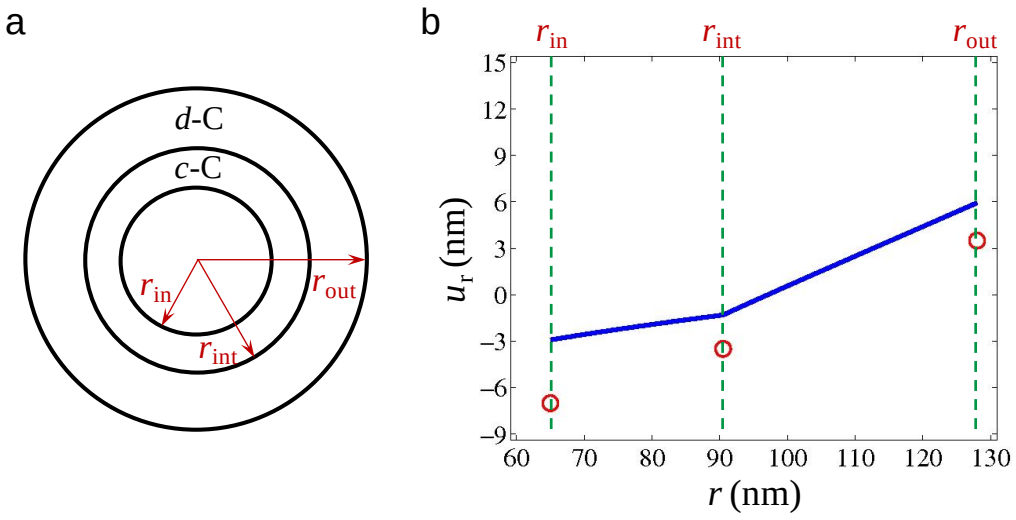

Figure 5.2 Chemo-mechanical modeling of sodiation-induced geometrical changes in a hollow bilayer CNF. (a) Schematic of cross section of the tube before sodiation, where r_{in} and r_{out} are respectively the inner and outer radius of the tube, and r_{int} is the radius of the c-C/d-C interface. (b) Predicted radial displacement u_r versus radial distance r (blue solid line), compared with experimental data (red circles).

Mechanical degradation in electrodes is usually an important cause of the irreversible capacity loss in rechargeable batteries [43]. The *in-situ* TEM study of these bilayer CNFs during sodiation has revealed mechanical degradation through formation of interface cracking [158]. Upon sodiation, a crack nucleates from the contact point between the CNF and Na_2O/Na electrolyte (Figure 5.1 (b)). As sodiation proceeds, the crack propagates from one end to the other end of the CNF along its axial direction. Such cracking behavior suggests that the unique bilayer structure, along with the hollow geometry, plays an important role in crack formation during sodiation of CNFs. Such interface cracking might be responsible for capacity fading in the initial charge/discharge cycles. Our chemo-mechanical modeling results show the development of compressive radial stress at the CNF at the *c*-C/*d*-C interface. Such compressive stress suggests that the cracking may be caused by lithiation-induced shearing between the *c*-C and *d*-C layers.

5.2 Lithiation of SiO_2-Coated Si Nanowires

In-situ lithiation experiments of SiO_2-coated <111>-oriented *c*-Si nanowires indicate that the lithiation of a SiO_2-coated Si nanowire is a complicated dynamic process (Figure 5.3). This process involves lithiation in both the Si nanowire and the SiO_2 coating layer. Upon lithiation, these two active materials, Si and SiO_2, undergo volume expansion, phase transformation, evolution of physical properties, large-strain mechanical deformation, as well as geometrical constraints from each other. Although recent research efforts have been made on SiO_2-coated Si anodes [60, 62], we note that the lithiation-induced volume expansion in SiO_2 coatings was not taken into consideration in these

works [60, 62]. However, the current *in-situ* TEM experimental results and the chemo-mechanical modeling studies show that the lithiation of SiO_2 plays an important role in the structural integrity of these coated nanowire anodes. In this section, we focus on the role of lithiation of SiO_2 coatings in this complicated dynamic process. In addition, we will discuss briefly on how the lithiation of SiO_2 affects mechanical instability in a SiO_2-coated *c*-Si nanowire.

Figure 5.3 presents the *in-situ* TEM experimental results of lithiation in a SiO_2-coated Si nanowire with a 7nm surface coating layer. The initial diameter of the pristine Si core in the nanowire is 110nm. Figure 5.3 (a) – (b) shows the morphological evolution of the nanowire during lithiation. Figure 5.3 (c) is the close-up view of the 7nm SiO2 coating (marked by red lines and arrows). Figure 5.3 (d) plots the time evolution of coating thickness during lithiation. The figure shows the coating thickness first increases until it reaches a maximum, and then gradually decreases. Such evolution of thickness can be attributed to a competition between two processes: (1) volume expansion of the coating layer induced by the lithiation of SiO_2; and (2) thinning of the coating layer due to a push-out effect of lithiated Si [17, 115]. The trend of the coating thickness can be divided into two stages. The first stage, in which the thickness increases until it reaches the maximum, is dominated by lithiation-induced volume expansion in the coating layer. The second stage, in which the thickness decreases, is due to mechanical-deformation-induced thinning. Detailed analysis of volume changes (as shown in Figure 5.4 (b)) indicates that in the first stage Si and SiO_2 are lithiated concurrently, while in the second stage the volume of the coating layer no longer changes, suggesting the coating is fully lithiated when the thickness reaches the maximum. Thus, in the second stage, the coating

undergoes purely mechanical deformation, which is caused by the push-out effect arising from the volume expansion of the Si core.

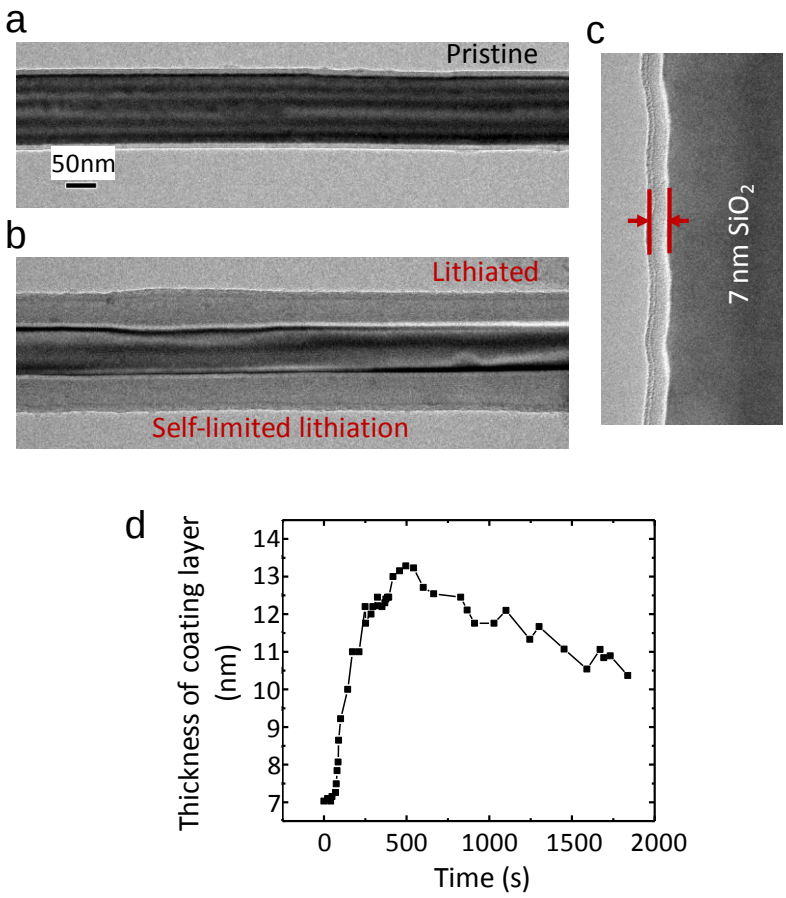

Figure 5.3 Lithiation of a SiO_2-coated Si nanowire with a 7nm-thick coating. (a) A pristine SiO_2-coated Si nanowire with a 7nm coating. (b) The nanowire is partially-lithiated because of a self-limiting effect [23]. (c) Close-up view of the coating layer (marked by red lines and arrows). (d) Plot of the coating thickness *versus* lithiation time. The coating thickness first increases until it reaches a maximum, and then gradually decreases. Such trend in thickness suggests that the lithiation of the SiO_2 coating, the lithiation of Si, and pure mechanical deformation in the coating layer occur concurrently.

We then simulate the lithiation of this SiO_2-coated Si nanowire using the chemo-mechanical model developed in Chapter 4. In the model, the strain at any material point

ε_{ij} is assumed to consist of three parts, $\varepsilon_{ij} = \varepsilon_{ij}^{c} + \varepsilon_{ij}^{e} + \varepsilon_{ij}^{p}$, where ε_{ij}^{c} is the chemical strain induced by Li insertion under a stress-free condition and ε_{ij}^{e} and ε_{ij}^{p} are the elastic and plastic strain caused by lithiation-induced mechanical deformation. Lithiation in *c*-Si and SiO_2 are assumed reaction-control and diffusion-control, respectively. Figure 5.4 (a) – (b) presents a comparison between modeling and experimental results on the geometrical evolution of the SiO_2-coated Si nanowire (Figure 5.3). The modeling results capture the concurrent lithiation processes in Si and SiO_2 in the first stage, as well as the thinning of the coating layer in the second stage. Simulation results show a tensile hoop strain of ~ 0.3 in the 7nm coating. Since there is no crack observed in the 7nm coating layer under the applied potential in the TEM experiments, this large tensile strain indicates that the fully-lithiated SiO_2 coating layer is highly ductile. Such ductile behavior can be attributed to a lithiation-induced metallic bonding environment [51]. The ductility, together with the size effect in thin coatings [17, 160], could be a reason for the absence of cracking.

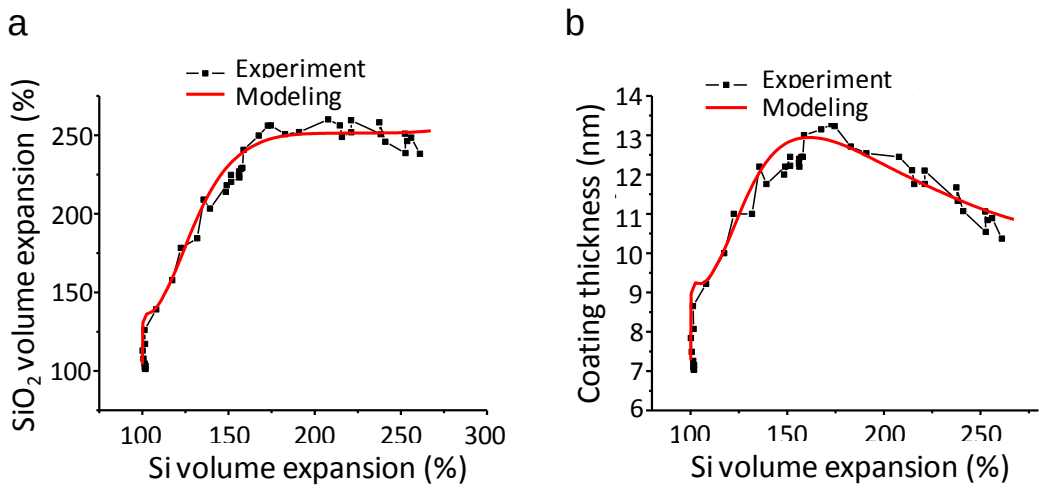

Figure 5.4 Geometrical evolution of a SiO_2-coated Si nanowire with a 7nm-thick coating. (a) SiO_2 volume expansion *versus* Si volume expansion. (b) Evolution of coating thickness *versus* Si volume expansion. (Black markers represent experimental measurements; red lines represent modeling results.)

In contrast to the nanowire with a 7nm coating, SiO_2-coated Si nanowires with a 11nm coating, in which the pristine Si core also has an initial diameter of 110nm, exhibit different lithiation phenomena. Figure 5.5 shows the geometrical evolution of a SiO_2-coated <111>-oriented *c*-Si nanowire with a 11nm coating. The geometrical evolution indicates that lithiation in the Si core stops at an earlier stage due to a stronger self-limiting effect [23], compared to that in the nanowire with a 7nm coating. In addition, the volume of the SiO_2 coating layer increases in the entire lithiation process of the nanowire. The dynamic lithiation process in the nanowire with a 11nm coating is different from that in the nanowire with a 7nm coating. Such a difference is mainly attributed to a relatively longer Li diffusion path in a 11nm coating.

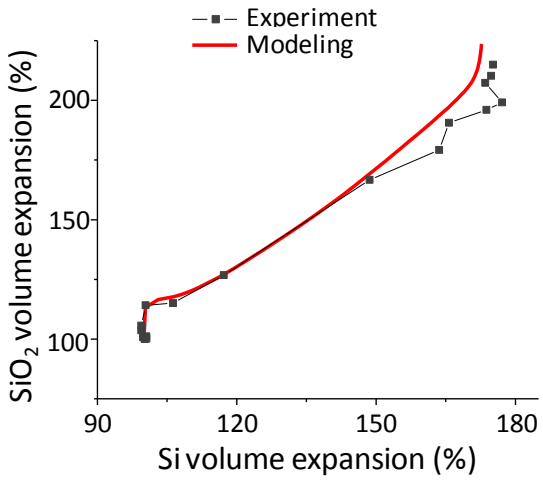

Figure 5.5 Geometrical evolution of a SiO_2-coated Si nanowire with a 11nm-thick coating. (a) SiO_2 volume expansion *versus* Si volume expansion. (Black markers represent experimental measurements; red lines represent modeling results.)

Another phenomenon in the lithiation of the nanowire with a 11nm coating, which is not observed for the nanowire with a 7nm coating, is lithiation-induced local fracture in the surface coating. The local fracture occurs at an early stage of the lithiation, indicating the 11nm coating cannot maintain structural integrity even at a relatively small tensile hoop strain. This fragility of coating at the early stage of lithiation is mainly due to the brittle nature of poorly-lithiated SiO_2. A lithiation-induced brittle-to-ductile transition in lithiated Si alloys has been reported [46, 51, 112]. The evolution of fracture properties is caused by lithiation-induced changes in atomic bonding environment, as explained in Chapter 2. This work indicates that a lithiation-induced brittle-to-ductile transition also exists in lithiated SiO_2.

5.3 Summary

We have applied the chemo-mechanical model developed in Chapter 4 to the study of electrochemical-reaction-induced structural and property evolutions in nanostructured multilayer electrodes. First, we present modeling studies of sodiation-induced structural changes in hollow bilayer CNFs. The modeling results show that the anisotropic sodiation-induced strain in *d*-C layers is a key factor for an unexpected shrinkage of the inner tube. Longitudinal cracks, which are frequently observed near the *c*-C/*d*-C interface after sodiation, are attributed to sodiation-induced shearing between *c*-C and *d*-C layers. Our modeling studies are tightly coupled with *in-situ* TEM results and provide critical insights into the degradation mechanisms of carbon-based anodes for NIBs. Second, we investigate the lithiation of SiO_2-coated Si nanowires with different coating thicknesses. Si and SiO_2 are lithiated concurrently, and the lithiation rates in these two materials are different. Thus, the lithiation of these SiO_2-coated Si nanowires is a complicated dynamic process. This dynamic process involves two competitions. One competition is between lithiation-induced volume expansion of the SiO_2 coating and thinning of the coating due to a push-out effect from lithiation in Si. The other competition is between the lithiation-induced evolution of fracture properties and mechanically-driven fracture in the surface coating. This work suggests that 7nm is an optimal coating thickness to maintain structural integrity. The results of this work provide an understanding of electrochemical lithiation in nanostructured electrodes coated with active materials.

6 CONCLUSIONS AND RECOMMENDED FUTURE RESEARCH

6.1 Significance of Contributions

This thesis presents multi-physics studies on the chemo-mechanics of high-performance battery electrode materials using both atomistic and continuum modeling. The modeling studies are integrated with *in-situ* TEM experimental characterizations. The main results and contributions are summarized below.

- *Mechanical behavior of lithiated materials*

  This work investigates the mechanical behavior of lithiated materials using an approach combining atomistic modeling, continuum modeling and experimental characterization. The results elucidate the mechanistic underpinnings for the evolution of the mechanical behavior of lithiated alloys induced by electrochemical lithiation in terms of the nature of atomic bonding. Our quantitative characterization and mechanistic understanding of the mechanical behavior of electrochemically lithiated Si alloys represent a critical step toward the rational design of durable Si-based electrodes. Broadly, our modeling approach integrated with experiments can be applied to the mechanical characterization of a wide range of electrochemically active materials for energy storage and conversion applications.

- *Chemo-mechanics of high-capacity nanostructured electrodes*

This work develops physical-based models at both the continuum and atomistic levels for simulating multiple physics processes in high-capacity electrodes during electrochemical lithiation. The modeling studies incorporate key features observed from *in-situ* TEM experiments to gain unprecedented mechanistic insights into electrochemically-driven structural evolution and damage processes in the electrodes. The studies also provide a transparent mechanics foundation for investigating lithiation-induced stress generation and failures in materials with multi-phase microstructures. The physical models developed provide a mechanics basis for further studying a wide range of lithiation-related phenomena.

The main results of this thesis have been presented in a series of publications: Ref. [23, 56, 58, 83, 115, 145, 158].

6.2 Recommended Future Research

Understanding the mechanical behavior of advanced energy-storage materials is essential to realizing their extraordinary functions in structural and device applications. However, the complexity in the mechanical behavior of the materials, especially under extreme conditions, poses significant challenges for the mechanics research. To meet these challenges, potential future research could focus on the modeling and simulation of mechanics-related phenomena in the materials by integrating solid mechanics, materials physics, and high performance computing at multiple length and time scales. The goals of the research include: (1) to understand the mechanical behavior and degradation mechanisms in advanced materials, (2) to develop innovative modeling tools for

predicting the material properties, and (3) to guide the design of new materials with tailored and unprecedented properties.

Intensive research on Li-ion electrodes is currently underway to seek new materials and architectures with outstanding performance, such as meso-scale structures, 3D architectures of nanomaterials, nanoporous materials, and heterostructured nanocomposites. These materials are promising alternatives to currently used electrodes owing to their extraordinary properties, such as facile strain relaxation, superior rate, capacity and cyclability. However, the chemo-mechanical degradation mechanisms of these new materials are largely unknown. The objective of potential future research could be to understand and predict the chemo-mechanical behavior of these battery materials using a mechanics-based approach. The overarching goal is to guide materials design of high performance energy storage systems. Future research could involve (1) investigation of the chemo-mechanical behavior of these novel materials and architectures by synergistically integrating the multi-scale/multi-physics modeling with experiments; (2) understanding of deformation, fracture and failure mechanisms in the materials during electrochemical cycling. The modeling studies will take into account the effects of characteristic structures and chemo-mechanical behavior at different length scales. The capabilities and tools developed through the above research can be broadly applied to investigate the alternatives to Li-ion batteries, including sodium-ion and lithium-sulfur batteries.

REFERENCES

1. Larcher, D., Beattie, S., Morcrette, M., Edstrom, K., Jumas, J.-C., and Tarascon, J.-M., Recent findings and prospects in the field of pure metals as negative electrodes for Li-ion batteries. Journal of Materials Chemistry, 2007. 17(36): p. 3759-3772.

2. Tarascon, J.M. and Armand, M., Issues and challenges facing rechargeable lithium batteries. Nature, 2001. 414(6861): p. 359-367.

3. Li, H., Huang, X., Chen, L., Wu, Z., and Liang, Y., A High Capacity Nano - Si Composite Anode Material for Lithium Rechargeable Batteries. Electrochemical and Solid-State Letters, 1999. 2(11): p. 547-549.

4. Goodenough, J.B. and Kim, Y., Challenges for Rechargeable Li Batteries. Chemistry of Materials, 2010. 22(3): p. 587-603.

5. Magasinski, A., Dixon, P., Hertzberg, B., Kvit, A., Ayala, J., and Yushin, G., High-performance lithium-ion anodes using a hierarchical bottom-up approach. Nature Materials, 2010. 9(4): p. 353-358.

6. Li, J., Dozier, A.K., Li, Y., Yang, F., and Cheng, Y.-T., Crack Pattern Formation in Thin Film Lithium-Ion Battery Electrodes. Journal of The Electrochemical Society, 2011. 158(6): p. A689-A694.

7. Beaulieu, L.Y., Eberman, K.W., Turner, R.L., Krause, L.J., and Dahn, J.R., Colossal Reversible Volume Changes in Lithium Alloys. Electrochemical and Solid-State Letters, 2001. 4(9): p. A137-A140.

8. Beaulieu, L.Y., Hatchard, T.D., Bonakdarpour, A., Fleischauer, M.D., and Dahn, J.R., Reaction of Li with Alloy Thin Films Studied by In Situ AFM. Journal of The Electrochemical Society, 2003. 150(11): p. A1457-A1464.

9. Wu, H., Zheng, G., Liu, N., Carney, T.J., Yang, Y., and Cui, Y., Engineering Empty Space between Si Nanoparticles for Lithium-Ion Battery Anodes. Nano Letters, 2012. 12(2): p. 904-909.

10. Wu, H., Chan, G., Choi, J.W., Ryu, I., Yao, Y., McDowell, M.T., Lee, S.W., Jackson, A., Yang, Y., Hu, L., and Cui, Y., Stable cycling of double-walled silicon nanotube battery anodes through solid-electrolyte interphase control. Nat Nano, 2012. 7(5): p. 310-315.

11. Yao, Y., McDowell, M.T., Ryu, I., Wu, H., Liu, N., Hu, L., Nix, W.D., and Cui, Y., Interconnected Silicon Hollow Nanospheres for Lithium-Ion Battery Anodes with Long Cycle Life. Nano Letters, 2011. 11(7): p. 2949-2954.

12. Hu, L., Wu, H., Gao, Y., Cao, A., Li, H., McDough, J., Xie, X., Zhou, M., and Cui, Y., Silicon–Carbon Nanotube Coaxial Sponge as Li-Ion Anodes with High Areal Capacity. Advanced Energy Materials, 2011. 1(4): p. 523-527.

13. Chan, C.K., Peng, H.L., Liu, G., McIlwrath, K., Zhang, X.F., Huggins, R.A., and Cui, Y., High-performance lithium battery anodes using silicon nanowires. Nature Nanotechnology, 2008. 3(1): p. 31-35.

14. Cui, L.-F., Ruffo, R., Chan, C.K., Peng, H., and Cui, Y., Crystalline-Amorphous Core−Shell Silicon Nanowires for High Capacity and High Current Battery Electrodes. Nano Letters, 2009. 9(1): p. 491-495.

15. Song, T., Xia, J., Lee, J.-H., Lee, D.H., Kwon, M.-S., Choi, J.-M., Wu, J., Doo, S.K., Chang, H., Park, W.I., Zang, D.S., Kim, H., Huang, Y., Hwang, K.-C., Rogers, J.A., and Paik, U., Arrays of Sealed Silicon Nanotubes As Anodes for Lithium Ion Batteries. Nano Letters, 2010. 10(5): p. 1710-1716.

16. Kovalenko, I., Zdyrko, B., Magasinski, A., Hertzberg, B., Milicev, Z., Burtovyy, R., Luzinov, I., and Yushin, G., A Major Constituent of Brown Algae for Use in High-Capacity Li-Ion Batteries. Science, 2011. 334(6052): p. 75-79.

17. Liu, X.H., Zhong, L., Huang, S., Mao, S.X., Zhu, T., and Huang, J.Y., Size-Dependent Fracture of Silicon Nanoparticles During Lithiation. ACS Nano, 2012. 6(2): p. 1522-1531.

18. Liu, X.H., Wang, J.W., Huang, S., Fan, F., Huang, X., Liu, Y., Krylyuk, S., Yoo, J., Dayeh, S.A., Davydov, A.V., Mao, S.X., Picraux, S.T., Zhang, S., Li, J., Zhu, T., and Huang, J.Y., In situ atomic-scale imaging of electrochemical lithiation in silicon. Nature Nanotechnology, 2012. 7(11): p. 749-756.

19. Chon, M.J., Sethuraman, V.A., McCormick, A., Srinivasan, V., and Guduru, P.R., Real-Time Measurement of Stress and Damage Evolution during Initial Lithiation of Crystalline Silicon. Physical Review Letters, 2011. 107(4): p. 045503.

20. Hertzberg, B., Benson, J., and Yushin, G., Ex-situ depth-sensing indentation measurements of electrochemically produced Si–Li alloy films. Electrochemistry Communications, 2011. 13(8): p. 818-821.

21. Liu, X.H., Zheng, H., Zhong, L., Huang, S., Karki, K., Zhang, L.Q., Liu, Y., Kushima, A., Liang, W.T., Wang, J.W., Cho, J.-H., Epstein, E., Dayeh, S.A., Picraux, S.T., Zhu, T., Li, J., Sullivan, J.P., Cumings, J., Wang, C., Mao, S.X., Ye, Z.Z., Zhang, S., and Huang, J.Y., Anisotropic Swelling and Fracture of Silicon Nanowires during Lithiation. Nano Letters, 2011. 11(8): p. 3312-3318.

22. Sethuraman, V.A., Chon, M.J., Shimshak, M., Srinivasan, V., and Guduru, P.R., In situ measurements of stress evolution in silicon thin films during electrochemical lithiation and delithiation. Journal of Power Sources, 2010. 195(15): p. 5062-5066.

23. Liu, X.H., Fan, F., Yang, H., Zhang, S., Huang, J.Y., and Zhu, T., Self-Limiting Lithiation in Silicon Nanowires. ACS Nano, 2013. 7(2): p. 1495-1503.

24. McDowell, M.T., Ryu, I., Lee, S.W., Wang, C., Nix, W.D., and Cui, Y., Studying the Kinetics of Crystalline Silicon Nanoparticle Lithiation with In Situ Transmission Electron Microscopy. Advanced Materials, 2012. 24(45): p. 6034-6041.

25. Lee, S.W., McDowell, M.T., Choi, J.W., and Cui, Y., Anomalous Shape Changes of Silicon Nanopillars by Electrochemical Lithiation. Nano Letters, 2011. 11(7): p. 3034-3039.

26. Chan, M.K.Y., Wolverton, C., and Greeley, J.P., First Principles Simulations of the Electrochemical Lithiation and Delithiation of Faceted Crystalline Silicon. Journal of the American Chemical Society, 2012. 134(35): p. 14362-14374.

27. Chevrier, V.L. and Dahn, J.R., First Principles Model of Amorphous Silicon Lithiation. Journal of The Electrochemical Society, 2009. 156(6): p. A454-A458.

28. Chew, H.B., Hou, B., Wang, X., and Xia, S., Cracking mechanisms in lithiated silicon thin film electrodes. International Journal of Solids and Structures, 2014. 51(23–24): p. 4176-4187.

29. Gao, Y.F. and Zhou, M., Coupled mechano-diffusional driving forces for fracture in electrode materials. Journal of Power Sources, 2013. 230(0): p. 176-193.

30. Huang, S. and Zhu, T., Atomistic mechanisms of lithium insertion in amorphous silicon. Journal of Power Sources, 2011. 196(7): p. 3664-3668.

31. Jung, S.C., Choi, J.W., and Han, Y.K., Anisotropic Volume Expansion of Crystalline Silicon during Electrochemical Lithium Insertion: An Atomic Level Rationale. Nano Letters, 2012. 12(10): p. 5342-5347.

32. Kim, H., Chou, C.Y., Ekerdt, J.G., and Hwang, G.S., Structure and Properties of Li-Si Alloys: A First-Principles Study. Journal of Physical Chemistry C, 2011. 115(5): p. 2514-2521.

33. Liang, W., Hong, L., Yang, H., Fan, F., Liu, Y., Li, H., Li, J., Huang, J.Y., Chen, L.-Q., Zhu, T., and Zhang, S., Nanovoid Formation and Annihilation in Gallium Nanodroplets under Lithiation–Delithiation Cycling. Nano Letters, 2013. 13(11): p. 5212-5217.

34. Liu, X.H., Huang, S., Picraux, S.T., Li, J., Zhu, T., and Huang, J.Y., Reversible Nanopore Formation in Ge Nanowires during Lithiation–Delithiation Cycling: An In Situ Transmission Electron Microscopy Study. Nano Letters, 2011. 11(9): p. 3991-3997.

35. Ryu, I., Choi, J.W., Cui, Y., and Nix, W.D., Size-dependent fracture of Si nanowire battery anodes. Journal of the Mechanics and Physics of Solids, 2011. 59(9): p. 1717-1730.

36. Shenoy, V.B., Johari, P., and Qi, Y., Elastic softening of amorphous and crystalline Li-Si Phases with increasing Li concentration: A first-principles study. Journal of Power Sources, 2010. 195(19): p. 6825-6830.

37. Yang, H., Huang, S., Huang, X., Fan, F.F., Liang, W.T., Liu, X.H., Chen, L.Q., Huang, J.Y., Li, J., Zhu, T., and Zhang, S.L., Orientation-Dependent Interfacial Mobility Governs the Anisotropic Swelling in Lithiated Silicon Nanowires. Nano Letters, 2012. 12(4): p. 1953-1958.

38. Zhang, Q.F., Zhang, W.X., Wan, W.H., Cui, Y., and Wang, E.G., Lithium Insertion In Silicon Nanowires: An ab Initio Study. Nano Letters, 2010. 10(9): p. 3243-3249.

39. Zhao, K., Pharr, M., Wan, Q., Wang, W.L., Kaxiras, E., Vlassak, J.J., and Suo, Z., Concurrent Reaction and Plasticity during Initial Lithiation of Crystalline Silicon in Lithium-Ion Batteries. Journal of The Electrochemical Society, 2012. 159(3): p. A238-A243.

40. Levitas, V.I. and Attariani, H., Anisotropic Compositional Expansion and Chemical Potential for Amorphous Lithiated Silicon under Stress Tensor. Sci. Rep., 2013. 3.

41. Lee, S.W., McDowell, M.T., Berla, L.A., Nix, W.D., and Cui, Y., Fracture of crystalline silicon nanopillars during electrochemical lithium insertion. Proceedings of the National Academy of Sciences, 2012. 109(11): p. 4080-4085.

42. Obrovac, M.N. and Christensen, L., Structural changes in silicon anodes during lithium insertion/extraction. Electrochemical and Solid State Letters, 2004. 7(5): p. A93-A96.

43. Liu, X.H., Liu, Y., Kushima, A., Zhang, S.L., Zhu, T., Li, J., and Huang, J.Y., In Situ TEM Experiments of Electrochemical Lithiation and Delithiation of Individual Nanostructures. Advanced Energy Materials, 2012. 2(7): p. 722-741.

44. McDowell, M.T., Lee, S.W., Harris, J.T., Korgel, B.A., Wang, C., Nix, W.D., and Cui, Y., In Situ TEM of Two-Phase Lithiation of Amorphous Silicon Nanospheres. Nano Letters, 2013. 13(2): p. 758-764.

45. Limthongkul, P., Jang, Y.I., Dudney, N.J., and Chiang, Y.M., Electrochemically-driven solid-state amorphization in lithium-silicon alloys and implications for lithium storage. Acta Materialia, 2003. 51(4): p. 1103-1113.

46. Kushima, A., Huang, J.Y., and Li, J., Quantitative Fracture Strength and Plasticity Measurements of Lithiated Silicon Nanowires by In Situ TEM Tensile Experiments. ACS Nano, 2012. 6(11): p. 9425-9432.

47. Zhao, K.J., Tritsaris, G.A., Pharr, M., Wang, W.L., Okeke, O., Suo, Z.G., Vlassak, J.J., and Kaxiras, E., Reactive Flow in Silicon Electrodes Assisted by the Insertion of Lithium. Nano Letters, 2012. 12(8): p. 4397-4403.

48. Cui, Z.W., Gao, F., Cui, Z.H., and Qu, J.M., A second nearest-neighbor embedded atom method interatomic potential for Li-Si alloys. Journal of Power Sources, 2012. 207: p. 150-159.

49. Chevrier, V.L. and Dahn, J.R., First Principles Studies of Disordered Lithiated Silicon. Journal of The Electrochemical Society, 2010. 157(4): p. A392-A398.

50. Johari, P., Qi, Y., and Shenoy, V.B., The Mixing Mechanism during Lithiation of Si Negative Electrode in Li-Ion Batteries: An Ab lnitio Molecular Dynamics Study. Nano Letters, 2011. 11(12): p. 5494-5500.

51. Zhao, K.J., Wang, W.L., Gregoire, J., Pharr, M., Suo, Z.G., Vlassak, J.J., and Kaxiras, E., Lithium-Assisted Plastic Deformation of Silicon Electrodes in Lithium-Ion Batteries: A First-Principles Theoretical Study. Nano Letters, 2011. 11(7): p. 2962-2967.

52. Argon, A.S. and Demkowicz, M.J., What can plasticity of amorphous silicon tell us about plasticity of metallic glasses? Metallurgical and Materials Transactions A, 2008. 39A(8): p. 1762-1778.

53. Schuh, C.A., Hufnagel, T.C., and Ramamurty, U., Overview No.144 - Mechanical behavior of amorphous alloys. Acta Materialia, 2007. 55(12): p. 4067-4109.

54. Goldman, J.L., Long, B.R., Gewirth, A.A., and Nuzzo, R.G., Strain Anisotropies and Self-Limiting Capacities in Single-Crystalline 3D Silicon Microstructures: Models for High Energy Density Lithium-Ion Battery Anodes. Advanced Functional Materials, 2011. 21(13): p. 2412-2422.

55. Sethuraman, V.A., Srinivasan, V., Bower, A.F., and Guduru, P.R., In Situ Measurements of Stress-Potential Coupling in Lithiated Silicon. Journal of The Electrochemical Society, 2010. 157(11): p. A1253-A1261.

56. Feifei, F., Shan, H., Hui, Y., Muralikrishna, R., Dibakar, D., Vivek, B.S., Adri, C.T.v.D., Sulin, Z., and Ting, Z., Mechanical properties of amorphous Li x Si alloys: a reactive force field study. Modelling and Simulation in Materials Science and Engineering, 2013. 21(7): p. 074002.

57. Cubuk, E.D., Wang, W.L., Zhao, K., Vlassak, J.J., Suo, Z., and Kaxiras, E., Morphological Evolution of Si Nanowires upon Lithiation: A First-Principles Multiscale Model. Nano Letters, 2013. 13(5): p. 2011-2015.

58. Liang, W., Yang, H., Fan, F., Liu, Y., Liu, X.H., Huang, J.Y., Zhu, T., and Zhang, S., Tough Germanium Nanoparticles under Electrochemical Cycling. ACS Nano, 2013. 7(4): p. 3427-3433.

59. Winter, M. and Besenhard, J.O., Electrochemical lithiation of tin and tin-based intermetallics and composites. Electrochimica Acta, 1999. 45(1–2): p. 31-50.

60. Sim, S., Oh, P., Park, S., and Cho, J., Critical Thickness of SiO2 Coating Layer on Core@Shell Bulk@Nanowire Si Anode Materials for Li-Ion Batteries. Advanced Materials, 2013. 25(32): p. 4498-4503.

61. Zhang, L.Q., Liu, X.H., Liu, Y., Huang, S., Zhu, T., Gui, L., Mao, S.X., Ye, Z.Z., Wang, C.M., Sullivan, J.P., and Huang, J.Y., Controlling the Lithiation-Induced Strain and Charging Rate in Nanowire Electrodes by Coating. ACS Nano, 2011. 5(6): p. 4800-4809.

62. McDowell, M.T., Lee, S.W., Ryu, I., Wu, H., Nix, W.D., Choi, J.W., and Cui, Y., Novel Size and Surface Oxide Effects in Silicon Nanowires as Lithium Battery Anodes. Nano Letters, 2011. 11(9): p. 4018-4025.

63. Liu, J., Li, N., Goodman, M.D., Zhang, H.G., Epstein, E.S., Huang, B., Pan, Z., Kim, J., Choi, J.H., Huang, X., Liu, J., Hsia, K.J., Dillon, S.J., and Braun, P.V.,

Mechanically and Chemically Robust Sandwich-Structured C@Si@C Nanotube Array Li-Ion Battery Anodes. ACS Nano, 2015. 9(2): p. 1985-1994.

64. Wang, J.W., Liu, X.H., Zhao, K., Palmer, A., Patten, E., Burton, D., Mao, S.X., Suo, Z., and Huang, J.Y., Sandwich-Lithiation and Longitudinal Crack in Amorphous Silicon Coated on Carbon Nanofibers. ACS Nano, 2012. 6(10): p. 9158-9167.

65. Zhao, J., Lu, Z., Liu, N., Lee, H.-W., McDowell, M.T., and Cui, Y., Dry-air-stable lithium silicide–lithium oxide core–shell nanoparticles as high-capacity prelithiation reagents. Nat Commun, 2014. 5.

66. Liu, N., Wu, H., McDowell, M.T., Yao, Y., Wang, C., and Cui, Y., A Yolk-Shell Design for Stabilized and Scalable Li-Ion Battery Alloy Anodes. Nano Letters, 2012. 12(6): p. 3315-3321.

67. Yao, Y., Liu, N., McDowell, M.T., Pasta, M., and Cui, Y., Improving the cycling stability of silicon nanowire anodes with conducting polymer coatings. Energy & Environmental Science, 2012. 5(7): p. 7927-7930.

68. Zhang, Y., Li, Y., Wang, Z., and Zhao, K., Lithiation of SiO2 in Li-Ion Batteries: In Situ Transmission Electron Microscopy Experiments and Theoretical Studies. Nano Letters, 2014. 14(12): p. 7161-7170.

69. Slater, M.D., Kim, D., Lee, E., and Johnson, C.S., Sodium-Ion Batteries. Advanced Functional Materials, 2013. 23(8): p. 947-958.

70. Tang, K., Fu, L., White, R.J., Yu, L., Titirici, M.-M., Antonietti, M., and Maier, J., Hollow Carbon Nanospheres with Superior Rate Capability for Sodium-Based Batteries. Advanced Energy Materials, 2012. 2(7): p. 873-877.

71. Wessells, C.D., Peddada, S.V., Huggins, R.A., and Cui, Y., Nickel Hexacyanoferrate Nanoparticle Electrodes For Aqueous Sodium and Potassium Ion Batteries. Nano Letters, 2011. 11(12): p. 5421-5425.

72. Hong, S.Y., Kim, Y., Park, Y., Choi, A., Choi, N.-S., and Lee, K.T., Charge carriers in rechargeable batteries: Na ions vs. Li ions. Energy & Environmental Science, 2013. 6(7): p. 2067-2081.

73. Palomares, V., Casas-Cabanas, M., Castillo-Martinez, E., Han, M.H., and Rojo, T., Update on Na-based battery materials. A growing research path. Energy & Environmental Science, 2013. 6(8): p. 2312-2337.

74. Alcántara, R., Lavela, P., Ortiz, G.F., and Tirado, J.L., Carbon Microspheres Obtained from Resorcinol-Formaldehyde as High-Capacity Electrodes for Sodium-Ion Batteries. Electrochemical and Solid-State Letters, 2005. 8(4): p. A222-A225.

75. Cao, Y., Xiao, L., Sushko, M.L., Wang, W., Schwenzer, B., Xiao, J., Nie, Z., Saraf, L.V., Yang, Z., and Liu, J., Sodium Ion Insertion in Hollow Carbon Nanowires for Battery Applications. Nano Letters, 2012. 12(7): p. 3783-3787.

76. Scrosati, B., Recent advances in lithium ion battery materials. Electrochimica Acta, 2000. 45(15–16): p. 2461-2466.

77. Stevens, D.A. and Dahn, J.R., High Capacity Anode Materials for Rechargeable Sodium - Ion Batteries. Journal of The Electrochemical Society, 2000. 147(4): p. 1271-1273.

78. Shao, Y., Xiao, J., Wang, W., Engelhard, M., Chen, X., Nie, Z., Gu, M., Saraf, L.V., Exarhos, G., Zhang, J.-G., and Liu, J., Surface-Driven Sodium Ion Energy Storage in Nanocellular Carbon Foams. Nano Letters, 2013. 13: p. 3909-3914.

79. Komaba, S., Murata, W., Ishikawa, T., Yabuuchi, N., Ozeki, T., Nakayama, T., Ogata, A., Gotoh, K., and Fujiwara, K., Electrochemical Na Insertion and Solid Electrolyte Interphase for Hard-Carbon Electrodes and Application to Na-Ion Batteries. Advanced Functional Materials, 2011. 21(20): p. 3859-3867.

80. Qian, J., Chen, Y., Wu, L., Cao, Y., Ai, X., and Yang, H., High capacity Na-storage and superior cyclability of nanocomposite Sb/C anode for Na-ion batteries. Chemical Communications, 2012. 48(56): p. 7070-7072.

81. Xiao, L., Cao, Y., Xiao, J., Wang, W., Kovarik, L., Nie, Z., and Liu, J., High capacity, reversible alloying reactions in SnSb/C nanocomposites for Na-ion battery applications. Chemical Communications, 2012. 48(27): p. 3321-3323.

82. Zhu, Y., Han, X., Xu, Y., Liu, Y., Zheng, S., Xu, K., Hu, L., and Wang, C., Electrospun Sb/C Fibers for A Stable and Fast Sodium-Ion Battery Anode. ACS Nano, 2013. 7: p. 6378–6386.

83. Wang, J.W., He, Y., Fan, F., Liu, X.H., Xia, S., Liu, Y., Harris, C.T., Li, H., Huang, J.Y., Mao, S.X., and Zhu, T., Two-Phase Electrochemical Lithiation in Amorphous Silicon. Nano Letters, 2013. 13(2): p. 709-715.

84. McDowell, M.T., Lee, S.W., Nix, W.D., and Cui, Y., 25th Anniversary Article: Understanding the Lithiation of Silicon and Other Alloying Anodes for Lithium-Ion Batteries. Advanced Materials, 2013. 25(36): p. 4966-4985.

85. Yoo, H., Lee, J.-I., Kim, H., Lee, J.-P., Cho, J., and Park, S., Helical Silicon/Silicon Oxide Core–Shell Anodes Grown onto the Surface of Bulk Silicon. Nano Letters, 2011. 11(10): p. 4324-4328.

86. Yu, B.-C., Hwa, Y., Park, C.-M., Kim, J.-H., and Sohn, H.-J., Effect of oxide layer thickness to nano-Si anode for Li-ion batteries. RSC Advances, 2013. 3(24): p. 9408-9413.

87. Ye, J.C., An, Y.H., Heo, T.W., Biener, M.M., Nikolic, R.J., Tang, M., Jiang, H., and Wang, Y.M., Enhanced lithiation and fracture behavior of silicon mesoscale pillars via atomic layer coatings and geometry design. Journal of Power Sources, 2014. 248(0): p. 447-456.

88. Memarzadeh Lotfabad, E., Kalisvaart, P., Cui, K., Kohandehghan, A., Kupsta, M., Olsen, B., and Mitlin, D., ALD TiO2 coated silicon nanowires for lithium ion battery anodes with enhanced cycling stability and coulombic efficiency. Physical Chemistry Chemical Physics, 2013. 15(32): p. 13646-13657.

89. Jung, Y.S., Lee, K.T., and Oh, S.M., Si–carbon core–shell composite anode in lithium secondary batteries. Electrochimica Acta, 2007. 52(24): p. 7061-7067.

90. Gu, M., Li, Y., Li, X., Hu, S., Zhang, X., Xu, W., Thevuthasan, S., Baer, D.R., Zhang, J.-G., Liu, J., and Wang, C., In Situ TEM Study of Lithiation Behavior of Silicon Nanoparticles Attached to and Embedded in a Carbon Matrix. ACS Nano, 2012. 6(9): p. 8439-8447.

91. Chang, W.-S., Park, C.-M., Kim, J.-H., Kim, Y.-U., Jeong, G., and Sohn, H.-J., Quartz (SiO2): a new energy storage anode material for Li-ion batteries. Energy & Environmental Science, 2012. 5(5): p. 6895-6899.

92. Favors, Z., Wang, W., Bay, H.H., George, A., Ozkan, M., and Ozkan, C.S., Stable Cycling of SiO2 Nanotubes as High-Performance Anodes for Lithium-Ion Batteries. Sci. Rep., 2014. 4.

93. Song, K., Yoo, S., Kang, K., Heo, H., Kang, Y.-M., and Jo, M.-H., Hierarchical SiOx nanoconifers for Li-ion battery anodes with structural stability and kinetic enhancement. Journal of Power Sources, 2013. 229(0): p. 229-233.

94. Yan, N., Wang, F., Zhong, H., Li, Y., Wang, Y., Hu, L., and Chen, Q., Hollow Porous SiO2 Nanocubes Towards High-performance Anodes for Lithium-ion Batteries. Sci. Rep., 2013. 3.

95. Sasidharan, M., Liu, D., Gunawardhana, N., Yoshio, M., and Nakashima, K., Synthesis, characterization and application for lithium-ion rechargeable batteries of hollow silica nanospheres. Journal of Materials Chemistry, 2011. 21(36): p. 13881-13888.

96. van Duin, A.C.T., Dasgupta, S., Lorant, F., and Goddard, W.A., ReaxFF: A reactive force field for hydrocarbons. Journal of Physical Chemistry A, 2001. 105(41): p. 9396-9409.

97. van Duin, A.C.T., Strachan, A., Stewman, S., Zhang, Q.S., Xu, X., and Goddard, W.A., ReaxFF(SiO) reactive force field for silicon and silicon oxide systems. Journal of Physical Chemistry A, 2003. 107(19): p. 3803-3811.

98. Plimpton, S., Fast Parallel Algorithms for Short-Range Molecular Dynamics. Journal of Computational Physics, 1995. 117(1): p. 1-19.

99. Key, B., Morcrette, M., Tarascon, J.M., and Grey, C.P., Pair Distribution Function Analysis and Solid State NMR Studies of Silicon Electrodes for Lithium Ion Batteries: Understanding the (De)lithiation Mechanisms. Journal of the American Chemical Society, 2011. 133(3): p. 503-512.

100. Demkowicz, M.J. and Argon, A.S., Liquidlike atomic environments act as plasticity carriers in amorphous silicon. Physical Review B, 2005. 72(24).

101. Demkowicz, M.J. and Argon, A.S., High-density liquidlike component facilitates plastic flow in a model amorphous silicon system. Physical Review Letters, 2004. 93(2): p. 025505.

102. Soni, S.K., Sheldon, B.W., Xiao, X.C., and Tokranov, A., Thickness effects on the lithiation of amorphous silicon thin films. Scripta Materialia, 2011. 64(4): p. 307-310.

103. Uchic, M.D., Dimiduk, D.M., Florando, J.N., and Nix, W.D., Sample dimensions influence strength and crystal plasticity. Science, 2004. 305(5686): p. 986-989.

104. Zhu, T., Li, J., Ogata, S., and Yip, S., Mechanics of ultra-strength materials. MRS Bulletin, 2009. 34(3): p. 167-172.

105. Zhu, T. and Li, J., Ultra-strength Materials. Progress in Materials Science, 2010. 55: p. 710-757.

106. Greer, J.R. and De Hosson, J.T.M., Plasticity in small-sized metallic systems: Intrinsic versus extrinsic size effect. Progress in Materials Science, 2011. 56(6): p. 654-724.

107. Volkert, C.A., Donohue, A., and Spaepen, F., Effect of sample size on deformation in amorphous metals. Journal of Applied Physics, 2008. 103(8): p. 083539.

108. Lund, A.C. and Schuh, C.A., Yield surface of a simulated metallic glass. Acta Materialia, 2003. 51(18): p. 5399-5411.

109. Haftbaradaran, H., Xiao, X., Verbrugge, M.W., and Gao, H., Method to deduce the critical size for interfacial delamination of patterned electrode structures and application to lithiation of thin-film silicon islands. Journal of Power Sources, 2012. 206(0): p. 357-366.

110. Aifantis, K.E., Hackney, S.A., and Dempsey, J.P., Design criteria for nanostructured Li-ion batteries. Journal of Power Sources, 2007. 165(2): p. 874-879.

111. Ryu, I., Lee, S.W., Gao, H., Cui, Y., and Nix, W.D., Microscopic model for fracture of crystalline Si nanopillars during lithiation. Journal of Power Sources, 2014. 255(0): p. 274-282.

112. Pharr, M., Suo, Z., and Vlassak, J.J., Measurements of the Fracture Energy of Lithiated Silicon Electrodes of Li-Ion Batteries. Nano Letters, 2013. 13(11): p. 5570-5577.

113. Murali, P., Guo, T.F., Zhang, Y.W., Narasimhan, R., Li, Y., and Gao, H.J., Atomic Scale Fluctuations Govern Brittle Fracture and Cavitation Behavior in Metallic Glasses. Physical Review Letters, 2011. 107(21): p. 215501.

114. Gu, X.W., Jafary-Zadeh, M., Chen, D.Z., Wu, Z., Zhang, Y.-W., Srolovitz, D.J., and Greer, J.R., Mechanisms of Failure in Nanoscale Metallic Glass. Nano Letters, 2014. 14(10): p. 5858-5864.

115. Huang, S., Fan, F., Li, J., Zhang, S., and Zhu, T., Stress generation during lithiation of high-capacity electrode particles in lithium ion batteries. Acta Materialia, 2013. 61(12): p. 4354-4364.

116. Di Leo, C.V., Rejovitzky, E., and Anand, L., A Cahn–Hilliard-type phase-field theory for species diffusion coupled with large elastic deformations: Application to phase-separating Li-ion electrode materials. Journal of the Mechanics and Physics of Solids, 2014. 70(0): p. 1-29.

117. Chen, L., Fan, F., Hong, L., Chen, J., Ji, Y.Z., Zhang, S.L., Zhu, T., and Chen, L.Q., A Phase-Field Model Coupled with Large Elasto-Plastic Deformation: Application to Lithiated Silicon Electrodes. Journal of The Electrochemical Society, 2014. 161(11): p. F3164-F3172.

118. Hsueh, C.H. and Evans, A.G., Oxidation induced stresses and some effects on the behavior of oxide films. Journal of Applied Physics, 1983. 54(11): p. 6672-6686.

119. Dalla Torre, J., Bocquet, J.-L., Limoge, Y., Crocombette, J.-P., Adam, E., Martin, G., Baron, T., Rivallin, P., and Mur, P., Study of self-limiting oxidation of silicon nanoclusters by atomistic simulations. Journal of Applied Physics, 2002. 92(2): p. 1084-1094.

120. Zhao, K., Pharr, M., Cai, S., Vlassak, J.J., and Suo, Z., Large Plastic Deformation in High-Capacity Lithium-Ion Batteries Caused by Charge and Discharge. Journal of the American Ceramic Society, 2011. 94: p. s226-s235.

121. Cui, Z., Gao, F., and Qu, J., Interface-reaction controlled diffusion in binary solids with applications to lithiation of silicon in lithium-ion batteries. Journal of the Mechanics and Physics of Solids, 2013. 61(2): p. 293-310.

122. Pharr, M., Zhao, K., Wang, X., Suo, Z., and Vlassak, J.J., Kinetics of Initial Lithiation of Crystalline Silicon Electrodes of Lithium-Ion Batteries. Nano Letters, 2012. 12(9): p. 5039-5047.

123. Ruffo, R., Hong, S.S., Chan, C.K., Huggins, R.A., and Cui, Y., Impedance Analysis of Silicon Nanowire Lithium Ion Battery Anodes. The Journal of Physical Chemistry C, 2009. 113(26): p. 11390-11398.

124. Deshpande, R., Cheng, Y.-T., Verbrugge, M.W., and Timmons, A., Diffusion Induced Stresses and Strain Energy in a Phase-Transforming Spherical Electrode Particle. Journal of The Electrochemical Society, 2011. 158(6): p. A718-A724.

125. Haftbaradaran, H., Song, J., Curtin, W.A., and Gao, H., Continuum and atomistic models of strongly coupled diffusion, stress, and solute concentration. Journal of Power Sources, 2011. 196(1): p. 361-370.

126. Yang, H., Liang, W., Guo, X., Wang, C.-M., and Zhang, S., Strong kinetics-stress coupling in lithiation of Si and Ge anodes. Extreme Mechanics Letters, 2015. 2(0): p. 1-6.

127. Gösele, U. and Tu, K.N., ‘‘Critical thickness’’ of amorphous phase formation in binary diffusion couples. Journal of Applied Physics, 1989. 66(6): p. 2619-2626.

128. Gösele, U. and Tu, K.N., Growth kinetics of planar binary diffusion couples: ’’Thin‐film case’’ versus ’’bulk cases’’. Journal of Applied Physics, 1982. 53(4): p. 3252-3260.

129. Tu, K.N., Selective growth of metal‐rich silicide of near‐noble metals. Applied Physics Letters, 1975. 27(4): p. 221-224.

130. Huang, J.Y., Zhong, L., Wang, C.M., Sullivan, J.P., Xu, W., Zhang, L.Q., Mao, S.X., Hudak, N.S., Liu, X.H., Subramanian, A., Fan, H.Y., Qi, L.A., Kushima, A., and Li, J., In Situ Observation of the Electrochemical Lithiation of a Single SnO2 Nanowire Electrode. Science, 2010. 330(6010): p. 1515-1520.

131. Chandrasekaran, R., Magasinski, A., Yushin, G., and Fuller, T.F., Analysis of Lithium Insertion/Deinsertion in a Silicon Electrode Particle at Room Temperature. Journal of The Electrochemical Society, 2010. 157(10): p. A1139-A1151.

132. Zhang, X.C., Shyy, W., and Sastry, A.M., Numerical simulation of intercalation-induced stress in Li-ion battery electrode particles. Journal of The Electrochemical Society, 2007. 154(10): p. A910-A916.

133. Huggins, R.A. and Nix, W.D., Decrepitation model for capacity loss during cycling of alloys in rechargeable electrochemical systems. Ionics, 2000. 6: p. 57-63.

134. Christensen, J. and Newman, J., Stress generation and fracture in lithium insertion materials. Journal of Solid State Electrochemistry, 2006. 10(5): p. 293-319.

135. Cheng, Y.T. and Verbrugge, M.W., Evolution of stress within a spherical insertion electrode particle under potentiostatic and galvanostatic operation. Journal of Power Sources, 2009. 190(2): p. 453-460.

136. Bhandakkar, T.K. and Gao, H.J., Cohesive modeling of crack nucleation in a cylindrical electrode under axisymmetric diffusion induced stresses. International Journal of Solids and Structures, 2011. 48(16-17): p. 2304-2309.

137. Bower, A.F., Guduru, P.R., and Sethuraman, V.A., A finite strain model of stress, diffusion, plastic flow, and electrochemical reactions in a lithium-ion half-cell. Journal of the Mechanics and Physics of Solids, 2011. 59(4): p. 804-828.

138. Zhao, K.J., Pharr, M., Vlassak, J.J., and Suo, Z.G., Inelastic hosts as electrodes for high-capacity lithium-ion batteries. Journal of Applied Physics, 2011. 109: p. 016110

139. Tang, M., Huang, H.Y., Meethong, N., Kao, Y.H., Carter, W.C., and Chiang, Y.M., Model for the Particle Size, Overpotential, and Strain Dependence of Phase Transition Pathways in Storage Electrodes: Application to Nanoscale Olivines. Chemistry of Materials, 2009. 21(8): p. 1557-1571.

140. Burch, D. and Bazant, M.Z., Size-Dependent Spinodal and Miscibility Gaps for Intercalation in Nanoparticles. Nano Letters, 2009. 9(11): p. 3795-3800.

141. Golmon, S., Maute, K., Lee, S.H., and Dunn, M.L., Stress generation in silicon particles during lithium insertion. Applied Physics Letters, 2010. 97(3): p. 033111.

142. Kasavajjula, U., Wang, C., and Appleby, A.J., Nano- and bulk-silicon-based insertion anodes for lithium-ion secondary cells. Journal of Power Sources, 2007. 163(2): p. 1003-1039.

143. Gao, H.J., Ji, B.H., Jager, I.L., Arzt, E., and Fratzl, P., Materials become insensitive to flaws at nanoscale: Lessons from nature. Proceedings Of The National Academy Of Sciences Of The United States Of America, 2003. 100(10): p. 5597-5600.

144. Mott, N.F., Rigo, S., Rochet, F., and Stoneham, A.M., Oxidation of silicon Philosophical Magazine B, 1989. 60(2): p. 189-212.

145. Yang, H., Fan, F., Liang, W., Guo, X., Zhu, T., and Zhang, S., A chemo-mechanical model of lithiation in silicon. Journal of the Mechanics and Physics of Solids, 2014. 70(0): p. 349-361.

146. Hatchard, T.D. and Dahn, J.R., In Situ XRD and Electrochemical Study of the Reaction of Lithium with Amorphous Silicon. Journal of The Electrochemical Society, 2004. 151(6): p. A838-A842.

147. He, Y., Yu, X., Li, G., Wang, R., Li, H., Wang, Y., Gao, H., and Huang, X., Shape evolution of patterned amorphous and polycrystalline silicon microarray thin film electrodes caused by lithium insertion and extraction. Journal of Power Sources, 2012. 216(0): p. 131-138.

148. Soni, S.K., Sheldon, B.W., Xiao, X., Verbrugge, M.W., Dongjoon, A., H., H., and Huajian, G., Stress Mitigation during the Lithiation of Patterned Amorphous Si Islands. Journal of The Electrochemical Society, 2011. 159(1): p. A38-A43.

149. Liao, H., Karki, K., Zhang, Y., Cumings, J., and Wang, Y., Interfacial Mechanics of Carbon Nanotube@Amorphous-Si Coaxial Nanostructures. Advanced Materials, 2011. 23(37): p. 4318-4322.

150. Ghassemi, H., Au, M., Chen, N., Heiden, P.A., and Yassar, R.S., In Situ Electrochemical Lithiation/Delithiation Observation of Individual Amorphous Si Nanorods. ACS Nano, 2011. 5(10): p. 7805-7811.

151. Wang, C.-M., Li, X., Wang, Z., Xu, W., Liu, J., Gao, F., Kovarik, L., Zhang, J.-G., Howe, J., Burton, D.J., Liu, Z., Xiao, X., Thevuthasan, S., and Baer, D.R., In Situ TEM Investigation of Congruent Phase Transition and Structural Evolution of Nanostructured Silicon/Carbon Anode for Lithium Ion Batteries. Nano Letters, 2012. 12(3): p. 1624-1632.

152. Johnson, W.L., Thermodynamic and kinetic aspects of the crystal to glass transformation in metallic materials. Progress in Materials Science, 1986. 30(2): p. 81-134.

153. Sheng, H.W., Liu, H.Z., Cheng, Y.Q., Wen, J., Lee, P.L., Luo, W.K., Shastri, S.D., and Ma, E., Polyamorphism in a metallic glass. Nat Mater, 2007. 6(3): p. 192-197.

154. McMillan, P.F., Polyamorphic transformations in liquids and glasses. Journal of Materials Chemistry, 2004. 14(10): p. 1506-1512.

155. Key, B., Bhattacharyya, R., Morcrette, M., Seznéc, V., Tarascon, J.-M., and Grey, C.P., Real-Time NMR Investigations of Structural Changes in Silicon Electrodes for Lithium-Ion Batteries. Journal of the American Chemical Society, 2009. 131(26): p. 9239-9249.

156. Scrosati, B. and Garche, J., Lithium batteries: Status, prospects and future. Journal of Power Sources, 2010. 195(9): p. 2419-2430.

157. Dunn, B., Kamath, H., and Tarascon, J.-M., Electrical Energy Storage for the Grid: A Battery of Choices. Science, 2011. 334(6058): p. 928-935.

158. Liu, Y., Fan, F., Wang, J., Liu, Y., Chen, H., Jungjohann, K.L., Xu, Y., Zhu, Y., Bigio, D., Zhu, T., and Wang, C., In Situ Transmission Electron Microscopy Study of Electrochemical Sodiation and Potassiation of Carbon Nanofibers. Nano Letters, 2014. 14(6): p. 3445-3452.

159. Thomas, P. and Billaud, D., Sodium electrochemical insertion mechanisms in various carbon fibres. Electrochimica Acta, 2001. 46(22): p. 3359-3366.

160. Zhao, K., Pharr, M., Hartle, L., Vlassak, J.J., and Suo, Z., Fracture and debonding in lithium-ion batteries with electrodes of hollow core–shell nanostructures. Journal of Power Sources, 2012. 218(0): p. 6-14.